



University of Pennsylvania  
**ScholarlyCommons**

---

Publicly Accessible Penn Dissertations


---

2019

## The Development Of Mems-Based Implantable Oxygen Sensing Systems

Didi She  
*University of Pennsylvania*

Follow this and additional works at: <https://repository.upenn.edu/edissertations>

 Part of the [Electrical and Electronics Commons](#)

---

### Recommended Citation

She, Didi, "The Development Of Mems-Based Implantable Oxygen Sensing Systems" (2019). *Publicly Accessible Penn Dissertations*. 3642.  
<https://repository.upenn.edu/edissertations/3642>

This paper is posted at ScholarlyCommons. <https://repository.upenn.edu/edissertations/3642>  
For more information, please contact [repository@pobox.upenn.edu](mailto:repository@pobox.upenn.edu).

---

# The Development Of Mems-Based Implantable Oxygen Sensing Systems

## Abstract

Oxygen-based cues are direct assessments for a wide range of in vivo biological effects, ranging from mitochondrial disease to tissue engineering/regenerative medicine. Existing electrochemical oxygen sensors are permanent systems applicable to short-term intraoperative use; devices are extracted before wound closure. Development of biocompatible oxygen sensors for long-term, post-surgery monitoring are therefore, desirable for clinical trials where objective oxygen measures are lacking. A biodegradable oxygen sensor that can break down into non-toxic components after a targeted lifespan, reducing the risk of chronic inflammatory response frequently observed with permanent devices, is another promising approach to advance the postoperative monitoring of oxygen tension and provide an additional means to monitor a number of diseases and injuries that are transient in nature, such as bone fracture, traumatic brain injury and wound healing. In this dissertation, we improved the current oxygen sensing technology to the point that it could be used for long-term applications, and further developed a biodegradable oxygen sensor along with a transient energy source to support the design of completely biodegradable oxygen sensing systems. Specifically, a biocompatible oxygen sensor, integrated with a customized circuit and an off-the-shelf battery were designed, built and tested. Oxygen levels in mouse gluteus muscle and zebrafish trunk muscle were both investigated to examine the sensor's ability to monitor dynamic oxygen tension in vivo. In addition, a biodegradable battery featuring long shelf life and stable performance in the presence of changing body conditions was designed, fabricated and examined in vitro. Finally, a completely biodegradable oxygen sensor featuring a Mg-Mo galvanic pair was demonstrated. This approach measures physiological oxygen tension in a transient, harmless manner in the body, while simultaneously acting as a potential energy source for additional devices. Additionally, such sensors may have application in transient monitoring of the environment, such as environmental spills and algal tides.

## Degree Type

Dissertation

## Degree Name

Doctor of Philosophy (PhD)

## Graduate Group

Electrical & Systems Engineering

## First Advisor

Mark G. Allen

## Keywords

Battery, Biocompatible, Biodegradable, MEMS, Microfabrication, Oxygen sensor

## Subject Categories

Electrical and Electronics

THE DEVELOPMENT OF MEMS-BASED IMPLANTABLE OXYGEN SENSING SYSTEMS

Didi She

A DISSERTATION

in

Electrical and Systems Engineering

Presented to the Faculties of the University of Pennsylvania

in

Partial Fulfillment of the Requirements for the

Degree of Doctor of Philosophy

2019

Supervisor of Dissertation

---

Dr. Mark G. Allen

Alfred Fitler Moore Professor

Department of Electrical and System Engineering

Graduate Group Chairperson

---

Dr. Victor Preciado

Associate Professor

Department of Electrical and System Engineering

Dissertation Committee

Dr. Cherie Kagan

Stephen J. Angello Professor

Department of Electrical and System Engineering

Dr. Charlie Johnson

Professor

Department of Electrical and System Engineering

Dr. David Issadore

Associate Professor

Department of Electrical and System Engineering

THE DEVELOPMENT OF MEMS-BASED IMPLANTABLE OXYGEN SENSING SYSTEMS

COPYRIGHT

2019

Didi She



## ACKNOWLEDGMENT

Looking back on my PhD career, I would like to express my great gratitude to many people who have helped and influenced me and my research.

First of all, I sincerely thank my advisor Dr. Mark Allen. Thank him for allowing me to join the lab and guiding me throughout my doctoral study. Thank him for all the patient guidance and kind helps he has been giving me from the first day we met. It would not be possible for me to complete this dissertation without his support and advise.

I would also like to thank Dr. Cherie Kagan, Dr. Charlie Johnson, and Dr. David Issadore for their gracious supports and dedicating their time and efforts on evaluating and guiding my work.

I would also like to acknowledge the efforts of our collaborators at Children's Hospital of Philadelphia: Dr. Zarazuela Zolkipli-Cunningham, Dr. Christoph Seiler, Dr. Marni Falk, Dr. Douglas C. Wallace, Ms. Katherine Mitchell and Mr. Xiaokang Bai. They provided zebrafish and mouse for the *in vivo* studies and spent many hours in joint testing of the animal models.

Also, I would also like to thank the trainers and staff members in Singh Center for Nanotechnology (SCN) at Penn. Without the variety of instruments well-maintained by them, I won't be able to finish any part of my projects.

I am grateful to all the friendships and supports from previous and current members of the MicroSensors and MicroActuators (MSMA) group. I really enjoy working with and

learning from them. Five and a half years we have had together working in lab is my unforgettable memory at Penn and will forever be an important experience in shaping who I am.

Last but not least, I would like to express appreciation to my parents and grandparents for their help and love and especially to my husband: thank you very much for your unconditional love and support.

# **ABSTRACT**

## **THE DEVELOPMENT OF MEMS-BASED BIOCOMPATIBLE AND BIODEGRADABLE OXYGEN SENSING SYSTEMS**

Didi She

Prof. Mark G. Allen

Oxygen-based cues are direct assessments for a wide range of *in vivo* biological effects, ranging from mitochondrial disease to tissue engineering/regenerative medicine. Existing electrochemical oxygen sensors are permanent systems applicable to short-term intraoperative use; devices are extracted before wound closure. Development of biocompatible oxygen sensors for long-term, post-surgery monitoring are therefore, desirable for clinical trials where objective oxygen measures are lacking. A biodegradable oxygen sensor that can break down into non-toxic components after a targeted lifespan, reducing the risk of chronic inflammatory response frequently observed with permanent devices, is another promising approach to advance the postoperative monitoring of oxygen tension and provide an additional means to monitor a number of diseases and injuries that are transient in nature, such as bone fracture, traumatic brain injury and wound healing. In this dissertation, we improved the current oxygen sensing technology to the point that it could be used for long-term applications, and further developed a biodegradable oxygen sensor along with a transient energy source to support the design of completely biodegradable oxygen sensing systems. Specifically, a biocompatible oxygen sensor, integrated with a customized circuit and an off-the-shelf

battery were designed, built and tested. Oxygen levels in mouse gluteus muscle and zebrafish trunk muscle were both investigated to examine the sensor's ability to monitor dynamic oxygen tension *in vivo*. In addition, a biodegradable battery featuring long shelf life and stable performance in the presence of changing body conditions was designed, fabricated and examined *in vitro*. Finally, a completely biodegradable oxygen sensor featuring a Mg-Mo galvanic pair was demonstrated. This approach measures physiological oxygen tension in a transient, harmless manner in the body, while simultaneously acting as a potential energy source for additional devices. Additionally, such sensors may have application in transient monitoring of the environment, such as environmental spills and algal tides.

## TABLE OF CONTENTS

<b>ACKNOWLEDGMENT .....</b>	<b>III</b>
<b>ABSTRACT.....</b>	<b>V</b>
<b>LIST OF TABLES.....</b>	<b>X</b>
<b>LIST OF ILLUSTRATIONS.....</b>	<b>XI</b>
<b>CHAPTER 1 INTRODUCTION.....</b>	<b>1</b>
<b>1.1 Oxygen sensors for biomedical applications.....</b>	<b>1</b>
1.1.1 Medical need for oxygen sensing in the body .....	1
1.1.2 Electrochemical oxygen sensors .....	3
<b>1.2 Implantable MEMS technologies.....</b>	<b>4</b>
1.2.1 Flexible devices for implantable applications.....	5
1.2.2 Toward biodegradable systems.....	6
<b>1.3 Research objective and thesis outline .....</b>	<b>10</b>
<b>CHAPTER 2 MICROFABRICATED OXYGEN SENSOR FOR BIOMEDICAL APPLICATIONS.....</b>	<b>14</b>
<b>2.1 Background and motivation .....</b>	<b>14</b>
<b>2.2 Working principle.....</b>	<b>18</b>
<b>2.3 Biocompatible Material Selection.....</b>	<b>19</b>
2.3.1 Electrode material .....	19
2.3.2 Oxygen permeable membrane material.....	21
<b>2.4 Design and fabrication.....</b>	<b>22</b>
2.4.1 Design and fabrication of sensor electrodes .....	22
2.4.2 Design of electrolyte reservoir.....	28
2.4.3 Design and fabrication of PDMS-based oxygen sensor .....	29
2.4.4 Design and fabrication of FEP-based oxygen sensor .....	31
<b>2.4 Customized potentiostat.....</b>	<b>34</b>
<b>2.5 Wireless transmission .....</b>	<b>37</b>
<b>2.6 Benchtop test results.....</b>	<b>40</b>
2.6.1 Response tests.....	40

2.6.2 Stability Tests .....	45
2.6.3 Lifetime Tests .....	48
2.6.4 Customized potentiostat platform .....	50
2.6.5 End-to-end Testing of oxygen sensing system .....	54
<b>2.7 Summary.....</b>	<b>55</b>
 <b>CHAPTER 3 <i>IN VIVO</i> APPLICATION OF THE OXYGEN SENSOR.....</b>	<b>56</b>
<b>3.1 Background and motivation .....</b>	<b>56</b>
<b>3.2 Sensor design and test method.....</b>	<b>59</b>
3.2.1 Small sensor design .....	59
3.2.2 Sensor test method.....	61
3.2.3 Animal test methods .....	64
<b>3.3 Results and discussion.....</b>	<b>65</b>
3.3.1 Sensor characterization .....	65
3.3.2 <i>In vivo</i> test results .....	70
3.3.3 Critical problems causing device drift/failure.....	73
<b>3.5 Summary.....</b>	<b>74</b>
 <b>CHAPTER 4 BIODEGRADABLE BATTERY WITH IMMOBLIZED ELECTROLYTE .</b>	<b>76</b>
<b>4.1 Background and motivation .....</b>	<b>76</b>
<b>4.2 Materials and Design .....</b>	<b>79</b>
4.2.1 Battery Design and Working Principle .....	79
<b>4.3 Fabrication and assembly .....</b>	<b>84</b>
<b>4.4 Characterization and testing .....</b>	<b>85</b>
<b>4.5 Results and Discussion.....</b>	<b>87</b>
4.5.1 Characterization of battery components.....	87
4.5.2 Electrochemical testing of biodegradable batteries.....	91
<b>4.6 Summary.....</b>	<b>95</b>
 <b>CHAPTER 5 BIODEGRADABLE OXYGEN SENSORS BASED ON GALVANIC CORROSION .....</b>	<b>96</b>
<b>5.1 Background and motivation .....</b>	<b>96</b>
<b>5.2 Materials and Design .....</b>	<b>96</b>
5.2.1 Materials .....	96
5.2.2 Sensor Design and Working Principle .....	97
5.2.3 Measurement test circuit of the sensor .....	101

<b>5.3 Characterization and testing .....</b>	<b>103</b>
5.3.1 Electrochemical analysis of the sensor.....	103
5.3.4 Characterization of a Mg-Mo oxygen Sensor.....	110
<b>5.4 Device modeling .....</b>	<b>112</b>
<b>5.5 Summary.....</b>	<b>116</b>
 <b>CHAPTER 6 CONCLUSIONS AND FUTURE WORK.....</b>	 <b>118</b>
<b>6.1 Summary of Conducted Research .....</b>	<b>118</b>
<b>6.2 Suggestions for Future Research .....</b>	<b>119</b>
6.2.1 Clark-type Oxygen Sensor and <i>In Vivo</i> Study .....	119
6.2.2 Lifetime of the biodegradable devices .....	121
6.2.3 Biodegradable Oxygen Sensor .....	123
 <b>APPENDIX 1 .....</b>	 <b>125</b>
 <b>APPENDIX 2 .....</b>	 <b>145</b>
 <b>BIBLIOGRAPHY.....</b>	 <b>151</b>

## LIST OF TABLES

Table 1. Thermal stability and solvent compatibility of discussed biodegradable polymer. .....	7
Table 2. Biodegradable metals and their corrosion-related characteristics .....	8



## LIST OF ILLUSTRATIONS

Figure 1. Dissertation outline.....	11
Figure 2. Operation of an electrochemical oxygen sensor. A potentiostat is used as the external circuit to apply a voltage and measure current. When a negative potential is applied from the circuit across the working and reference electrodes, oxygen in contact with the working electrode is reduced, thus generating an electric current. ....	19
Figure 3. Designs with different (a) surface area ratio of the working, reference, and counter electrodes, (b) electrode materials (graphite, Pt and Au) and (c) shapes.....	25
Figure 4. Fabrication scheme of sensor electrode on polyimide substrate.....	27
Figure 5. (a) Optical images of sensor electrodes after step (ii) as seen from the backside. The Cr region can be seen through the translucent polyimide; (b) Sensor electrode top view after step (iii). ....	27
Figure 6. Photomicrograph of a test sensor after electrical operation. The deformation of gold electrodes first appears on the anode, where oxygen is formed. The wrinkles align with the mesh structure in areas where the hole density is low. ....	28
Figure 7. Fabrication process of the oxygen sensor incorporating PDMS as the oxygen-permeable membrane.....	30
Figure 8. Optical image of the fabricated sensor. ....	31
Figure 9. The fabrication process of electrolyte reservoir featuring FEP membrane. ....	32
Figure 10. Process of sealing the holes in the sensor substrate from the backside using Dymax 3401. (a) Apply a thin layer of Dymax 3401 to the laser-ablated holes on the back side. (b) UV light was applied to cure Dymax 3401 and therefore seal the electrolyte reservoir. (c) Sensor filled with electrolyte and sealed from the back. (d) Water electrolysis decomposes water to form a large bubble. ....	34
Figure 11. Circuit schematic of the customized potentiostat connected to a three-electrode oxygen sensor.....	37
Figure 12. (a) Schematic and (b) layout for the potentiostat and wireless transmission board. ....	38
Figure 13. The process flow of the customized potentiostat controlled by a remote board. ....	40
Figure 14. Electrical response of the fabricated electrochemical sensor. (a) Linear sweep voltammogram for a sensor tested within oxygen concentrations of 0.5%, 11%, 23%, 47%, 75%, 95% with respect to atmospheric oxygen. (b) The diffusion-limited-current/calibrated-O <sub>2</sub> -concentration relationship. The sensor demonstrated linearity across a range of physiologically relevant concentrations. ....	42
Figure 15. LSV curves of the same sensor tested under saturated oxygen concentration. ....	43
Figure 16. Response characterization of the fabricated sensor with different oxygen permeable membranes. ....	44
Figure 17. Response characterization of the fabricated sensor at 20 °C and 37 °C.....	45
Figure 18. (a) The stability results of the fabricated electrochemical oxygen sensor at room temperature by measuring the diffusion-limited reduction currents at a full-oxygen state 40 times sequentially. (b) The sensitivity results of 3 sets of tests. ....	47

Figure 19. (a) The stability results of the fabricated electrochemical oxygen sensor at 37 °C by measuring the diffusion-limited reduction currents at a full-oxygen state 80 times sequentially. (b) The sensitivity results of 3 sets of tests. ....	48
Figure 20. Life time characterization of the fabricated oxygen sensor at room temperature. Data obtained from customized sensor (black circles) are cross-referenced to a commercial oxygen sensor (orange line). ....	49
Figure 21. Life time characterization of the fabricated oxygen sensor at room temperature by measuring the diffusion-limited reduction currents at a full-oxygen state over 2 weeks. The insets showed simple test results of the sensitivity in day 1 and day 14. Data obtained from customized sensor at oxygen-depleted state and full-oxygen state is cross-referenced to a commercial oxygen probe.....	50
Figure 22. Front and back side of the wirelessly-controlled potentiostat circuit board. The overall dimension of the PCB board is 2 cm × 3 cm × 8 mm.....	51
Figure 23. (a) Raw data of LSV testing over a 1 MΩ resistor using the customized potentiostat platform with a 1.2 MΩ feedback resistance and (b) Corresponding current noise. (c) Noise standard deviations as a function of feedback resistance. ....	53
Figure 24. End to end testing and calibration of the oxygen sensing system. (a) LSV data obtained from customized potentiostat. (b) Corresponding current measured from the full system calibrated to a commercial oxygen sensor. ....	55
Figure 25. Optical image of (a) the fabricated sensor; (b) wire and solder pad before and after soldering. ....	61
Figure 26. The change in oxygen concentration with time and distance as the bias voltage increases in LSV measurements.....	63
Figure 27. Estimated oxygen concentration gradients at the transition point from kinetic-controlled region to diffusion-limited region.....	63
Figure 28. Sensitivity characterization of the fabricated electrochemical oxygen sensor. (a) Oxygen tensions measured periodically by LSV every 20 minutes. (b) Output current of the customized sensor cross referenced to the oxygen measurement from the commercial oxygen sensor.....	67
Figure 29. LSV curves for a sensor tested under saturated oxygen state at 5 mV/s, 25 mV/s, 125 mV/s and 625 mV/s, respectively. ....	68
Figure 30. Sensor readout at both full-oxygen and oxygen-depleted states in PVA solutions with a PVA/water mass ratio of 0:1, 1:9 and 1:4, respectively.....	69
Figure 31. The sensitivity results of the sensor tested in solutions with pH values of 5.2 and 7.8, respectively. ....	70
Figure 32. End to end testing of the oxygen sensing system <i>in vivo</i> and <i>ex vivo</i> . ....	71
Figure 33. <i>In vivo</i> test results for mouse and zebrafish models, respectively.....	72
Figure 34. <i>In vivo</i> result of oxygen level in mouse and fish models. The average oxygen levels of mouse glueous muscle and fish trunk muscle are 36 Torr and 24 Torr, respectively (n=15 each).....	73
Figure 35. A pictorial history of the sensor pad over a one-week duration. ....	74
Figure 36. Schematic diagram of immobilized electrolyte biodegradable battery. ....	80
Figure 37. The principle of operation of the biodegradable battery. Liquid absorbed into the cell activates the battery by converting solid NaCl into a super saturated NaCl	

solution. Na <sup>+</sup> and Cl <sup>-</sup> , as well as hydrogen gas, leach out from the PCL film. The governing chemistry in the electrolytic cell is the cathodic protection of Fe through the oxidation of Mg anode and, parasitic corrosion of the Mg. ....	83
Figure 38. The schematic diagram of the circuit model. ....	84
Figure 39. Fabrication process of the battery. ....	88
Figure 40. NaCl leach rate of the NaCl/PCL composite structure with top PCL membrane thickness of 0 $\mu\text{m}$ , 20 $\mu\text{m}$ , 50 $\mu\text{m}$ , 80 $\mu\text{m}$ , respectively. ....	89
Figure 41. Discharge behavior upon activation of four batteries with the same configuration and discharge parameters. ....	90
Figure 42. Discharge behavior of a battery removed from DI water after being discharged for 24 hours. The battery terminates in 6 hours due to liquid loss, and resumes its performance shortly after reimmersion in water for a second time. ....	91
Figure 43. Discharging behavior under constant current. The operating voltages are approximately 0.95 V, 0.75 V and 0.45 V for discharge rates of 12.5 $\mu\text{A}/\text{cm}^2$ , 25 $\mu\text{A}/\text{cm}^2$ and 0.1 $\text{mA}/\text{cm}^2$ , respectively. ....	92
Figure 44. Battery terminal voltage at different discharge currents. $V_t$ changes nonlinearly with $I$ at smaller currents. ....	93
Figure 45. Discharging behavior under a constant current of 25 $\mu\text{A}/\text{cm}^2$ . The liquid volume outside of the battery was changed every one hour. ....	94
Figure 46. Schematic diagram of the biodegradable sensor. ....	99
Figure 47. The sensor is discharged at varying current densities. The blue line is the discharge current density of the sensor. The dashed black line is the output voltage in an oxygen-depleted sample electrolyte, while the solid black line is the output voltage in an oxygen-saturated sample electrolyte. ....	101
Figure 48. the test circuit of the sensor. The DC equivalence of the sensor is inside the dashed box. The external test circuit draws a controlled current from the sensor. ....	103
Figure 49. Galvanodynamic measurements of the Mg-Mo pair and the individual electrodes at a scan rate of 0.01 $\text{mA}/\text{cm}^2 \cdot \text{s}$ . ....	104
Figure 50. An example of a PCL-supported Mg-Mo electrochemical couple supported on PLA being subjected to the test method described in section 5.2.3. The output voltage of the electrochemical couple is measured as a function of time. During battery mode, a current of 1 $\text{mA}/\text{cm}^2$ is being drawn from the couple. During open circuit mode, no current is drawn from the couple. During sensor mode, a current of 0.02 $\text{mA}/\text{cm}^2$ is drawn from the couple. In sensor mode, the output voltage is representative of the electrolyte oxygen concentration. The process is then repeated to understand the time history of oxygen concentration in the environment. ....	105
Figure 51. Testing result of the sensor in both oxygen-saturated and oxygen-depleted state. (a) The discharge current is alternated between battery mode and sensor mode during each measurement; (b) output voltage in sensor mode extracted from (a). Stable operation is observed. ....	107
Figure 52. Output voltage of the sensor at constant discharge current (i.e., sensor mode only) in both oxygen-saturated and oxygen-depleted states. Sensor drift is observed. ..	107
Figure 53. Response characterization of (a) Mg-Fe, (b) Mg-W and (c) Mg-Mo sensors at a discharge current density of 0.02 $\text{mA}/\text{cm}^2$ . At each measurement point, sensor	

interrogation protocol followed the waveforms of Fig. 50 (battery mode, open circuit mode, sensor mode).....	109
Figure 54. (a) Optical image of the sensor and cotton-like deposits observed on anode after an hour of testing; (b) The stability results of biodegradable oxygen sensor by measuring output voltage at a full-oxygen state 10 times sequentially. Sensor sensitivity is validated by measuring in oxygen depleted state before and after the stability test. (c) Optical image of sensor surface after discharge for an hour at a low current density of $0.02 \text{ mA/cm}^2$ . ....	112
Figure 55. A 2D map of the oxygen distribution in the electrolyte after applying a current to the electrodes using COMSOL Multiphysics. ....	115
Figure 56. Simulated and experimental results of the dependence of oxygen concentration as a function of cell voltage. The experimental cell was an Mg-Mo couple discharged in sensor mode at a current density of $0.04 \text{ mA/cm}^2$ . At each measurement point, sensor interrogation protocol followed the waveforms of Fig. 50 (battery mode, open circuit mode, sensor mode).....	116

## CHAPTER 1 INTRODUCTION

### 1.1 Oxygen sensors for biomedical applications

#### 1.1.1 Medical need for oxygen sensing in the body

Oxygen plays an important role in the metabolism of the human body. Appropriate levels of oxygen are vital to support cell respiration. In humans, apnea for more than one minute causes serious lack of oxygen in blood vessels; three minutes' discontinuance of oxygen supply leads to permanent damage of the brain. The human body uptakes oxygen from ambient air through the lungs. During respiration, air passes into finer tubes called bronchioles and reaches a cluster of tiny air sacs called alveoli, where gas exchange occurs. Oxygen entering the alveoli dissolves through a membrane into blood vessels surrounding each alveolus, and then is transferred to tissues and organs by cardiovascular system. Dissolved oxygen is used by cells and tissues in most multi-cellular species for the oxidation of molecules. Most importantly, oxygen is used in the electron transfer oxidase system where it helps form phosphate bonds in ATP. These processes of chemical and physical changes go on continually in the human body: build-up of new tissue, replacement of old tissue, conversion of food to energy, disposal of waste materials, and reproduction. [1]–[4]

Since molecular oxygen is a critical requirement for aerobic metabolism and cellular function, it can be used as a direct assessment for a wide range of biological effects. Oxygen-based cues already play an important role in medical diagnostics and decision making by several medical specialties such as wound care and hyperbaric medicine. For

instance, tissue oxygen data is a direct assessment for predicting potential candidates for hyperbaric oxygen (HBO<sub>2</sub>) therapy [5]. In wound care treatment, oxygen level assessment is principally used to help determine amputation level (i.e., how high up a limb amputation should take place) and to estimate healing potential, identify the presence of hypoxia in wounded tissue, and predict the response to hyperoxia and determine when HBO<sub>2</sub> therapy is complete. In addition, oxygen level monitoring as a diagnostic method has attracted significant interest in areas from mitochondrial diseases to tissue engineering/regenerative medicine. For instance, local oxygen tension is of particular interest to clinicians and scientists studying mitochondrial diseases [3], [6]–[8]. Theoretical studies have shown that the most common symptomatology in mitochondrial disease is myopathy, which leads to elevations in whole body and tissue oxygen levels due to impaired muscle oxygen extraction efficiency. The ability to acquire *in vivo* intramuscular measurements of oxygen tension would significantly enhance the information available to clinicians and scientists to monitor and evaluate mechanisms of mitochondrial diseases or lack thereof. Also, scientists are seeking a better understanding of the role of oxygen in bone fracture healing [9]. Theoretically, the healing mechanism is dependent on the rate of revascularization and the local reestablishment of physiological oxygen tension. Correlation of longitudinal parameters with quantitative measures of *in situ* oxygen tension would provide a rational approach for the design of improved regenerative strategies.

Novel oxygen sensing techniques are a promising approach to facilitate *in vivo* measurements for numerous injuries and diseases of interest. Various attempts have been

made to achieve in-situ oxygen level monitoring. Thanks to continued technological advances, short-term in-situ testing of oxygen tension has been made possible for evaluating related biological processes. For instance, Brighton and Krebs [10] measured oxygen tension in a rabbit fibular fracture using electrochemical oxygen sensors inserted at each time point. They noted marked differences and temporal trends of the oxygen tension in the hematoma, woven bone, and intact diaphyseal bone. Tissue oxygen measurements with respect to soft-tissue wound healing have also been conducted using polarographic electrodes to confirm hypoxia in chronic, indolent human wounds and to show that oxygen is delivered to wounds during HBO<sub>2</sub> treatment. However, most of the existing sensors only provide short-term measurement for subcutaneous, transcutaneous and intraoperative oxygen monitoring [11]. We see an exciting opportunity to develop sensors for long-term, continuous oxygen monitoring to enhance preclinical development for a number of relevant diseases. Moreover, for clinical practice where decision-making is based on historical results, the development of post-surgery, chronic oxygen sensing techniques has great potential in transforming clinical trials where repeatable, objective outcome measures are lacking.

#### 1.1.2 Electrochemical oxygen sensors

Electrochemical sensors are one of the most widely used diagnostic tools in clinical analysis, environmental monitoring, and the food industry, due to their rapid response, low cost, and ease of applicability in the field. The ability to safely and reliably detect oxygen tension over semi-chronic time periods (e.g., weeks to months) is extremely

desirable. The Clark cell is a well-established method for measuring dissolved oxygen concentration based on electrochemical principles [12]. The technology has been well-studied and sensors based on this method are commercially available. However, the sizes of the commercial sensors have precluded their use in clinical applications. In addition, many commercial oxygen sensors incorporate hazardous chemicals such as lead or inorganic acids, rendering them less suitable for food industry, environmental or *in vivo* monitoring. As such, current electrochemical oxygen sensors are not optimally suited for continuous monitoring of the oxygen environment in the body. Key challenges and opportunities remain in developing implantable oxygen sensors for continuous, *in vivo* monitoring.

## **1.2 Implantable MEMS technologies**

Continued advancements in material and fabrication technologies utilized by microelectromechanical systems (MEMS) has created an opportunity to implant small, flexible, low-power sensors into preclinical and clinical *in vivo* models, and quantitatively measure environmental parameters in the body. Since implantable devices have to interface with the local physiological environment, which is a dynamic system responding to foreign devices, achieving the required sensitivity and stability is often countered by host inflammatory or fibrous encapsulation response to chronic implants [13], [14]. Extensive research has focused on improving implant biocompatibility, through physical and chemical modifications to tissue-device interfaces with the goal of prolonging device lifetime [13], [15]–[22]. Materials aimed at reducing tissue damage



inflicted by the device at the implant site, better emulating the material properties of the host tissue, and improving biocompatibility have been investigated. These include flexible and polymeric materials, hybrid composites, and biological materials, such as proteins, cells, and tissues, that may be considered for implantable applications for continuous, *in vivo* monitoring [21].

### 1.2.1 Flexible devices for implantable applications

Flexible implantable MEMS devices are very attractive for medical applications, as their less rigid nature may reduce local damage and thereby improve the host foreign body response. Flexible devices that can be bent, stretched, or twisted to adapt to the local tissue geometry can minimize irritation and improve conformal contact with the physiological environment [23]. The availability of low-cost manufacturing and rapid prototyping methods with plastic materials has also contributed to the development of flexible devices. The use of flexible polymeric materials, such as parylene and polyimide, for clinical applications continues to increase steadily due to their biocompatibility and ease of processing with traditional microfabrication technologies [15]. In 2001, a polyimide-based multichannel intracortical electrode array was manufactured with standard, planar, photolithographic, and CMOS-compatible techniques. Polyimide served as the mechanically flexible substrate that was manipulated into unique three-dimensional designs. The array was electrically interfaced with an integrated polyimide cable to provide efficient contact points for a high density of channels [24]. Another example is a wireless, passive, radio frequency pressure sensor for long-range continuous intraocular

pressure monitoring for glaucoma patients. The sensor featured parylene-C (poly-chloro-p-xylylene) as the encapsulant and sensing membrane. The flexible coil substrate can be folded into a smaller form factor to enable minimally invasive implantation (e.g., catheter-based deployment) and, subsequently, can naturally unfold to its original state without damage. Long-term and short-term device testing in a six-month *in vivo* model and acute *ex vivo* model, respectively, verified the feasibility and efficacy of the sensor, including robust fixation and long-term biocompatibility in the intraocular environment [25].

## 1.2.2 Toward biodegradable systems

### 1.2.2.1 Biodegradable materials

Biodegradable materials refer to a class of advanced materials that can completely dissolve or disintegrate with biologically benign byproducts in water and biofluids. The most commonly used bioresorbable materials include synthetic water-soluble polymers, aliphatic polyesters and dissolvable metals [26].

A typical example of synthetic water-soluble polymers used in bioresorbable electronics is poly(vinyl alcohol) (PVA) [27]. It is capable of rapid and reversible dissolution in water for biomedical purposes. PVA is reported being utilized as the substrates, encapsulation, and dielectric layers for various devices, such as field effect transistors (FETs) and Li-ion batteries. In transient Li-ion batteries, PVA thin films offer multiple

functions as substrate, separator, and battery packaging. The reported transient Li-ion battery packaged using PVA is disintegrable within 5 min in alkaline solution [26].

Aliphatic polyesters, such as poly(lactic acid) (PLA), poly(glycolic acid) (PGA), poly(lactic-co-glycolic acid) (PLGA) and polycaprolactone (PCL) are some of the key materials for biomedical applications including tissue engineering devices and body implants [28]. Unlike water-soluble polymers, aliphatic polyesters chemically degrade in water/biofluids due to the hydrolytically unstable ester linkages in the backbone chain. Dissolution of aliphatic polyesters is much slower compared to water-soluble PVA, typically completed in months. Their dissolution rate is controllable by adjusting the molecular weight and chemical composition during the synthesis processes. For example, degradation of PLGA can be decelerated by increasing the ratio of lactide to glycolide to enhance hydrophobicity and retard swelling [29].

These biodegradable polymers can easily be processed by solvent casting, spin casting, hot melting, and electrospinning. Their thermal stability and solvent compatibility are summarized in Table 1 [26].

Table 1. Thermal stability and solvent compatibility of discussed biodegradable polymer.

	Thermal stability	Water	Acetone	Alcohol
PVA	$T_g$ : 83 °C $T_m$ : 203 °C	Soluble	insoluble	insoluble
PLA	$T_g$ : 45–65 °C $T_m$ : 173–178 °C	hydrolyzed	soluble	insoluble
PCL	$T_g$ : –65 to –60 °C $T_m$ : 58–63 °C	hydrolyzed	insoluble	insoluble
PLGA	$T_g$ : 40–55 °C	hydrolyzed	soluble	insoluble

In electronic systems, metals always play important roles in devices and circuits. The corrosion of metal, a normally undesirable phenomenon, however, can be utilized as a useful property for certain metals in biodegradable applications. In addition to solubility, they are required to be biocompatible and relatively stable to survive the fabrication processes. Magnesium (Mg) and its alloys are the most well-known biocompatible and biodegradable metals due to their combination of high mechanical strength, fracture toughness, and non-toxicity [30]. Besides Mg, alternative dissolvable metals, including zinc (Zn), iron (Fe), tungsten (W) and molybdenum (Mo), as listed in Table 2, have been explored in broad applications of biodegradable electronics, such as transistors, sensors, and energy devices [31], [32]. When exposed to biofluids, these materials undergo corrosion and produce soluble ions, hydroxides, and/or oxides [32].

Table 2. Biodegradable metals and their corrosion-related characteristics

	Dissolving mechanism	$E^\circ$ [V]	Mass lost corrosion rates [ $\mu\text{m/h}$ ]
Mg	$\text{Mg} + 2\text{H}_2\text{O} \rightleftharpoons \text{Mg}(\text{OH})_2 + \text{H}_2$	-2.372	pH 7.4 SBF 37 °C: 0.05–0.5
Fe	$\text{Fe} + 2\text{H}_2\text{O} \rightleftharpoons \text{Fe}(\text{OH})_2 + \text{H}_2$	-0.447	pH 7.4 SBF 37 °C: $\approx 0.02$
W	$2\text{W} + 2\text{H}_2\text{O} + 3\text{O}_2 \rightleftharpoons 2\text{H}_2\text{WO}_4$	-0.119	pH 7.4 SBF: 0.02–0.06
Mo	$2\text{Mo} + 2\text{H}_2\text{O} + 3\text{O}_2 \rightleftharpoons 2\text{H}_2\text{MoO}_4$	-0.152	pH7 buffer: $1 \times 10^{-3}$

#### 1.2.2.2 Biodegradable sensors, batteries and circuits

As biodegradable materials have been greatly explored, the idea of biodegradable devices has been brought forward. Biodegradable devices are sensors and actuators that break down after a targeted functional lifetime into nontoxic components that may either be resorbed or expelled by the body. This feature may overcome the complications associated with permanent implants for applications that are transient in nature, such as bone healing. Further, the resorbable nature eliminates the need for secondary surgery to extract the implant. A typical example is the passive wireless pressure sensor demonstrated by our group [33], [34]. The pressure sensor comprises flexible plates bearing inductor windings to form a resonant electrical circuit with the capacitor and to magnetically couple with an external loop. Zinc/iron bilayers were used as the sensor conductor material, and biodegradable polymers poly-L-lactide (PLLA) and polycaprolactone (PCL) were used as dielectric and structural materials. The fabricated sensor demonstrated a linear frequency response with external applied pressure. The functional lifetime of the sensors was approximately 4 days, and can be tailored by the choice of polymer encapsulation and area ratio of the bilayer galvanic couple.

Previously reported biodegradable MEMS sensors (i.e., as described above) are mostly passive, with no need for an internal power source or circuitry, and by necessity limited in functionality [35]. It is therefore useful to consider the incorporation of active elements to achieve a full electrical system. The power consumption of an active device, however, demands the exploration of biodegradable batteries as viable energy sources [36]–[38]. Our group has presented a magnesium/iron battery featuring PCL as the packaging and

functional material [30]. Compared with medical-grade nondegradable lithium-ion batteries at similar size scales, the PCL-coated Mg/Fe batteries showed superior performance of up to six times higher in energy density and 1–2 orders of magnitude reduction in volume.

In order to achieve a full electrical system, a biodegradable printed circuit board (PCB) or equivalent interconnect structure providing mechanical supports and electrical interconnections for mounted components must be addressed. Huang et. al demonstrated a multilayer transient PCB with performance comparable to that of conventional devices, but with the capability for dissolving into benign end products upon immersion in water [39]. This work demonstrates fully biodegradable circuit components which are critical to ultimately achieve a physiologically integrated MEMS system possessing multiple sensing modalities.

### **1.3 Research objective and thesis outline**

The objective of this thesis is to improve the current oxygen sensing technology to the point that it could be used for long-term *in vivo* applications, and further develop a biodegradable oxygen sensor along with a transient energy source to support the design of completely biodegradable oxygen sensing systems. As shown in Fig. 1, the outline of this thesis can be divided into two parts: 1) to design, build and test a biocompatible oxygen sensor, integrate it with a customized circuit and an off-the-shelf battery, and validate its feasibility for both *in vitro* and *in vivo* applications; 2) to develop a

biodegradable Mg-Fe battery and a transient galvanic oxygen sensor and examine their performance *in vitro*.

	Implantable oxygen sensing system		
	Sensor	Circuit	Power
<b>Gen 1 Biocompatible</b>	Electrochemical sensor <ul style="list-style-type: none"> <li>• Biocompatible</li> <li>• Satisfy physical constraints of rodent model</li> </ul>	Customized circuit <ul style="list-style-type: none"> <li>• Driver circuit</li> <li>• Control unit</li> <li>• User interface</li> </ul>	Off-the-shelf battery
	Prove by <i>in vitro</i> & <i>in vivo</i> applications		
<b>Gen 2 Biocompatible &amp; Transient</b>	Galvanic sensor <ul style="list-style-type: none"> <li>• Biodegradable</li> <li>• Achieves form factors comparable to biocompatible sensors</li> </ul>	Silicon-based circuit* (Huang et al., 2017)	Mg-Fe battery <ul style="list-style-type: none"> <li>• Biodegradable</li> <li>• Achieves feature sizes similar to coin cell battery</li> </ul>
	Prove by bench top experiments		

\* Use non-degradable circuit here to validate sensor & battery

Figure 1. Dissertation outline.

The present chapter reviewed the importance of oxygen-based cues in biological processes, and the current technology development in electrochemical oxygen sensors, implantable MEMS and biodegradable sensors, batteries and circuits.

Chapter 2 will present the fabrication and characterization of a freestanding, miniaturized electrochemical oxygen sensor. The sensor is fabricated on a flexible and biocompatible polyimide substrate using lithographic techniques, and singulated with an excimer laser. The sensor consists of a round-shaped planar sensing portion (diameter: 2.4 mm, thickness: 180  $\mu$ m), and metal lines and contact pads for connection with external

analytical tools. The sensing portion is comprised of three electrodes (working, counter and reference electrodes), an electrolyte reservoir filled with liquid electrolyte, and a semipermeable membrane for oxygen introduction. The electrodes are patterned using a single layer of gold without adhesion layer to eliminate any multilayer metallic structure in the sensing region. Both polydimethylsiloxane and fluorinated ethylene propylene semipermeable membranes are characterized. The fabricated sensor demonstrated an oxygen response of -14 nA/atm.% and good linearity. This device is integrated with a customized potentiostat circuit and a microcontroller with data process and wireless transmission capability for applications such as monitoring oxygen tension in biomedical-related applications over semi-chronic time periods.

Chapter 3 will further demonstrate the feasibility of the prototype oxygen sensing system described in Chapter 2 for *in vivo* applications. Sensors with smaller planar footprint are designed and fabricated to adapt to mouse and zebrafish models. Linear sweep voltammetry with a scan rate of 25 mV/s is used to overcome the mismatch in oxygen diffusion rate between the calibration and *in vivo* testing environment. Oxygen levels in mouse gluteus muscle and zebrafish trunk muscle are both investigated to validate the sensor's ability to monitor dynamic oxygen tension *in vivo*.

Chapter 4 will demonstrate a biodegradable battery featuring a solid electrolyte of sodium chloride and polycaprolactone. This approach harnesses the body fluid that diffuses into the cell as an element of the electrolyte; simultaneously, the large excess of sodium chloride suspended in the polycaprolactone holds intracellular ionic conditions constant. A constant discharge profile can then be achieved even in the presence of varying external



aqueous conditions, enabling compact, stable-performing cells. This design also features easy integration and automatic activation, providing a simplified strategy to fabricate batteries with long shelf life and desirable functional life span. In addition, the polymeric skeleton of the solid electrolyte system acts as an insulating layer between electrodes, preventing the metallic structure from short-circuit during discharge.

Chapter 5 details the design, fabrication and characterization of a completely biodegradable dissolved oxygen sensor. The sensor features a Mg-Mo galvanic pair and operates at alternating discharging currents. The principle of operation is the competition of oxygen reduction reaction against the dominating hydrogen reduction reaction at the cathode, leading to a positive shift of the cell potential that corresponds to the oxygen availability in the vicinity of the cathode. This approach measures physiological oxygen tension in a transient, harmless manner in the body, while simultaneously acting as a potential energy source for additional devices.

Chapter 6 will conclude this dissertation and present possible future work.

## CHAPTER 2 MICROFABRICATED OXYGEN SENSOR FOR BIOMEDICAL APPLICATIONS

### 2.1 Background and motivation

Oxygen cues are critical assessments for a variety of biological processes. For instance, theoretical studies have shown that local oxygen tension appears to be an important factor in bone regenerative processes. The ability to acquire real-time measurements of oxygen tension within the regenerative niche *in situ* would significantly enhance the information available to tissue engineers to monitor and evaluate mechanisms of functional healing or lack thereof [9]. However, electrochemical oxygen sensors that are commercially available satisfy neither the size nor biocompatibility requirements needed for *in vivo* monitoring [40]. Development of a miniaturized, biocompatible and disposable electrochemical oxygen sensor with long shelf and functional lifetime that does not contain hazardous materials may be desirable for biomedical applications.

An electrochemical oxygen sensor comprises three elements: electrodes, liquid electrolyte, and an oxygen permeable membrane. When a voltage is applied between electrodes, the current generated by electrochemical oxidation/reduction (redox) reactions is proportional to the dissolved oxygen content that has diffused through the oxygen permeable membrane into the liquid electrolyte, thus providing transduction. For the realization of a miniaturized electrochemical sensor, a significant challenge lies in the fabrication of a set of reliable and durable electrodes, as well as the incorporation of a miniaturized reservoir to store the liquid electrolyte in the electrochemical cell.

There have previously been attempts to fabricate electrochemical oxygen sensors using microfabrication technologies. A typical example is the thin-film Ag/AgCl structure demonstrated by Suzuki et al. [41]. In this structure the entire surface of the thin-film pattern was covered with a hydrophobic polymer layer leaving slits at the edges of the pattern, rendering the AgCl layer less susceptible to deterioration during sensor operation. However, the open circuit potential of the Ag/AgCl element was maintained for only 3–5 days after injection of electrolyte, after which a rapid negative shift of potential was observed. The stability and durability of the electrodes still are limiting factors to the shelf life and functional lifetime of the sensor [42]–[47]. Noble metals, such as platinum and gold, have also been used as the electrodes. Park et al. [48] demonstrated a reservoir-type oxygen sensor featuring gold electrodes; a lifetime test showed that the response current abruptly changed over 20% after 10.6 hours. Wu et al. [49] reported a Clark sensor chip consisting of a glass substrate and platinum electrodes, and the results showed that the difference of the relative responses from the first response increased 10% after 50 minutes. The fluctuations in sensor response were suspected to be attributable to the change in surface status of the electrodes, and the shift in potential of the reference electrodes, but little has been further explored to improve their performance in stability and lifetime.

Another challenge in the design and fabrication of a miniature electrochemical oxygen sensor is the integration of the electrodes with an electrolyte and oxygen-permeable membrane system that supports compact packaging. To form a compartment for the internal electrolyte, previous studies mainly attached a separate electrolyte reservoir to a

chip to form a microfluidic system [50][51]. Although this process provides a simple and reproducible fabrication process, the overall dimension of the sensor is increased. In addition, for applications such as implantable and wearable biomedical sensors, good flexibility is required to reduce discomfort. However, the reported miniature electrochemical oxygen sensors generally lack flexibility and substrate and electrode failures due to mechanical stress have been observed. Further, most Clark-type sensors developed in the lab are characterized using a commercially available laboratory potentiostat, which is usually a bulky system and further compromises the sensor's portability for clinical use [52]–[57].

In an attempt to develop a miniaturized electrochemical sensor with good response to oxygen, various materials, structures and dimensions, as suggested by reported literature were evaluated on the basis of sensor performance, and designs that could optimize their use for electrochemical oxygen sensors were investigated. This chapter presents the development of a MEMS-based electrochemical sensor for monitoring of dissolved oxygen across a range of physiologically relevant concentrations. Specifically, this design comprises an oxygen permeable membrane, a freestanding electrolyte reservoir and a set of gold electrodes. Two oxygen permeable polymers, polydimethylsiloxane (PDMS) and fluorinated ethylene propylene (FEP), were investigated. The overall dimension of the sensor is  $2.5 \text{ mm} \times 6 \text{ mm} \times 0.3 \text{ mm}$ . A customized potentiostat platform with nanoampere current measurement and wireless data transmission capability was developed. Depending on the size constraints of the anatomical space under investigation, transceiver and circuitry components could be packaged within a single device or wires

could be routed to a remote transceiver pack mounted either intraperitoneally or subcutaneously in implantable applications.

Earlier work on microfabricated electrochemical oxygen sensors mainly focused on Ag/AgCl or platinum reference electrodes, while few, if any, aqueous-based three-gold-electrode freestanding oxygen sensors have been reported. This work demonstrates a freestanding, disposable gold-based oxygen sensor with improved flexibility. The gold electrodes are single-layer noble metallic structures without any consumable parts, which avoids many of the problems with dimension and performance seen with existing miniature electrochemical oxygen sensors. In addition, a new fabrication process is developed to integrate the FEP membrane. The devices exhibit good response and prolonged shelf and functional lifetime. Further, the sensor can be bent in the non-functional region without alternating the redox current, demonstrating good flexibility for applications involving mechanical loading. For instance, the sensor can be integrated with the structural implant to monitor oxygen tension during bone regeneration in a rodent femoral defect model [9]. The contact pad region can be anchored to the bone fixation plate, while the oxygen-sensitive part of the sensor is inserted into the bone defect. In this application, substrate flexibility of the planar sensor is important for accommodating the slight vertical displacement of the contact pad region and bending in the middle of the sensor induced by force loading at the structural implant.

## 2.2 Working principle

The basic principle of electrochemical oxygen sensors is the measurement of the current-potential relationship in an electrochemical cell, operated by measuring the electrical signal resulting from analyte reactions at the electrode. As shown in Fig. 2, the electrochemical oxygen sensor comprises three elements: electrodes, liquid electrolyte, and an oxygen permeable membrane. Oxygen molecules that come in contact with the sensor first permeate through a membrane, which also serves as protection against non-target molecules. The oxygen molecules then diffuse through the inner electrolyte to reach the surface of the working electrode (also known as the sensing electrode). There the molecules are reduced, consequently consuming electrons, and thus generating an electric current. The reduction reaction is a multielectron reaction often associated with the formation of reaction intermediates. Several reaction mechanisms have been suggested [58]:

(i) A direct four electron reduction to  $\text{H}_2\text{O}$ :



(ii) A two-electron pathway involving reduction to hydrogen peroxide:



(iii) A four-electron process reduction that occurs in two steps:



The current is proportional to the rate of reaction at the sensing electrode, the potential of which is commonly regulated using the reference electrode. The reference electrode

provides a constant potential and serves to maintain the voltage of the sensing electrode at desired values. The electrochemical cell is completed by the counter electrode which balances the reaction at the working electrode. The ionic current between the counter and sensing electrode is transported by the electrolyte inside the sensor body, whereas the external current path is provided by the potentiostat circuits.

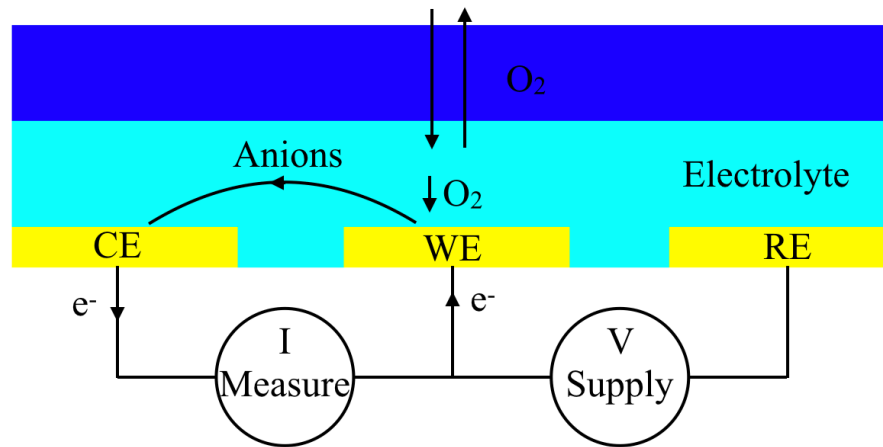


Figure 2. Operation of an electrochemical oxygen sensor. A potentiostat is used as the external circuit to apply a voltage and measure current. When a negative potential is applied from the circuit across the working and reference electrodes, oxygen in contact with the working electrode is reduced, thus generating an electric current.

## 2.3 Biocompatible Material Selection

### 2.3.1 Electrode material

Ag-AgCl/ $\text{Cl}^-$  is a self-contained electrochemical system, which makes it a good candidate as a reference electrode for many industrial applications where the electrochemical potential must be accurately measured or controlled. Due to its stability and simplicity of fabrication, macroscopic Ag/AgCl structures are commonly used as the reference

electrode in commercial oxygen sensors. A macroscale Ag/AgCl/KCl system can provide a stable reference potential for the reduction reaction on the cathode. In addition, silver can also serve as the anode, providing material for the oxidation reaction. However, reducing the dimensions of the silver and silver chloride for miniaturized sensors may cause complications in device operation [40]. Specifically, silver can be consumed by chloridization and silver chloride reacts with chloride ions ( $\text{Cl}^-$ ) to form a soluble product in solutions with high  $\text{Cl}^-$  concentrations. At reduced size configurations, the electrochemical and chemical stability of silver and silver chloride becomes a limiting factor in shelf life or functional lifetime of the oxygen sensor. Second, the silver chloride thin film structure can be damaged under mechanical stress, which makes it less desirable for flexible substrates or applications involving mechanical loading.

A thin-film noble metal structure is another option for electrodes; this choice features inexpensive fabrication, as well as prolonged shelf and functional life. The inertness of the electrode material decreases the risk of electrode deterioration during measurement, which might lead to a large alteration of the electrolyte composition in a small, volume-constrained electrolyte chamber. In addition, an inert counter electrode can eliminate the consumption of anodic material, providing a relatively long-term functional lifetime. However, the potential of a pure metal electrode is not well defined and susceptible to instability. Drift in the reference electrode potential can cause quantitative errors in data collection beyond simple inaccuracies in the measured potential. Fortunately, this shortcoming can be overcome by using linear sweep voltammetry (LSV) for low frequency characterization, as discussed later in this study.



A three-electrode system built with a single metal, such as gold or platinum, is selected to satisfy all relevant design requirements. Although gold is less noble than platinum, it was experimentally observed that gold-based sensors demonstrated less drift than platinum-based sensors. This may be attributed to hydrogen absorption on the platinum electrodes, which causes a larger potential shift compared to gold throughout the measurement duration. The remaining, slight drift in reference potential can be overcome by using LSV for characterization. As a result, gold was selected as the material for all three electrodes.

### 2.3.2 Oxygen permeable membrane material

The oxygen transport rate through the membrane is one of the most important factors that affects the response of the oxygen sensor. Polydimethylsiloxane (PDMS) has been widely used as the membrane material for its high oxygen permeability (i.e., 600 Barrer) [48]. Fluoropolymer is another good candidate for the oxygen-permeable membrane. Compared with PDMS [52], fluoropolymers have several advantages [48], [53], such as less absorption of small molecules and biomolecules, and less leaching of irrelevant molecules from the environment into the electrolyte in the reservoirs. The oxygen permeability of fluorinated ethylene propylene (FEP) is 5.9 Barrer [48], which is relatively high among fluoropolymers, rendering FEP another candidate for the membrane. Among the polymers, polyimide possesses high thermal and hydrolytic stability, excellent chemical resistance, excellent adhesion properties and good mechanical strength. Therefore, PDMS, FEP and commercial polyimide films (Kapton

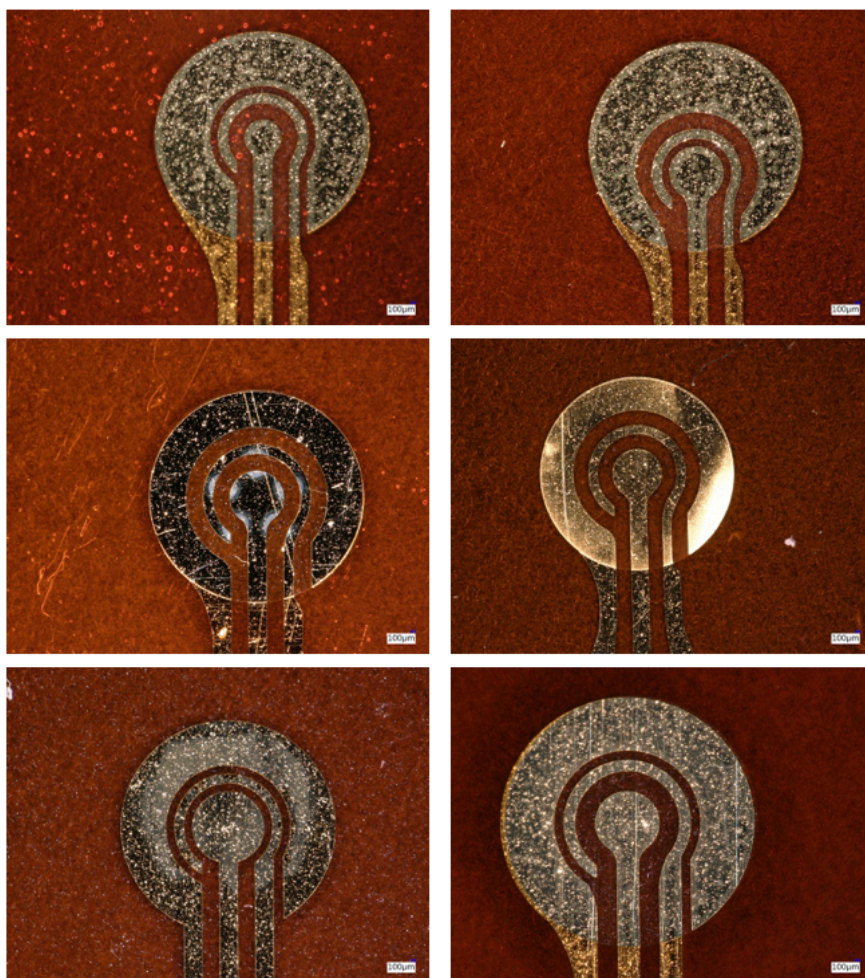
HN, Dupont) were chosen as the membrane material and device substrate, respectively; oxygen sensors based on these polymers are fabricated and characterized.

## **2.4 Design and fabrication**

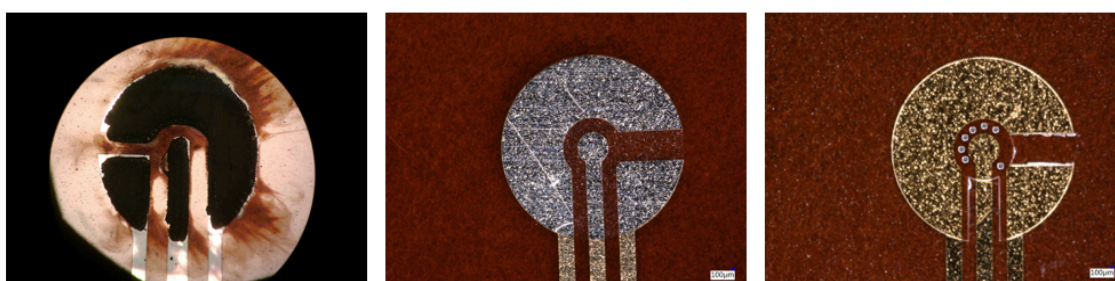
### **2.4.1 Design and fabrication of sensor electrodes**

Several electrode design issues are considered to improve device response and sensor stability. To achieve a sufficiently high output signal and therefore response, the sensor requires a sufficient working electrode area to support oxygen reduction. However, the dependence of the output current on cathode area is not a simple linear relationship. Previous studies have shown that the current is approximately proportional to the area of cathode electrode until it saturates at a threshold value, which primarily depends on the dimension of the electrolyte reservoir. Second, to ensure that the potential at the counter electrode is sufficiently low to eliminate oxidation of the electrode material, a high surface area ratio between the counter and working electrodes is required. Third, a sufficient reference electrode area is also desirable in order to maintain a stable reference voltage. In addition, the relative position of the three electrodes and the distance between them must also be considered. In most electrochemical systems, the reference electrode should be placed near the working electrode to minimize ohmic losses and to provide a uniform electric field. However, in the electrochemical oxygen sensor, it is better to separate the electrodes as much as possible to eliminate crosstalk between electrodes [58], [59].

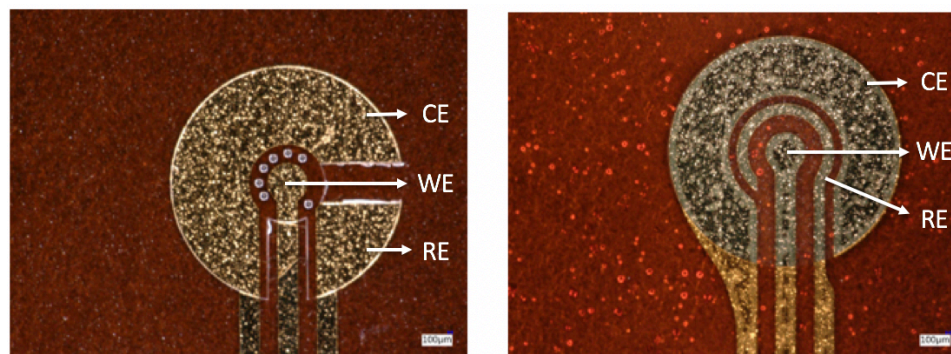
Several designs with different electrode materials, shapes and sizes, as shown in Fig. 3, have been fabricated, tested and compared. The finalized dimension of the oxygen sensor is  $2.5\text{ mm} \times 6\text{ mm} \times 0.3\text{ mm}$ , with a slimmer neck in the middle, as later shown in Fig. 5. Leaving out the connecting wires and solder pad region, the functional region of the sensor is 2.4 mm in diameter. The distance between the cathode surface and the gas permeable membrane is approximately  $6\text{ }\mu\text{m}$ , providing an inner electrolyte system of  $0.027\text{ mm}^3$ . The cathode area for maximum signal saturation is set to approximately  $0.2\text{ mm}^2$ . To minimize crosstalk between the electrodes, the electrode separation distance is  $200\text{ }\mu\text{m}$  in the present work. The surface area ratio of the working, reference, and counter electrodes is approximately 1:1:5, with a working electrode footprint that is  $400\text{ }\mu\text{m}$  in diameter. The connecting wires in the neck region are passivated to eliminate the redox reactions.



(a)



(b)



(c)

Figure 3. Designs with different (a) surface area ratio of the working, reference, and counter electrodes, (b) electrode materials (graphite, Pt and Au) and (c) shapes.

A thin layer (i.e.,  $<20$  nm thickness) of chromium (Cr) is commonly used in microfabrication to improve the adhesion between electron-beam-evaporated gold and a base substrate. Although Cr might improve the adhesion of the device electrodes to the polyimide substrate, a multilayer metallic structure may also introduce complications to the electrochemical system, potentially resulting in abnormal behavior and/or decreased response or stability of the sensor. In such systems, the exposed edge of Cr could lead to a mixed potential on the reference electrode. Also, Cr has a negative redox potential relative to gold, potentially leading to more facile oxidation and subsequent deterioration of the sensor electrode. Finally, dissolved chromium ions might migrate to the cathode; and their reduction at the working electrode could cause an increase in current not reflective of oxygen concentration. Hence, a chromium adhesion layer extending into the sensor/electrolyte region was undesirable in the fabrication of an electrochemical oxygen sensor. However, complete removal of the adhesion layer is problematic. Without such a

layer it was experimentally observed that the working and counter electrodes wrinkle and then physically deform after a very short duration of functionality; further, the absence of an adhesion layer in the pad region rendered subsequent processing more difficult (e.g., delamination of electroplated copper in the contact pads during soldering).

To overcome these difficulties, we developed an electrode fabrication scheme that incorporates a partial adhesion layer and a mesh electrode morphology as shown in Fig. 4. An adhesion layer of chromium is patterned only in the contact pad region, where copper will be electroplated. The mesh structure consists of 20- $\mu\text{m}$ -diameter holes arranged in a radial array. The first thin layer of Au/Cr was deposited onto the polyimide substrate by electron-beam evaporation and lithographically patterned by lift-off, followed by the deposition and patterning of a second, thicker Au layer. To achieve the mesh design, the working and counter electrodes were patterned with an excimer laser, whose micromachining conditions were optimized to ablate the thin film metal without damaging the underlying polymeric substrate. The fabricated electrode is shown in Fig. 5. Fig. 6 shows that the deformation of gold electrodes first appears in areas where mesh density is low, indicating that electrode hole can reduce the deformation and delamination problem of the electrodes. It was also experimentally observed that the electrode mesh morphology improved the lifetime of the electrodes, and the Cr layer greatly improved the adhesion between the metallic contact pad and polyimide substrate and increased tolerance to stress induced in soldering and encapsulation.

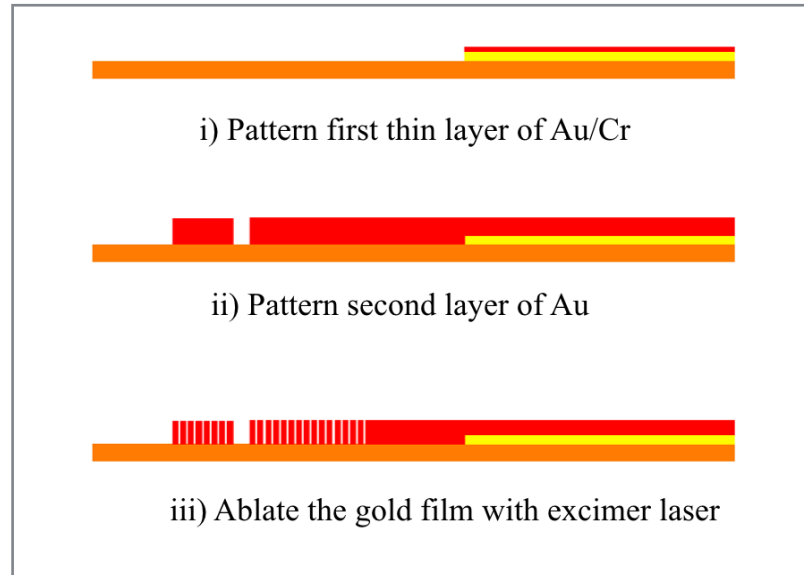


Figure 4. Fabrication scheme of sensor electrode on polyimide substrate

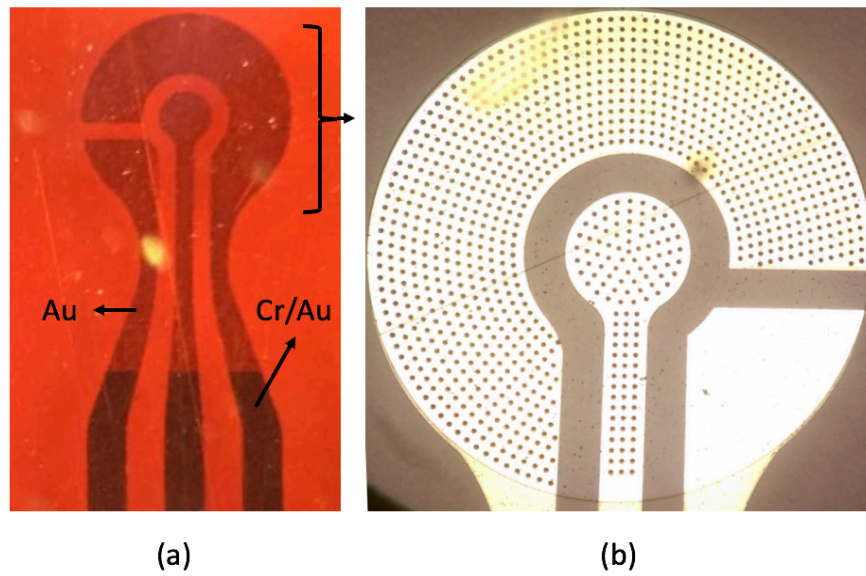


Figure 5. (a) Optical images of sensor electrodes after step (ii) as seen from the backside. The Cr region can be seen through the translucent polyimide; (b) Sensor electrode top view after step (iii).



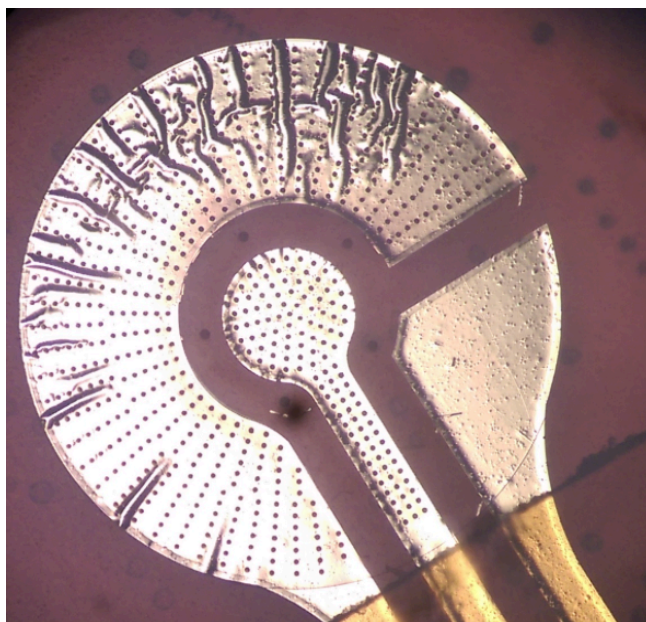


Figure 6. Photomicrograph of a test sensor after electrical operation. The deformation of gold electrodes first appears on the anode, where oxygen is formed. The wrinkles align with the mesh structure in areas where the hole density is low.

#### 2.4.2 Design of electrolyte reservoir

PDMS does not swell in contact with water, indicating that the saturation concentration of water in PDMS is limited. The diffusion coefficient of oxygen and water in PDMS is  $4\text{e-}9 \text{ m}^2/\text{s}$  and  $4\text{e-}10 \text{ m}^2/\text{s}$  [60], respectively. Since water is a critical reactant in the oxygen reduction reaction, and its diffusion coefficient in PDMS is much smaller compared to the diffusion coefficient of oxygen, we need to incorporate water-based electrolyte in between the PDMS membrane and the electrodes such that the oxygen reduction reaction does not depend on water kinetics. The thickness of the inner electrolyte is about  $6\text{-}8 \text{ }\mu\text{m}$ , which facilitates oxygen equilibration with the environment to achieve a fast response.



#### 2.4.3 Design and fabrication of PDMS-based oxygen sensor

A schematic of the oxygen sensor fabrication process incorporating PDMS as the oxygen-permeable membrane is illustrated in Fig. 7. The gold electrodes were patterned onto the polyimide substrate as described above. Five small pores (60  $\mu\text{m}$  in diameter) were formed through the polyimide film in between the working and counter electrodes using an excimer laser to enable subsequent injection of the inner electrolyte prior to activation of the sensor. A 3  $\mu\text{m}$  thick SU-8 layer was then patterned to passivate the gold leads. A photoresist (MicroChem SPR-220 7.0) pattern was used as a mold for the electrodeposition of copper on the contact pads (6  $\mu\text{m}$  thickness). The inner electrolyte chamber was patterned using PVA, a water-soluble polymer with low solubility in organic solvents. The negative image of the chamber was patterned by 9- $\mu\text{m}$ -thick SPR-220 7.0 (MicroChem) and 20- $\mu\text{m}$ -thick PVA (33 wt.%) was spin-cast onto the substrate and dried. The sample was treated by oxygen plasma to remove any PVA coating the edges of the photoresist and, subsequently, sonicated in acetone to dissolve the photoresist and achieve a micropatterned water-soluble mold. PDMS was then spin-coated and cured at 70  $^{\circ}\text{C}$  to form the electrolyte reservoir with a 15  $\mu\text{m}$  thick oxygen permeable membrane. The copper contact pads were exposed by using tape to lift off the PDMS in that area. Finally, sensors were singulated with an excimer laser, soldering was performed for electrical connection, and exposed contacts were encapsulated with a UV curable encapsulant (Dymax 3401). An optical image of a fabricated sensor is shown in Fig. 8.

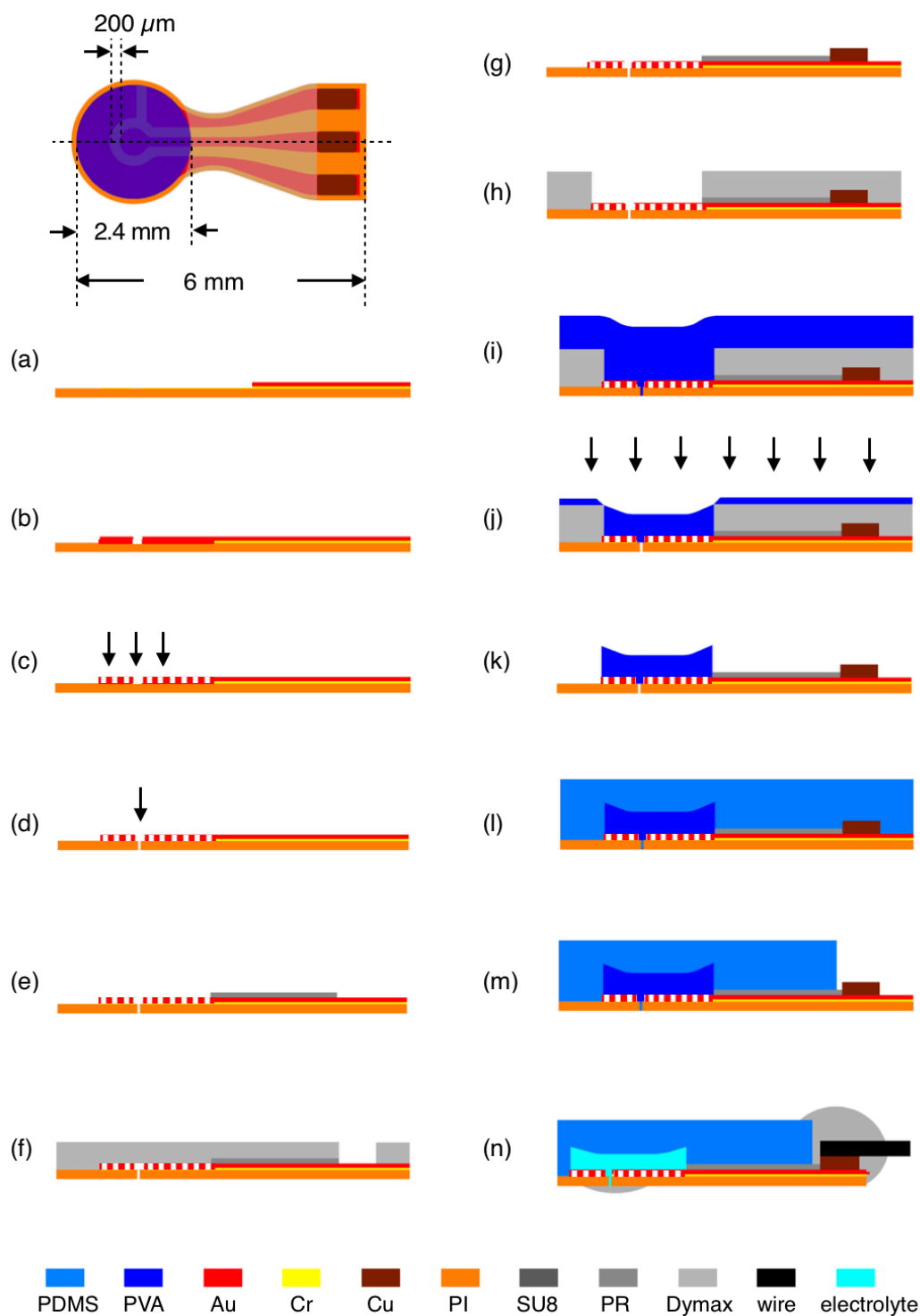


Figure 7. Fabrication process of the oxygen sensor incorporating PDMS as the oxygen-permeable membrane.

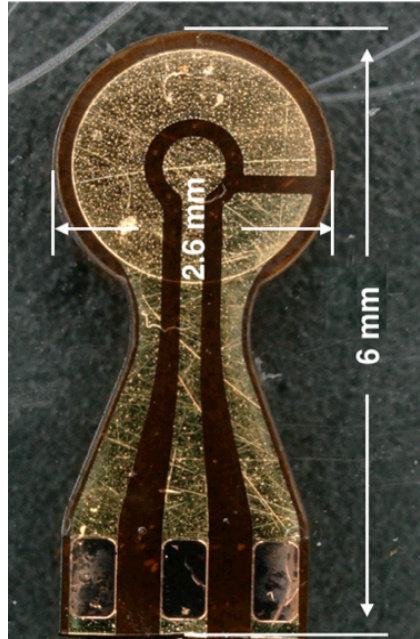


Figure 8. Optical image of the fabricated sensor.

#### 2.4.4 Design and fabrication of FEP-based oxygen sensor

The fabrication process of electrolyte reservoir featuring FEP membrane is shown in Fig. 9. The steps through the patterning of electrodes and electrolyte reservoir are the same as demonstrated in Fig. 7, from step (a) to step (e). After the chamber is patterned with a sacrificial PVA structure, a 12  $\mu\text{m}$  thick FEP membrane was laminated onto the top and cut with excimer laser to the size of the foot print of the electrolyte chamber. Subsequently, 10  $\mu\text{m}$  thick Parylene was deposited to seal the FEP film to the substrate. An excimer laser was again used to etch down Parylene to expose the FEP film and copper pad area, and the micromachining conditions were optimized to ablate the Parylene film without damaging the underlying oxygen-permeable membrane.

Specifically, the fluence used to ablate Parylene is in the range 0.4-0.6 J/cm<sup>2</sup> to maximize the removal rate of Parylene without impacting the substrate [61]. Sensors were subsequently cut, wired and encapsulated as discussed in Fig. 7.

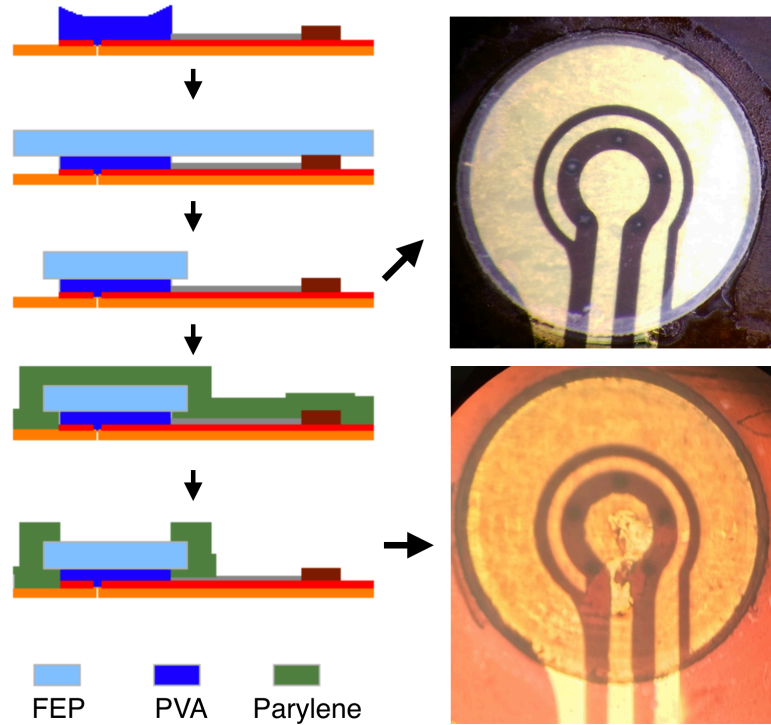


Figure 9. The fabrication process of electrolyte reservoir featuring FEP membrane.

The inner electrolyte comprises a 0.1 M NaCl solution, chosen since it is the major ionic content of many physiological environments. In order to fill the chamber with electrolyte, the sample was immersed in 0.1 M NaCl for 12 hours to allow the electrolyte to infiltrate through the laser-ablated pores on the back side of the sensor and to dissolve the remaining PVA. It is assumed that the remaining PVA is diluted during this process to a negligible concentration. The pores in the sensor substrate are sealed from the backside,

as shown in Fig. 10. The sensor was placed with the top side facing downward on a surface wetted with 0.1 M NaCl solution to prevent evaporation of inner electrolyte, and a thin layer of Dymax 3401 was applied to the laser-ablated pores on the back side. UV light was applied to cure the Dymax 3401 and therefore seal the electrolyte reservoir. The membrane is 12  $\mu\text{m}$  in thickness and separated from the electrodes by a 6- $\mu\text{m}$ -thick inner electrolyte cell containing a 0.1 M NaCl solution. To validate that the electrolyte has been introduced into the chamber, a voltage of 2V was applied between two of the electrodes for water electrolysis. Decomposition of water forms a large bubble, as shown in Fig. 10(d), demonstrating that water has successfully infiltrated the electrolyte chamber and the inlets were subsequently successfully sealed.

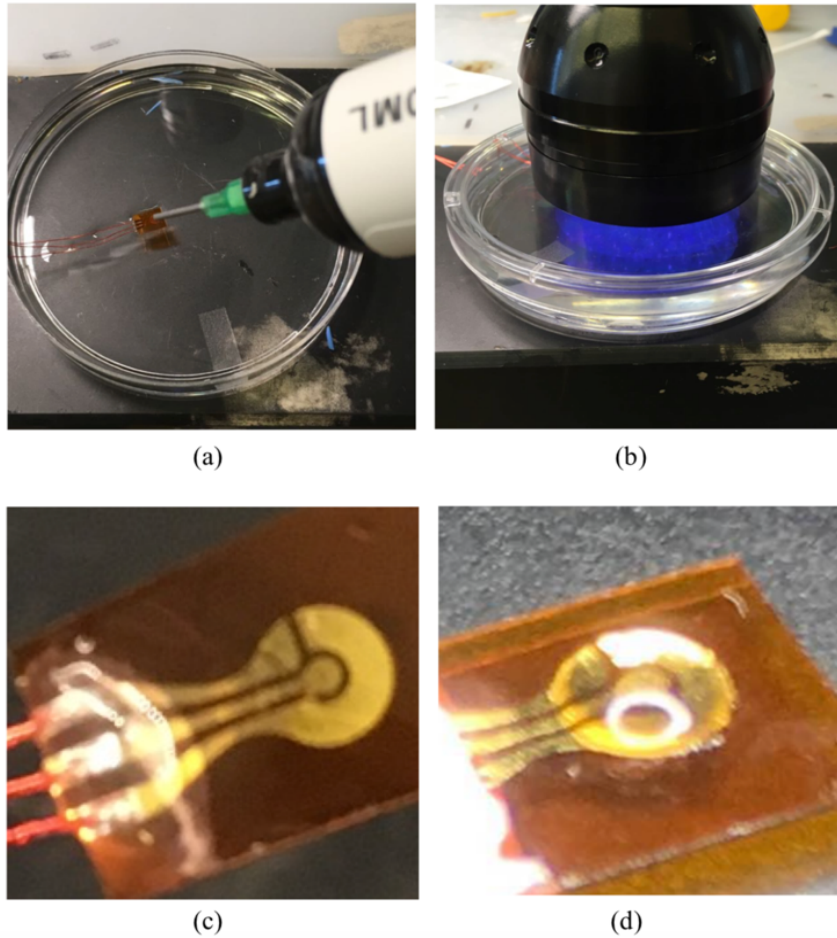


Figure 10. Process of sealing the holes in the sensor substrate from the backside using Dymax 3401. (a) Apply a thin layer of Dymax 3401 to the laser-ablated holes on the back side. (b) UV light was applied to cure Dymax 3401 and therefore seal the electrolyte reservoir. (c) Sensor filled with electrolyte and sealed from the back. (d) Water electrolysis decomposes water to form a large bubble.

## 2.4 Customized potentiostat

A customized potentiostat is developed to interface with the sensor and provide wireless data transmission capability. As shown in Fig. 11, the analog circuitry contains a digital-to-analog converter (DAC) and two operational amplifiers (op-amps) with negative feedback for generating voltage waveforms and quantifying current at sufficient precision.

The objective of the circuit is to provide a regulated voltage between the WE and the RE and to deliver an output voltage proportional to the sensor output current (produced by any electrochemical reactions on the electrodes). The voltage between the WE and RE are controlled and maintained by the DAC and op-amps, and can be modulated as a function of time in a pattern dependent on the type of required experiment, e.g., in this case, a linear change for linear LSV. The op-amp controlling the voltage of the WE also functions as a trans impedance amplifier that converts the current from the inverting input into a voltage, which can be calculated by:

$$V_{\text{out}} = V_{\text{W}} - I \cdot R \quad (5)$$

where  $V_{\text{out}}$  represents the output voltage of the transimpedance amplifier.  $V_{\text{W}}$ ,  $I$ , and  $R$  denote the WE voltage, output current of the sensor, and feedback resistance of the trans impedance amplifier, respectively. When a negative potential is applied between WE and RE, the oxygen reduction occurs on the anode surface, and positive charges are generated at the sensor anode. Current flowing out of the WE feeds into the trans impedance amplifier and, in this manner, the output voltage is proportional to the charges generated in the oxygen reduction reaction. The CE is connected to the output of an op-amp, which will source adequate current to balance the current required by the WE. We employed TI LMV342IDGKR op-amps in the customized potentiostat because they feature very low offset voltage and input bias current and are low power. Specifically, these amplifiers have an input bias current of 1pA and an input bias voltage of 0.25 mV, which render them capable of regulating electrode voltage with millivolt precision and measuring electrode current with nanoamp precision. The output voltage of the transimpedance

amplifier is fed into a MSP430 (TI CC430), which performs analog-to-digital (ADC) conversion, data storage and wireless transmission to a remote-control board.

The microcontroller is used to program the DAC output and read ADC input to perform the LSV technique. The desired range of LSV for our application is from 0 V to -1.5 V, which suggests that  $V_W - V_R$  need to support a lower limit of -1.5V and upper limit of 0 V. In addition, since the output voltage of the trans impedance amplifier is depicted by equation (5), a constant  $V_W$  makes it easier for the microcontroller to acquire data with the ADC. Therefore, we set  $V_W$  to a DC offset of 1.2V, and  $V_R$  is programed to vary from 1.2V to 2.7V, thus giving a LSV scan range of 0 V to -1.5V. The smallest potential step required for our application is 5mV, therefore a 12-bit DAC with a 2.7 V reference, which provides a theoretical resolution of 0.7 mV, is sufficient. Sensitivity of the system is determined by 1) resolution of the ADC, 2) reference voltage provided to the ADC, and 3) feedback resistance of the trans impedance amplifier. The reduction reaction on the anode produces a positive current flowing into the trans impedance amplifier, resulting in an output voltage between 0 and  $V_W$ . Therefore, a 1.2V reference, equal to the value of  $V_W$ , is chosen for the ADC to provide higher resolution. In addition, because the maximum reduction current under saturated oxygen state is less than 2  $\mu$ A, a feedback resistance of 600 kohms would provide sufficient current resolution for the desired measurement range. For a 12-bit ADC with 1.2V reference, the resolution is 2 nA in principle. Increasing the feedback resistance would further improve the resolution, while compromising the upper limit of measurable current. The practical minimum



current we can resolve is slightly higher than the theoretical value, due to the nonlinearity of DACs, mostly within a few least-significant bits, and the electronic noise in the system.

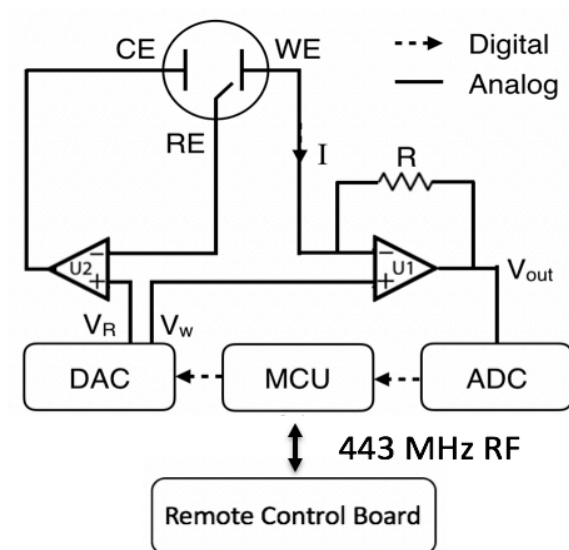
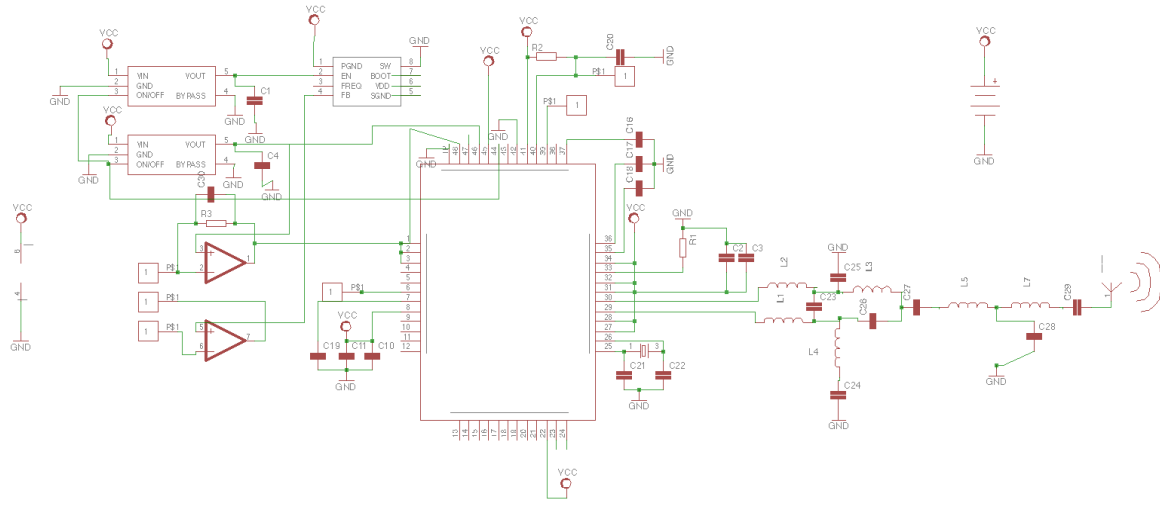


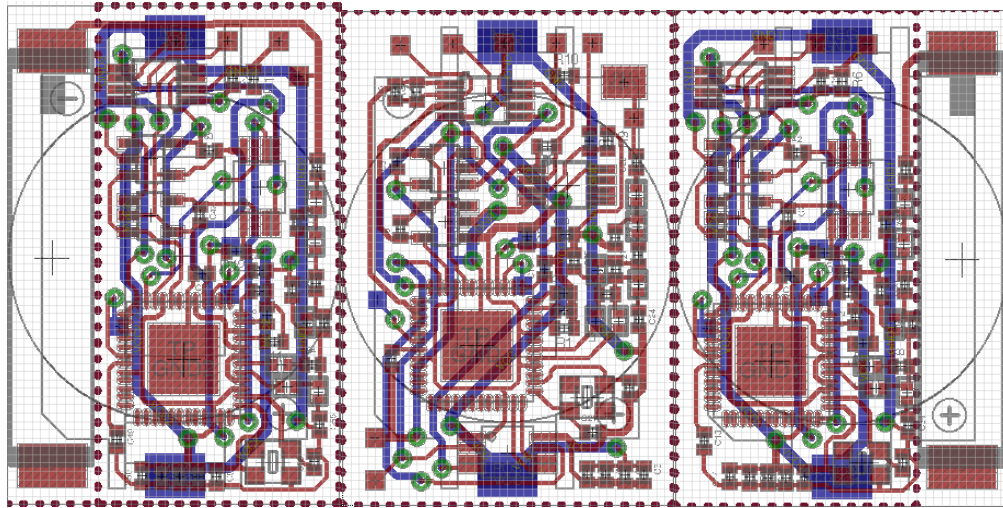
Figure 11. Circuit schematic of the customized potentiostat connected to a three-electrode oxygen sensor.

## 2.5 Wireless transmission

A commercial quarter wave antenna (433 MHz) and matching network were included to enhance the transmission intensity. Fig. 12 shows the schematic and layout of the PCB transmission circuit for the oxygen sensor. The transmission circuit was designed to maximize power transfer and the antenna supports radio transmission/receiving. Peripheral circuits were incorporated for decoupling and stabilization.



(a)



(b)

Figure 12. (a) Schematic and (b) layout for the potentiostat and wireless transmission board.

Fig. 13 shows the process flow of the customized potentiostat controlled by a remote board. The program is optimized to achieve extended battery life by incorporating the WOR and standby modes. The current consumption of radio module in active mode is approximately 15 mA, while in WOR mode with a duty cycle of 15%, the average current consumption is reduced to 2 mA. The radio output power of the baseboard and

satellite board are set to 0 dBm. In this configuration, approximately 85% of the energy wasted during idle listening is eliminated. In standby mode, only the Real-Time Clock (RTC) module is active to keep track of the time, and the power consumption is approximately 2  $\mu$ A. The customized potentiostat is controlled to either perform LSV measurement or remain on standby to conserve power based on the command it wirelessly receives. The process flow can be summarized as three loops: 1) The potentiostat begins in the WOR mode and, after receiving a start command, advances to loop 3 until it receives a ‘stop’ command, upon which the potentiostat resumes the WOR mode; 2) The platform starts from the WOR mode, and after receiving a “sleep” command, sets the timer in the RTC module and jumps into standby mode. After the timer is cleared, the platform resumes the WOR mode. The “sleep” command is a simple packet structure with two sections - one to identify the type of command, and another to store the number of hours for the timer; 3) The potentiostat applies a voltage to the sensor, reads the sensor output, and sends data to the remote board. This process is repeated until a ‘stop’ command is received. LSV testing is performed by incrementing varying the applied voltage in each cycle at 1Hz frequency, and the total time for transmitting data and listening is reduced to 40% to save power. We assume that the microcontroller stays in WOR mode for 3 minutes before each test, and since one LSV measurement takes no more than 4 minutes at a scan rate of 5 mV/s, the maximum power consumption for each test is 0.5 mAh. In standby mode, the power consumption of one day is 0.05 mAh. Therefore, if we take measurements at a frequency of one points per day, the customized potentiostat can last on the order of months with a commercial CR2032 battery.

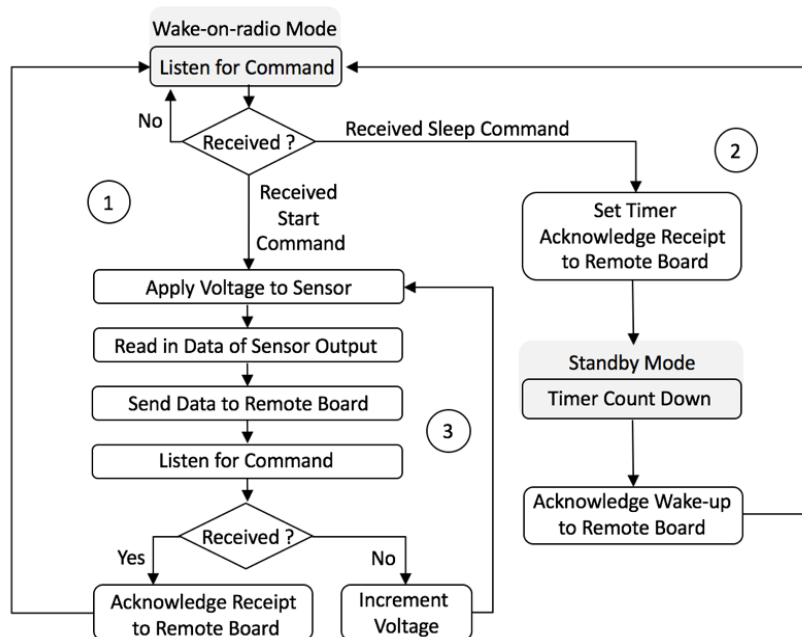


Figure 13. The process flow of the customized potentiostat controlled by a remote board.

## 2.6 Benchtop test results

### 2.6.1 Response tests

Benchtop electrochemical testing of the electrochemical sensor was performed in a 0.1 M NaCl solution, where the oxygen concentration was tuned to the physiological range (i.e., 0 – 8.6mg/L at 25 °C and sea level) and calibrated to a commercial O<sub>2</sub> probe (Microx TX3, PreSens). Various O<sub>2</sub> concentrations were achieved in the solution by the addition of sodium sulfite (Na<sub>2</sub>SO<sub>3</sub>) in quantities sufficient to consume the excess oxygen due to a chemical reaction of oxygen with Na<sub>2</sub>SO<sub>3</sub>. Specifically, sulfite reacts with and consumes dissolved oxygen to produce sulfate, thus decreasing oxygen concentration in aqueous solutions. Upon consumption of the sulfite, over time and in ambient conditions oxygen

is naturally reintroduced into the solution; this gradual increase in oxygen concentration is monitored both by the commercial oxygen probe and by this electrochemical sensor and compared. Performance of the device was evaluated by LSV using a commercial potentiostat (Reference 600, Gamry). The bias potential between the working and reference electrodes was swept at a rate of  $-5$  mV/s until the sensor reached the diffusion-limited regime. Fig. 14 shows the testing result of an oxygen sensor with a PDMS membrane thickness of  $12\text{ }\mu\text{m}$ . The limiting current was identified as the intersection of the reaction-limited region and diffusion-limited region of the I-V curve (i.e., the circular markers in Fig. 14(a)). The corresponding calibration curve for the fabricated electrochemical oxygen sensor is shown in Fig. 14(b), where the current measurement is cross-referenced to the oxygen measurement from the commercial oxygen probe. The corresponding current of the reaction-limited region moves towards more negative potentials as the oxygen concentration increases. That is because the limiting current is proportional to the concentration and hence the transition between the kinetic and the diffusion limited regions occurs at an increased bias with increasing oxygen concentration. The fabricated sensor demonstrated an oxygen response of approximately  $-14\text{ nA/atm.}\%$  and excellent linearity; linear regression yielded a correlation coefficient of 0.9906.

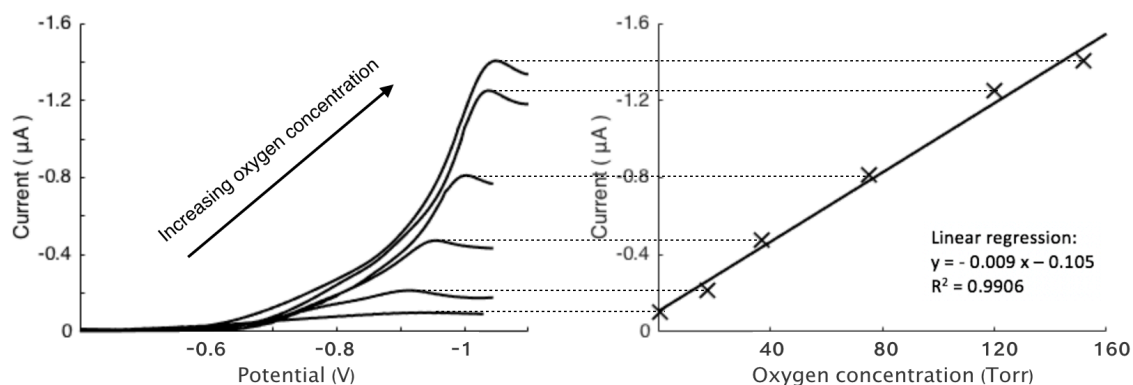


Figure 14. Electrical response of the fabricated electrochemical sensor. (a) Linear sweep voltammogram for a sensor tested within oxygen concentrations of 0.5%, 11%, 23%, 47%, 75%, 95% with respect to atmospheric oxygen. (b) The diffusion-limited-current/calibrated-O<sub>2</sub>-concentration relationship. The sensor demonstrated linearity across a range of physiologically relevant concentrations.

Fig. 15 shows the LSV curves of the same sensor tested under saturated oxygen concentration. The plateau currents are consistent while the corresponding transition voltage shifts from -0.7 V to -0.85 V. As discussed earlier, while the durability of the gold reference electrode is superior to a simple thin-film Ag/AgCl pair, the potential exhibits more fluctuations—a shortcoming that can be overcome by using LSV to find the limiting current region. Specifically, the gold reference potential is drifting during measurement, which leads to a changing potential difference between working electrode and reference electrode. Although the appearance of redox peak is shifting in the I-V curve, the absolute reduction potential might not be altered as greatly. Therefore, the plateau current still reflects the oxygen tension under test.

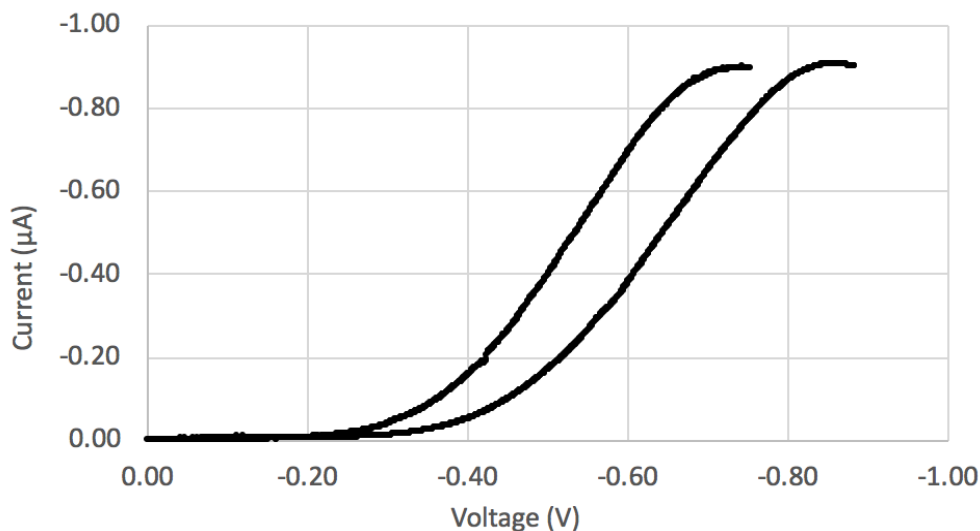


Figure 15. LSV curves of the same sensor tested under saturated oxygen concentration.

A bend test was performed to evaluate the resistance to mechanical failure of the sensor. Two plates were used to anchor the contact pad region and functional region, respectively, and the middle part of the sensor is bent to a specific angle by moving one plate to form an inside radius. The sensitivity of the sensor remained unchanged at a bending angle of 30 degrees in the middle part, demonstrating good flexibility for applications involving mechanical loading.

Sensors with different oxygen permeable membranes are compared in Fig. 16. The responses of the PDMS based sensors fabricated following the steps described in Fig. 7 lie in a range from -9 nA/atm.% to -14 nA/atm.%. This variation was suspected to be introduced by the uniformity and consistency problem in the oxygen plasma treatment of the PVA sacrificial structure, which might lead to a variation in the size of the electrolyte reservoir. FEP based sensors have response between -1.8 nA/atm.% to -2.2 nA/atm.%, which was expected since FEP has lower oxygen permeability. Due to the variation in

response, each sensor should be calibrated after infiltration of inner electrolyte. Sensors can be stored in solution for months prior to usage, since the sensor has no consumable parts, and the unbiased interior components show excellent stability with time.

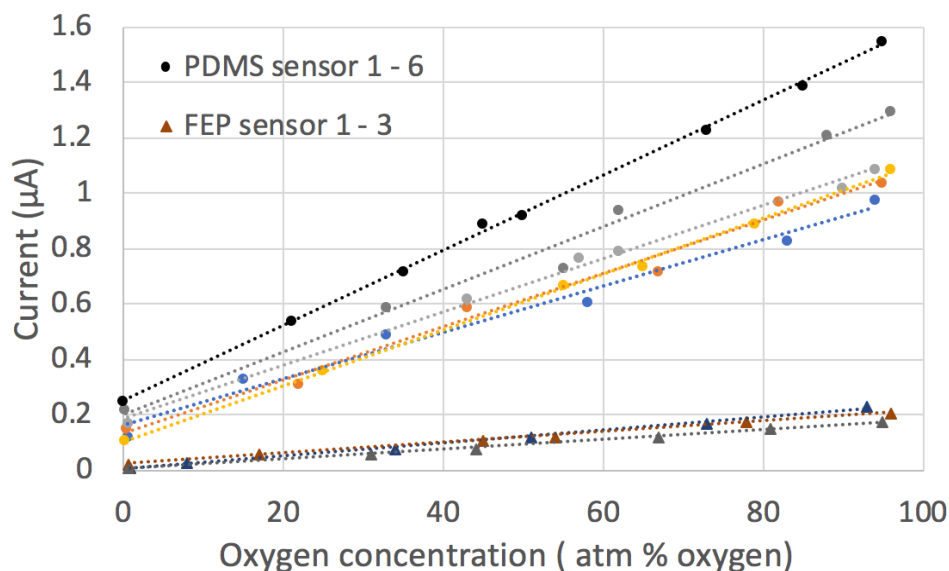


Figure 16. Response characterization of the fabricated sensor with different oxygen permeable membranes.

Biological studies are usually conducted at body temperature (37 °C), while environmental monitoring tests are mostly taken at room temperature (20 °C). To determine the sensor performance at different temperature range, the sensor was characterized in 0.1 M NaCl solution at room temperature and body temperature, respectively. Fig. 17 shows the calibration curve of a sensor in 0.1 M NaCl at 20 °C and 37 °C. The sensor demonstrated an oxygen sensitivity of approximately -14.5 nA/atm.% at 20 °C, and approximately -17.5 nA/atm.% at 37 °C. This indicates that the sensitivity of the sensor changes over temperature at a rate of approximately 0.18 nA/ atm.% °C.



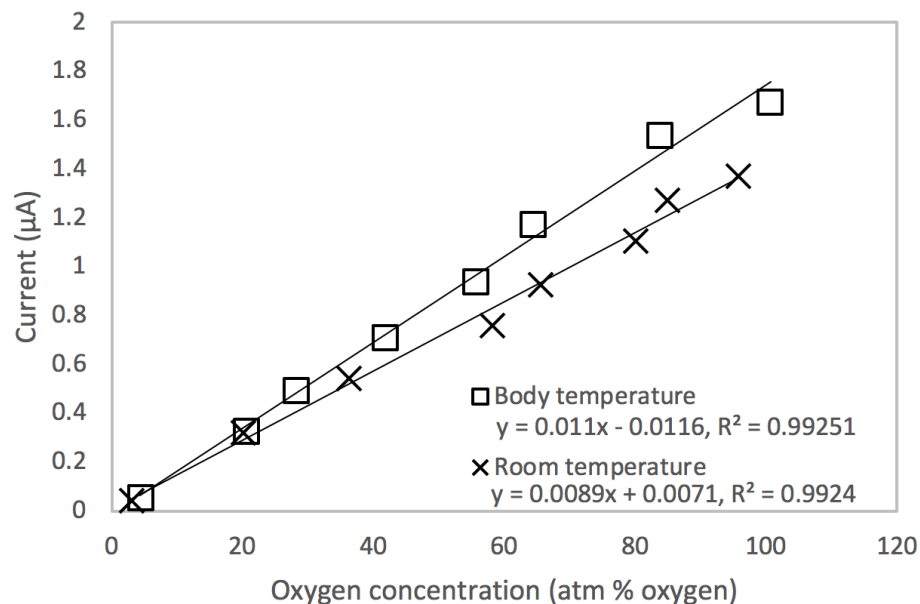
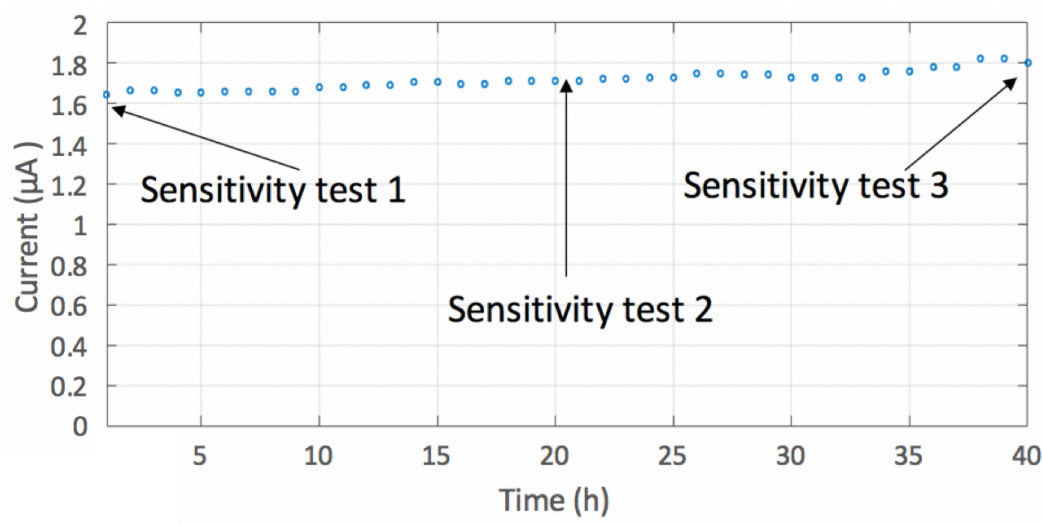


Figure 17. Response characterization of the fabricated sensor at 20 °C and 37 °C.

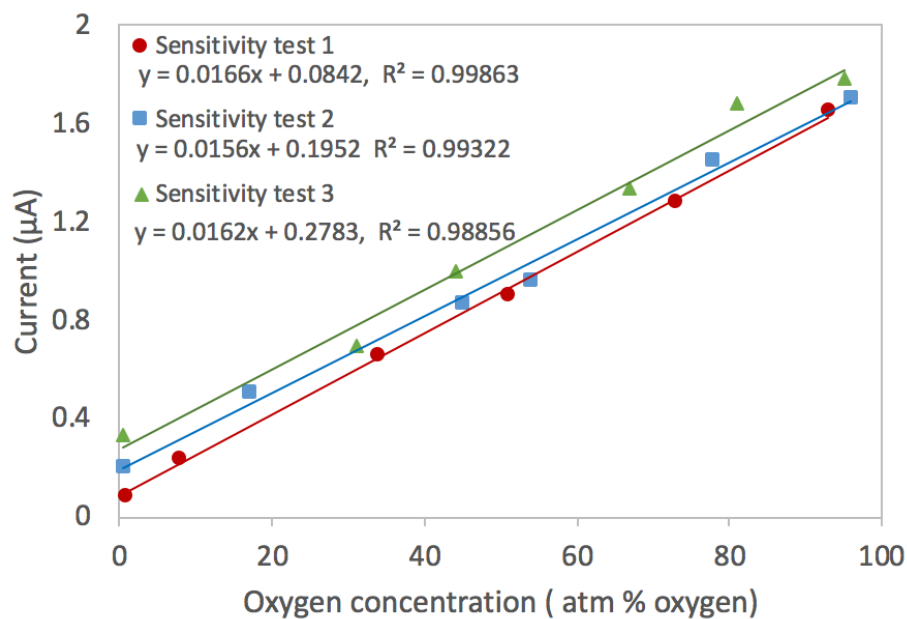
### 2.6.2 Stability Tests

Oxygen sensors with a 12 μm thick PDMS membrane were utilized to analyze the stability performance. The test medium was a 0.1 M NaCl solution saturated with oxygen. LSV tests were performed periodically every hour at room temperature for a total of approximately two days, and three sets of response tests were performed (i.e., at the beginning, middle and end of the stability test). As shown in Fig. 18, the output current remained stable over the duration of 58 tests including the response tests. The sensor demonstrated similar response at the beginning, middle and end of the stability test. The same tests were performed at body temperature for a total of 80 hours, and the response change over time was also evaluated. The solution under test was incubated in heated water and maintained at 37 °C. As shown in Fig. 19, the fluctuation in current at body

temperature is slightly larger than at room temperature. This might be caused by slight temperature fluctuation of the water bath. The response test at both body temperature and room temperature showed relatively consistent slope, while the intercept increased over time. This indicates that the current shift during the tests is attributed to the increase of residual current.

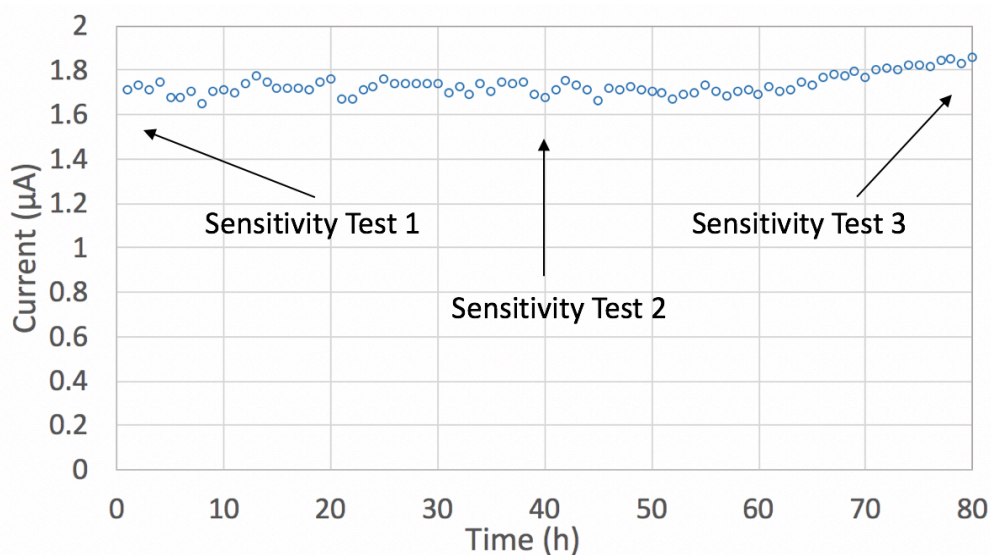


(a)

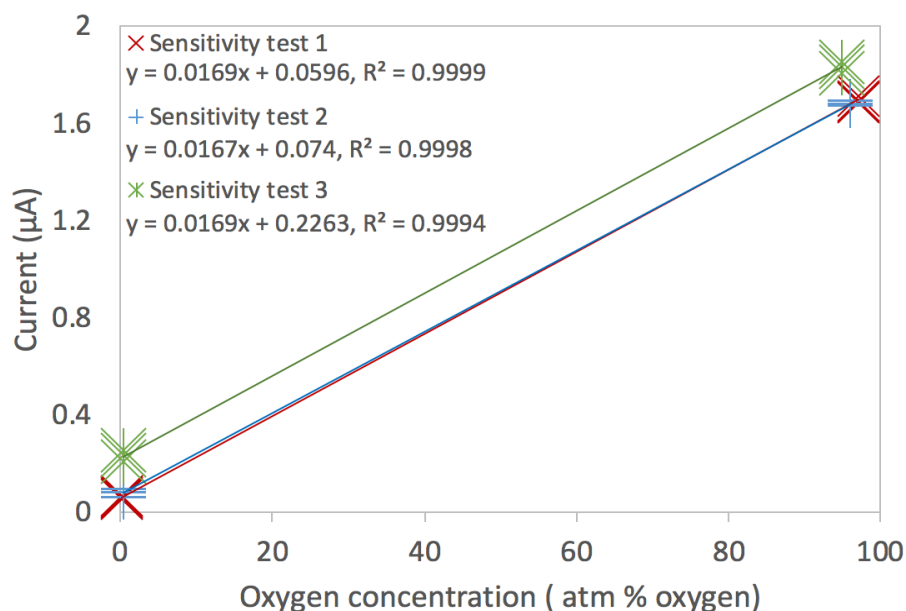


(b)

Figure 18. (a) The stability results of the fabricated electrochemical oxygen sensor at room temperature by measuring the diffusion-limited reduction currents at a full-oxygen state 40 times sequentially. (b) The sensitivity results of 3 sets of tests.



(a)



(b)

Figure 19. (a) The stability results of the fabricated electrochemical oxygen sensor at 37 °C by measuring the diffusion-limited reduction currents at a full-oxygen state 80 times sequentially. (b) The sensitivity results of 3 sets of tests.

### 2.6.3 Lifetime Tests

0.1 M NaCl solution was used to evaluate the lifetime of the sensor at room temperature. Fig. 20 shows the life time characterization of the sensor at 20 °C obtained by cross-referencing to a commercial oxygen sensor. Measurements were performed periodically by LSV every hour until device failure. The inset shows the diffusion-limited reduction currents of the first 50 measurements cross referenced to the commercial sensor. The overall linearity of the 50 tests were obtained with a correlation coefficient of 0.99. An increasing current drift was observed after 140 tests. It is speculated that the deterioration in performance of the sensor is attributed to slow physical degradation of the metal film

when currents flow through the electrodes. Fig. 21 shows testing results at full-state oxygen from custom sensor over 2 weeks, and the insets show simple sensitivity results at day 1 and day 14, respectively. The measured currents lay within  $1.56 \pm 0.06 \mu\text{A}$  with a standard deviation of 0.04 except for day 9 and day 10, which have a high probability of being outliers, based on student's t-distribution. The large current change in day 9 and day 10 is suspected to originate from ambient environmental change (e.g. temperature, convection), as the sensor sensitivity is not largely altered in 14 days.

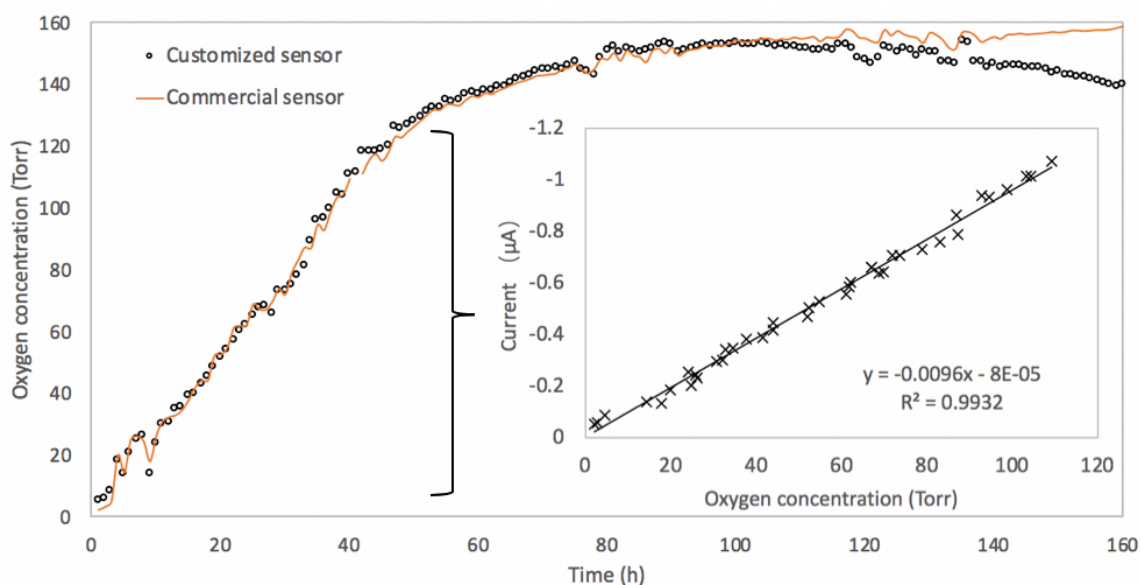


Figure 20. Life time characterization of the fabricated oxygen sensor at room temperature. Data obtained from customized sensor (black circles) are cross-referenced to a commercial oxygen sensor (orange line).

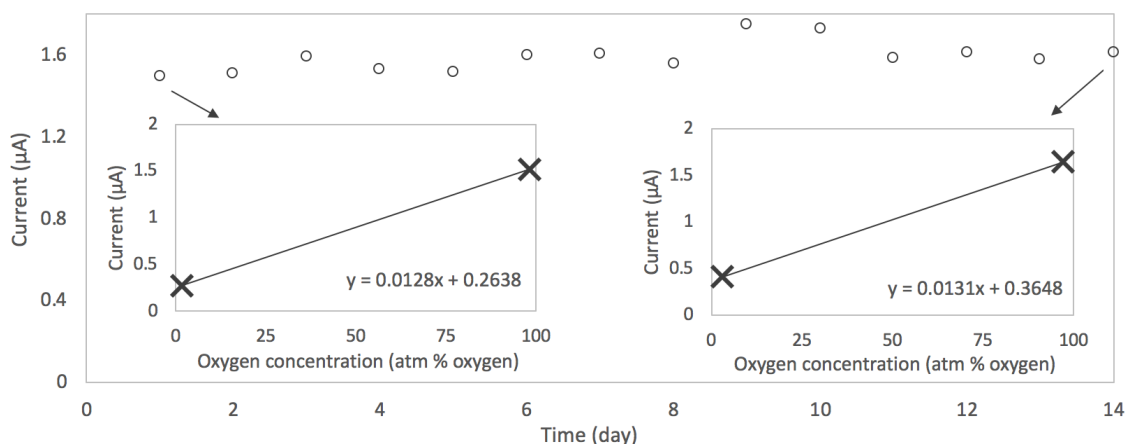


Figure 21. Life time characterization of the fabricated oxygen sensor at room temperature by measuring the diffusion-limited reduction currents at a full-oxygen state over 2 weeks. The insets showed simple test results of the sensitivity in day 1 and day 14. Data obtained from customized sensor at oxygen-depleted state and full-oxygen state is cross-referenced to a commercial oxygen probe.

As we discussed earlier, sensors can be stored in solution for months without alteration in sensitivity, since the sensor has no consumable parts, and the unbiased interior components have excellent stability with time. The sensors can potentially support testing for 140 days if one test is performed each day. In many biomedical applications, oxygen concentration is expected to change slowly, thus, sparse time point measurements may be satisfactory for biological research or for clinical use. The results suggested that the oxygen sensor is sufficient for monitoring oxygen tension in situ over semi chronic time periods (e.g., weeks to months) at physiological oxygen magnitudes.

#### 2.6.4 Customized potentiostat platform

An optical image of the wirelessly controlled, customized potentiostat is shown in Fig. 22. The dimension of the printed circuit board (PCB) is 30 mm  $\times$  20 mm  $\times$  8mm. A CR 2032 battery holder was soldered on the backside of the board for onboard power supply.

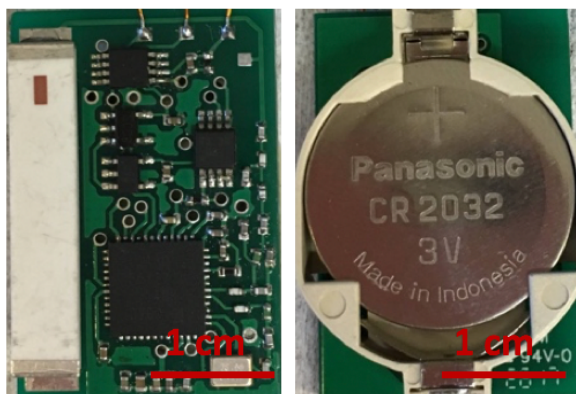


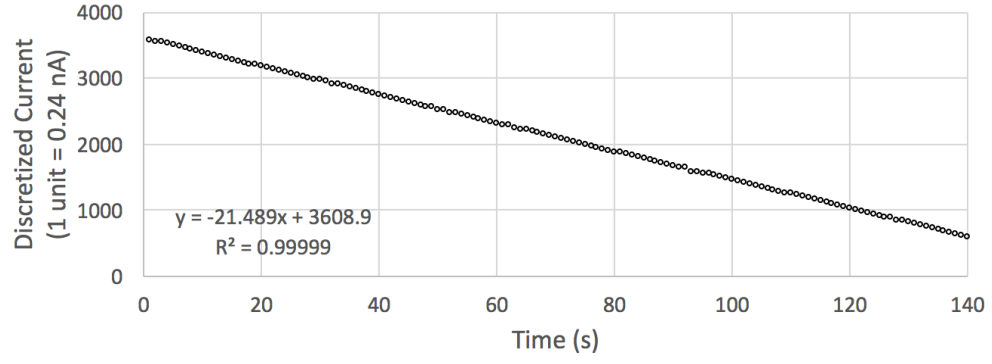
Figure 22. Front and back side of the wirelessly-controlled potentiostat circuit board. The overall dimension of the PCB board is 2 cm  $\times$  3 cm  $\times$  8 mm.

To quantify the noise of the customized potentiostat platform, LSV measurements were performed over a 1 M $\Omega$  resistor to reflect typical measurement current range. The feedback resistance of the trans-impedance amplifier, in this case, was 1.2 M $\Omega$ . A two-electrode setup was incorporated: one end of the resistor is connected to WE and the other is connected to RE and CE. The scan rate of the LSV measurement is -5 mV/s. Fig. 23(a) shows the raw data transmitted from the microcontroller. With a feedback resistance of 1.2 M $\Omega$  and ADC voltage reference of 1.2V, the full-scale output corresponds to 1  $\mu$ A. Since the output from the 12-bit ADC spans 4096 units, the resolution of the potentiostat is 0.24 nA. Fig. 23(b) demonstrates the current noise obtained by subtracting the expected value from the actual readout of the microcontroller.

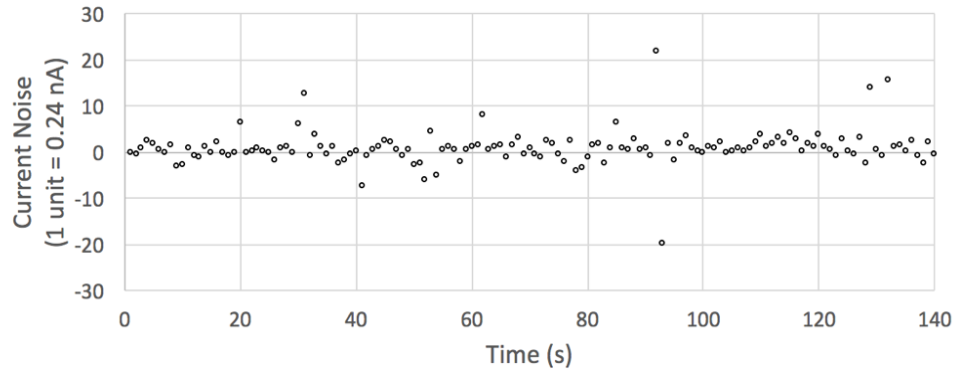
The standard deviation of discrete current noise is approximately 1.2 nA, which is sufficient for our application. In addition, random noise is easily filtered because only the average plateau current is of interest in oxygen detection using linear sweep voltammetry.

To evaluate the limiting factor of the potentiostat performance, current noise of the circuit was quantified at different gains of the trans-impedance amplifier (set by the feedback resistance value). The noise value was taken as the standard deviation of the acquired data. A typical laboratory setting was used to perform the measurements, without special precautions to reduce environmental noise (e.g., enclosure in a Faraday cage). Fig. 23(c) shows the measured standard deviations plotted as a function of feedback resistance, and the theoretical accuracy of the 12-bit ADC. The smallest current that can be measured is limited by either the accuracy of ADC or the analog noise of the circuit and environment. If the measurement is ADC-precision limited, the measurement accuracy should improve while the current is amplified before being fed into ADC. On the other hand, if the measurement is analog-noise limited, the measurement accuracy should decrease while the noise is also amplified by the trans-impedance amplifier. As shown, the measured noise decreases as the trans-impedance amplifier gain increases, indicating that this 12-bit ADC truncates data above the analog noise of the circuit. Further improvement can be made with a higher resolution ADC.

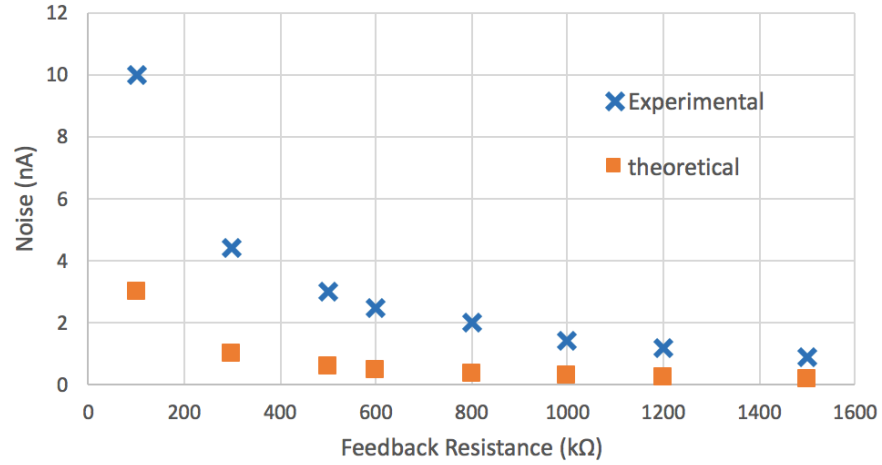




(a)



(b)



(c)

Figure 23. (a) Raw data of LSV testing over a 1 MΩ resistor using the customized potentiostat platform with a 1.2 MΩ feedback resistance and (b) Corresponding current noise. (c) Noise standard deviations as a function of feedback resistance.

### 2.6.5 End-to-end Testing of oxygen sensing system

The Clark-type oxygen sensor and customized potentiostat is successfully integrated for deployment of the sensing platform in field use. To validate the system integration of the sensor with the customized potentiostat, end to end calibration to the commercial oxygen sensor was first performed. The test is performed in a 0.1M NaCl solution with tunable oxygen concentrations, similar to the protocol previously described for sensor characterization. The oxygen concentration was tuned to the physiological range (i.e. 0 – 160 Torr). Linear sweep voltammetry was recorded starting from 0 V at a scan rate of -25 mV/s. Raw data of the I-V curve was send to the battery-powered personal computer and plotted using GUI in real time. When the output current of the LSV measurement reaches a plateau, the experiment is manually terminated by sending commands using the GUI application. The result was later directly cross-referenced to the oxygen measurement from the commercial probe.

Fig. 24 shows the results of the end-to-end testing of the oxygen sensor connected to the customized potentiostat. The I-V curve demonstrates a clear plateau for extracting the corresponding limiting reduction current at each oxygen concentration. The result is directly cross-referenced to the oxygen measurement from the commercial probe. This oxygen sensing system demonstrated an oxygen sensitivity of approximately 13 nA/atm.% and excellent linearity, confirming that the customized potentiostat can maintain accuracy sufficient for *in vivo* applications.

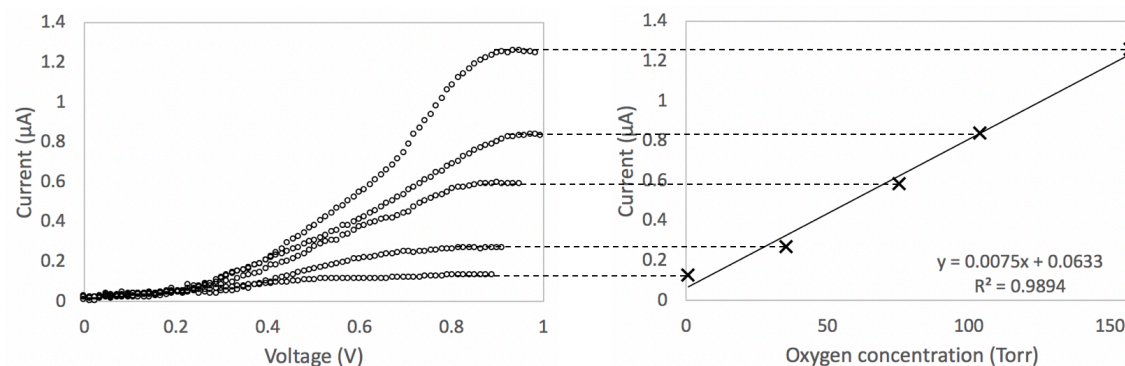


Figure 24. End to end testing and calibration of the oxygen sensing system. (a) LSV data obtained from customized potentiostat. (b) Corresponding current measured from the full system calibrated to a commercial oxygen sensor.

## 2.7 Summary

Microfabricated Clark-type electrochemical oxygen sensors with integral electrochemical chambers were designed and fabricated, and their performance was examined. Features of the presented design include a freestanding and miniature structure. Two oxygen-permeable membrane materials were explored, and their responses were compared. In order to maintain a stable reference potential during a long period of shelf and functional time, an inert gold electrode without adhesion layer was fabricated, and the remaining, slight drift in reference potential was overcome by using LSV for characterization. The customized potentiostat platform was also designed, populated and tested for noise levels. The circuitry showed sufficient accuracy for *in vivo* applications. This design features fabrication of reliable and durable electrodes and easy integration of a miniaturized reservoir, thus providing a simplified strategy to fabricate freestanding, miniaturized oxygen sensors with a long shelf life and desirable functional life span.

## CHAPTER 3 *IN VIVO* APPLICATION OF THE OXYGEN SENSOR

### 3.1 Background and motivation

Oxygen-based cues are important assessments for a wide range of *in vivo* biological effects, ranging from mitochondrial diseases to tissue engineering/regenerative medicine [8], [62], [63]. However, this was largely unexplored until T. K. Hunt recognized that accurate tissue oxygen measurements are required in defining the role of oxygen in wound healing in the early 1960s [64], [65]. Hunt used polarographic methods in his initial studies, which contributed to the development of more compact oxygen sensors [66]. Clark was among those who improved oxygen-measurement technology to the point that all functional components can be integrated to a compact volume, which is more practical for animal studies [67]. Specifically, a major advance was sealing the electrodes, along with a small volume of electrolyte solution, behind a polyethylene membrane. However, the large size of the sensor still limited its use to fluid and subcutaneous applications, until it was miniaturized by Silver [68]. Later technological advancements further improved the feasibility and efficiency of Clark-type sensors for short-term *in vivo* applications, as discussed in chapter 2. For instance, oxygen sensors consisting of a platinum cathode and silver anode were used to measure intraoperative intestinal oxygen tension and predict the occurrence of an anastomotic leak [69]. Brighton and Krebs also measured oxygen tension in a rabbit fibular fracture using a miniaturized Clark-type oxygen sensor inserted at each time point [10]. They noted marked differences and temporal trends of the oxygen tension in the hematoma, woven bone, and intact diaphyseal bone.

Optical sensing based on the quenching of luminescence is a relatively new technology for measuring oxygen tension [70]. Over the past decades, optical sensors have experienced a fast growth and are in the process of replacing the Clark-type sensors in many fields since 1) oxygen is not consumed during measurements using optical sensors and 2) the optical sensors have accuracies similar to those of the Clark sensors but are typically easier to maintain as they are less prone to decreasing accuracy over time caused by calibration drift [71]. As a result of their commercial availability, hundreds of applications in areas as diversified as blood gas and clinical analysis, monitoring of oxygen tension in skin and toxicity testing have been conducted in the past 20 years [71], [72].

Although the commercialized oxygen sensors have been widely used in biomedical applications, substantial work remains to be done, both in advancing the existing oxygen sensing technologies and in further understanding oxygen-based cue in biological processes. The existing commercial oxygen sensing devices, either optical or electrochemical, are all handheld systems and only applicable to short-term intraoperative use; they cannot be left *in situ* as a means of real-time, continuous, postoperative monitoring. The development of a miniaturized implantable oxygen sensing system could provide an additional means to enhance the preclinical development for a number of relevant diseases. In addition, for clinical practice where oxygen delivery is an important factor, for example in bone fracture, traumatic brain injury and wound healing, the development of implantable, post-surgery oxygen sensing techniques has great potential in transforming clinical trials where repeatable, objective outcome measures are lacking.

A number of factors that should be taken into consideration for implantable applications.

The ideal oxygen sensing system would have the following attributes:

- 1, High sensitivity;
- 2, Easy calibration;
- 3, Motion and pH changes do not induce artifacts;
- 4, No oxygen consumption during measurement;
- 5, Long-term measurement possible;
- 6, Small footprint and wireless data transmission capability.

The currently preferred method to measure oxygen is the phosphorescence quenching technique due to their advantages discussed earlier. However, the electrochemical oxygen sensors are unique in many ways to overcome problems in optical sensors such as optimizing dye loading concentration and photo bleaching, thus providing alternative means to measure oxygen tension at a lower cost [73], [74]. Moreover, optical sensor consists of a light-emitting diode and photodetector [75] in addition to the sensing element, which requires more power than its electrochemical counterpart and limits the lifetime of an implanted system operating on a battery. In addition, the driver circuits for optical sensors are usually more complicated than the electrochemical sensors, which largely increases the footprint of the system. The electrochemical sensing systems are, therefore, more desirable in applications where small footprint, long life-time, and wireless data transmission capability are preferred.

In Chapter 2, we have explored the potential of Clark-type sensor and successfully developed a biocompatible sensor using microfabrication technologies and integrated

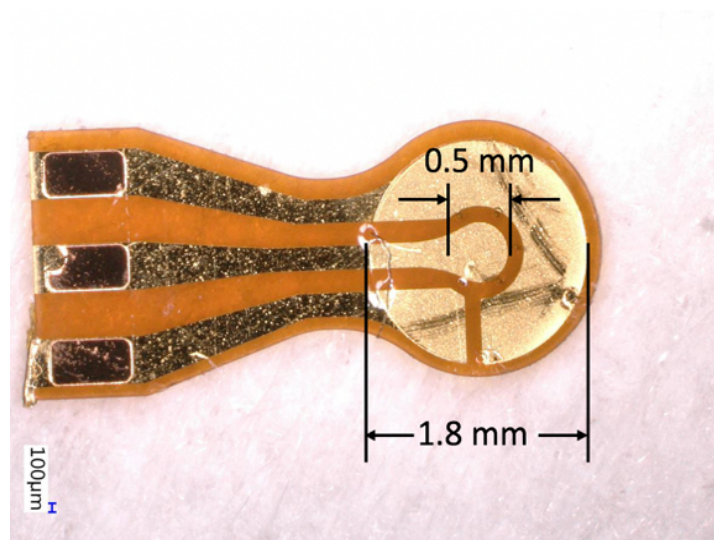
such techniques into small form factor systems with wireless data transmission capability. The sensor features two-point (e.g. oxygen-depleted point and oxygen-saturated point) calibration, and is easy to maintain as it exhibits minimum calibration drift over semi-chronic time periods (e.g. two weeks). In addition, unlike standard Clark sensors, there is no net consumption of oxygen in the sensor. This chapter further examines the performance of the sensor in the presence of changing environments (e.g. pH, oxygen diffusion rate) and disruptions (e.g. electrical signal noise) induced from tissue fraction and motion during sensor implantation. We recognized the individual factors in physiological environments, improved the test method to adapt to *in vivo* applications and explored the use of anesthetized mouse and zebrafish models to further validate the sensor's ability to measure real-time oxygen tension *in vivo*.

### **3.2 Sensor design and test method**

#### **3.2.1 Small sensor design**

The sensor is designed and fabricated by the same method described in Chapter 2. However, a smaller planar footprint is used to adapt to the small animal models. As shown in Fig. 25, the dimension of the oxygen sensor is  $1.8\text{ mm} \times 5\text{ mm} \times 0.3\text{ mm}$ , with a slimmer neck in the middle. Leaving out the connecting wires and solder pad region, the functional region of the sensor is 1.8 mm in diameter, comprised of three electrodes (working, counter and reference electrodes), an electrolyte reservoir filled with liquid electrolyte, and a semipermeable membrane for oxygen introduction. The distance between the cathode surface and the gas permeable membrane is approximately 6  $\mu\text{m}$ ,

providing an inner electrolyte system of  $0.015 \text{ mm}^3$ . The cathode area for maximum signal saturation is set to approximately  $0.2 \text{ mm}^2$ . Surface area ratio of the working, reference, and counter electrodes is approximately 1:1:4, with a working electrode footprint of 0.5 mm in diameter. Connections to the sensor for electrical readout are made using enamel-coated copper wire. As shown in Fig. 25 (b), the enamel insulation is scratched off only in the tip region of the wire. Soldering was performed for electrical connection, and exposed contacts were encapsulated with UV-curable encapsulant (Dymax 3041) to provide strain relief and to prevent liquid ingress. Additional medical-grade encapsulant (Dymax 1072-M) was applied to cover the Dymax 3041 to further protect the solder junction and ensure biocompatibility of the sensor.



(a)



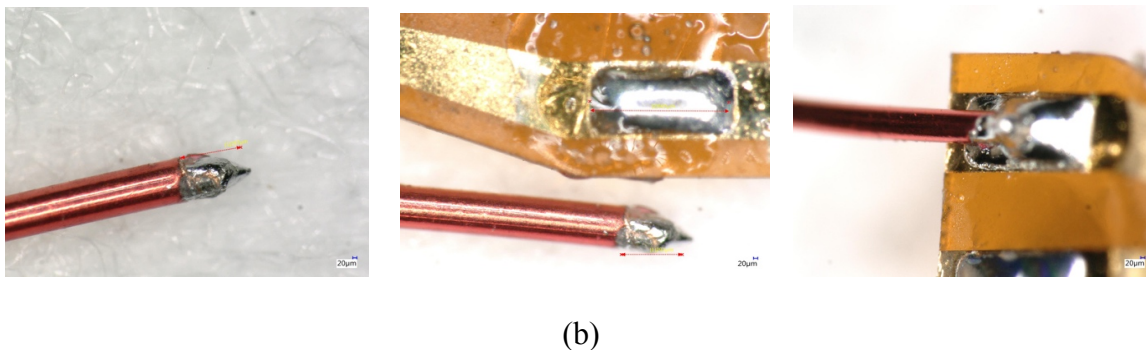


Figure 25. Optical image of (a) the fabricated sensor; (b) wire and solder pad before and after soldering.

### 3.2.2 Sensor test method

Linear sweep voltammetry (LSV) was used to overcome the quantitative error in data collection caused by drift in the reference electrode in chapter 2. To understand this method more quantitatively in the context of animal tests, a semiquantitative analysis was performed to understand oxygen concentration as a function of geometry, applied LSV voltage, and other sensor parameters. As the bias voltage increases in LSV measurements, the change in oxygen concentration with time and distance is shown in Fig. 26. The region close to the electrode's surface with concentration gradient is the diffusion layer and its thickness,  $\delta$ , is time dependent. LSV measurements of the sensor starting from a 0 V bias predict two regions: 1) the kinetic control region and 2) the diffusion control region. At low bias levels, the reaction at the working electrode is in the kinetic control region where the reaction rate has a strong dependence on the applied voltage. At larger bias voltages, the transport of oxygen to the working electrode shifts from operating under kinetic control to being diffusion limited. The plateau current at the transition point

can be related to oxygen tension based upon Faraday's law and the diffusion equation, as follows:

$$I = nFAD(\partial C/\partial x)_{x=0} \quad (6)$$

where C is the partial concentration of oxygen, n is the number of electrons transferred per reduction event, F is Faraday's constant, A is the surface area of the working electrode, and D is the oxygen diffusion coefficient in the electrolyte. An estimative formula for this current expressed by Nernst, assuming the main limitation to mass transfer is across the boundary layer, is as follows:

$$I = nFADC_0/\delta \quad (7)$$

As discussed above, the LSV technique measures the plateau current to evaluate the oxygen concentration. Fig. 27 shows the estimated oxygen concentration gradients when the currents reach the plateau. At a lower scan rate, the reaction rate increases slowly, and the diffusion layer gradually extends away from the electrode surface until the diffusion gradient can no longer supply redox material at a rate to satisfy the reaction rate. At higher scan rates, the oxygen reduction rate increases rapidly, and thus the current reaches the diffusion limited region in shorter time, resulting in a thinner diffusion layer.

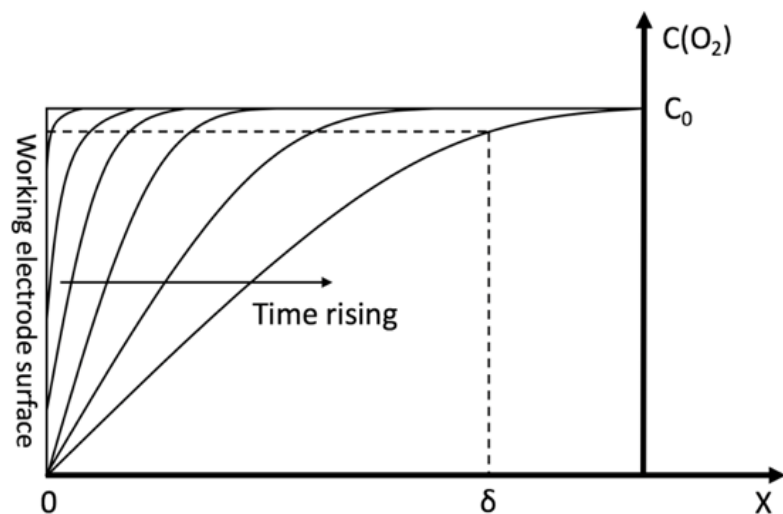


Figure 26. The change in oxygen concentration with time and distance as the bias voltage increases in LSV measurements.

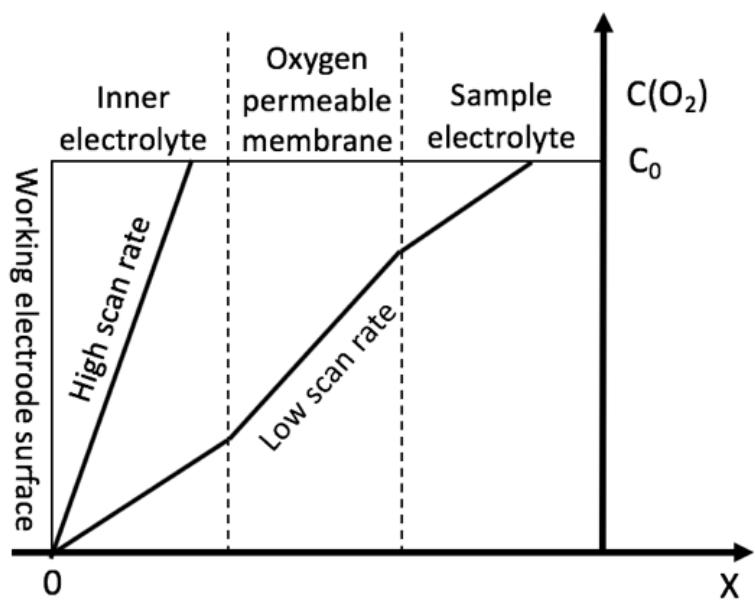


Figure 27. Estimated oxygen concentration gradients at the transition point from kinetic-controlled region to diffusion-limited region.

In the context of stable operation in benchtop tests, a choice of low scan rate (i.e. 5 mV/s) for the oxygen sensor has been experimentally proven to benefit the sensor stability in chapter 2. However, to minimize the influence of oxygen transport property in the sample electrolyte on the sensor sensitivity, a higher scan rate might be preferable. Specifically, to achieve consistent sensitivity among samples with different oxygen diffusion coefficient external to the sensor, conditions should be chosen that the oxygen diffusion impedance at plateau current is exclusively determined by transport property of the inner electrolyte, which outweighs the contributions of the electrolyte outside of the sensor by as great a margin as possible. The diffusion layer needs to be kept within the inner electrolyte, so that the influence of membrane tension and oxygen transport properties in the sample electrolyte layer can be minimized. Therefore, for in vivo applications where the sensor is calibrated in a liquid electrolyte but used in the animal tissue, a scan rate of 25 mV/s is used for the LSV measurements.

### 3.2.3 Animal test methods

Oxygen levels in mouse gluteus muscle and zebrafish trunk muscle are both investigated using the sensing system. The sensors are selected such that the residual current (the current produced by the sensor when exposed to a medium containing no oxygen) is negligible in comparison with the signals of interest, specifically, in the range from 0.01% to 1% of the signal generated in air-saturated water. Hence the stability of residual currents in changing conditions (i.e. pH, temperature, etc.) is of little interest and single-point (e.g. oxygen-saturated point) recalibration can be used prior to implantation.

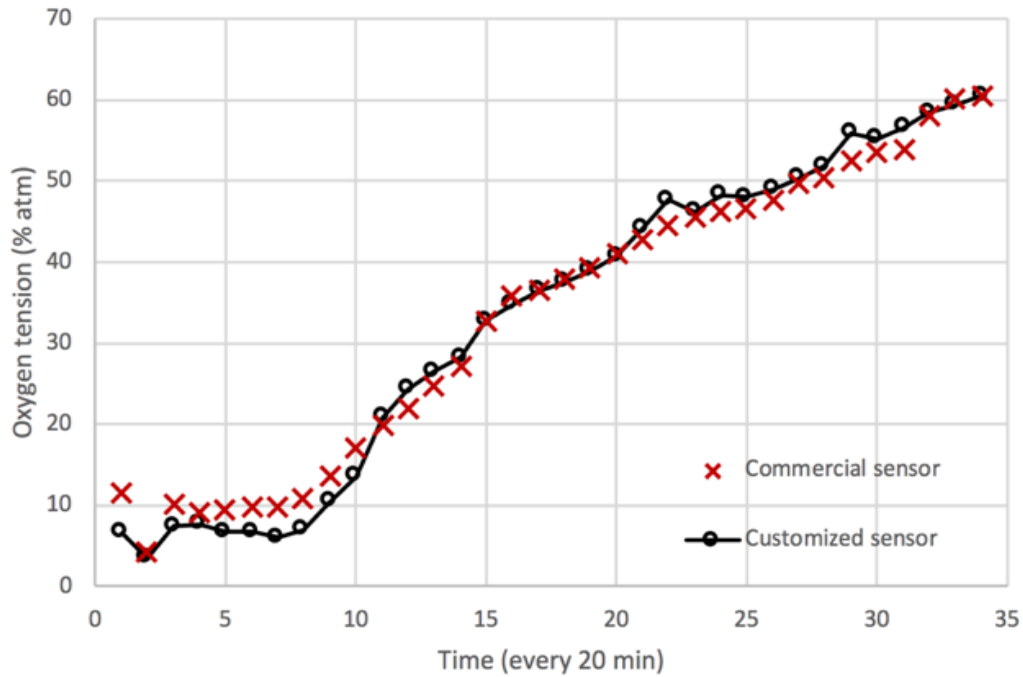
Prior to each in vivo experiment, the sensor is calibrated by immersing it in 0.1 M NaCl solution, which has been equilibrated with room air. After calibration was completed, all animals were anesthetized and stabilized throughout each experiment. Specifically, mice were anesthetized using 1.5% isoflurane delivered in room air, and zebrafish were anesthetized using tricaine. An incision is created through the skin over the expected location of the muscle under test, and the sensor was manually inserted in the muscle of an anesthetized animal, within 60 seconds from anaesthesia to insertion of sensor. The oxygen sensor should not be left in air for more than a brief period or it will dry out and fail. The active area of the sensor was kept moist with the working electrode site located as close as possible to the midpoint of the muscle. Single or periodic oxygen measurements were performed using LSV. During this time the GUI registers and display values in the curve mode, such that the sensor signals are visible. At the end of the measurement, sensors were retrieved from the muscle to confirm functionality. If the sensor is more than  $\pm 6\%$  off from the original saturated oxygen reading when it is removed from the animal, the measurement should be rejected or repeated.

### **3.3 Results and discussion**

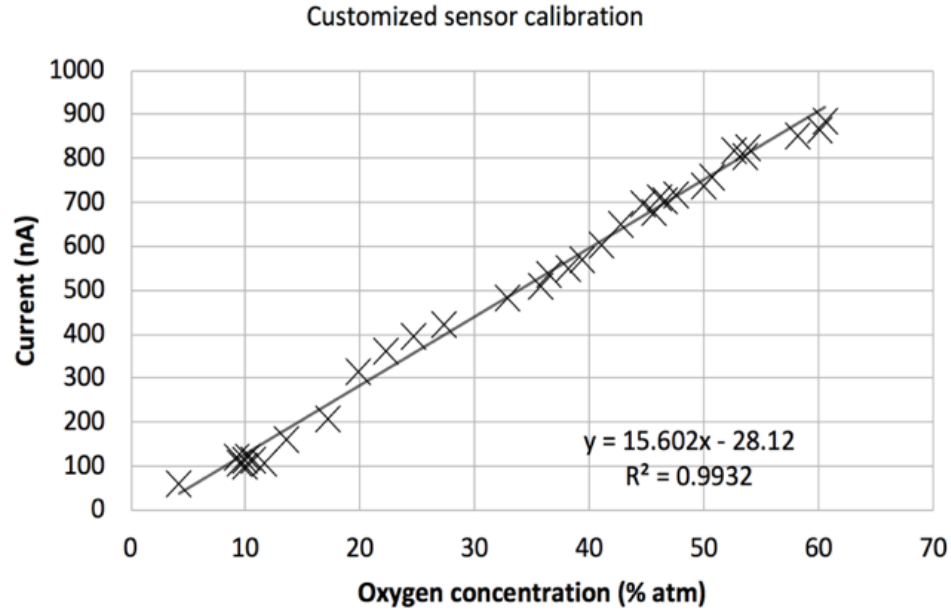
#### **3.3.1 Sensor characterization**

Sensitivity testing of the electrochemical sensor was performed by the same setup and commercial probe described in chapter 2. The bias potential between the working and reference electrodes was swept at a rate of 25 mV/s until the sensor reached the diffusion-limited regime. Fig. 28 shows the sensitivity characterization of the fabricated

electrochemical oxygen sensor obtained by cross-referencing to a commercial oxygen probe. Fig. 28(a) shows measurements performed periodically by LSV every 20 minutes until oxygen concentration in the sample electrolyte exceeds the physiologically relevant range (i.e. 0-60 atm% oxygen). Fig. 28(b) shows the sensor output current cross referenced to the oxygen measurement from the commercial oxygen sensor. The fabricated sensor demonstrated an oxygen response of approximately -15 nA/atm.% and excellent linearity across a range of physiologically relevant concentrations (i.e. 0-60 atm% oxygen); linear regression yielded a correlation coefficient of 0.9932.



(a)



(b)

Figure 28. Sensitivity characterization of the fabricated electrochemical oxygen sensor. (a) Oxygen tensions measured periodically by LSV every 20 minutes. (b) Output current of the customized sensor cross referenced to the oxygen measurement from the commercial oxygen sensor.

Fig. 29 shows the LSV curves of an oxygen sensor tested under saturated oxygen state at different scan rates. The plateau current of the same sensor increases as the scan rate increases. At a scan rate of 25 mV/s, the diffusion limited plateau current is approximately 800 nA. The estimated diffusion layer thickness is approximately 2  $\mu\text{m}$  according to Eq. 7. Since the inner electrolyte (i.e. 6  $\mu\text{m}$ ) is thicker than the diffusion layer by a great margin, the influence of oxygen transport in sample electrolyte on the sensor sensitivity can potentially be minimized. To further validate the consistency in sensitivity, PVA solutions with different PVA/water mass ratios are used as test environments with different oxygen diffusion properties. The oxygen diffusion

coefficient reported for water at 37 °C is  $3.8 \times 10^{-5} \text{ cm}^2/\text{s}$  [76], and PVA can bring down the oxygen diffusion coefficient in water by approximately 60 % when PVA mass fraction in the solution is 20% [77]. Fig. 30 shows the sensor readouts at both oxygen-saturated and oxygen-depleted states in samples with different PVA concentration, validating that at a scan rate of 25 mV/s, sensor sensitivity is consistent in samples with oxygen diffusion coefficient ranging from approximately  $1.5 \times 10^{-5} \text{ cm}^2/\text{s}$  to  $3.8 \times 10^{-5} \text{ cm}^2/\text{s}$ . The reported oxygen diffusion coefficient in muscle is  $1.8 - 2.4 \times 10^{-5} \text{ cm}^2/\text{s}$  at 37 °C [76]. Therefore, the sensor can be calibrated in water and then used in the animal muscle tissue, without altering the sensitivity.

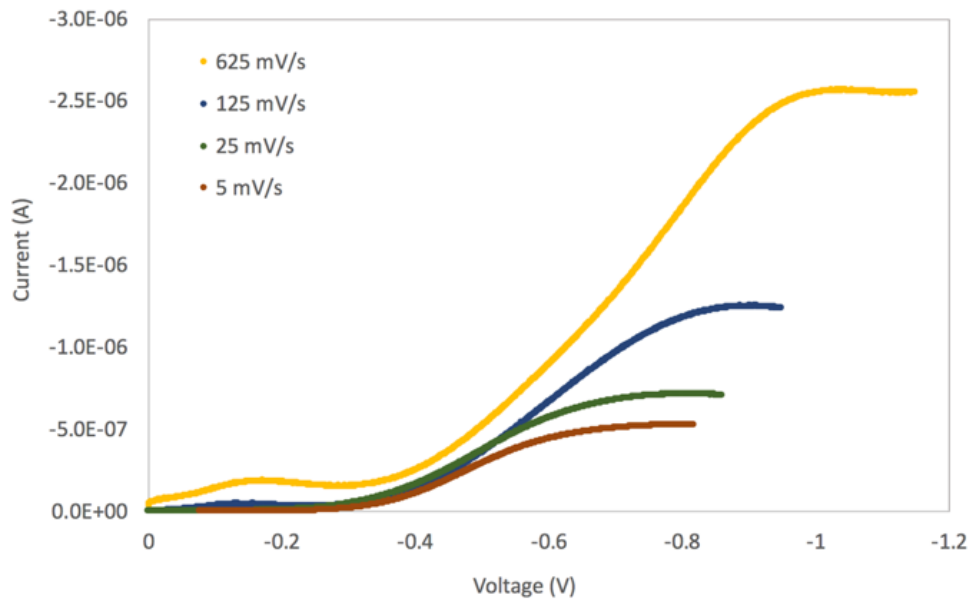


Figure 29. LSV curves for a sensor tested under saturated oxygen state at 5 mV/s, 25 mV/s, 125 mV/s and 625 mV/s, respectively.



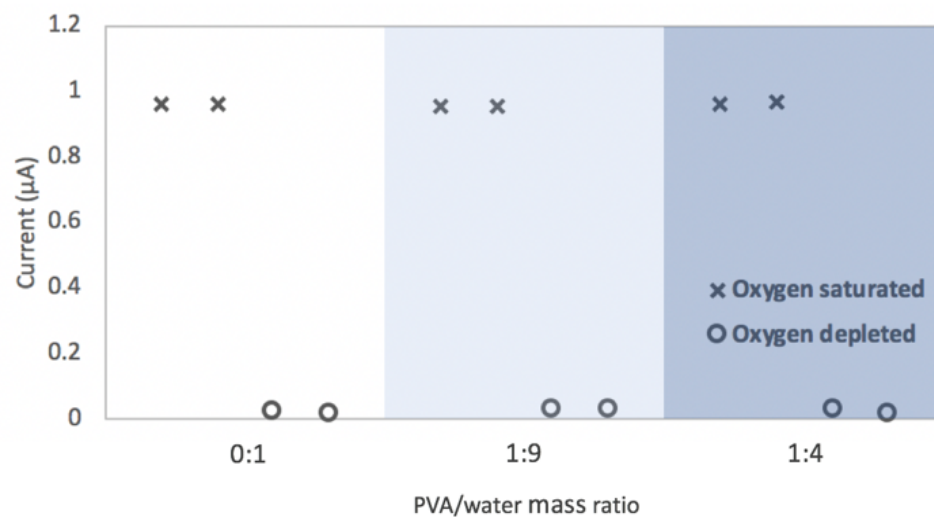


Figure 30. Sensor readout at both full-oxygen and oxygen-depleted states in PVA solutions with a PVA/water mass ratio of 0:1, 1:9 and 1:4, respectively.

Benchtop tests are mostly taken in 0.1 M NaCl solutions, while the actual muscle tissue pH varies in a small range (i.e. 6.96 - 7.68 in skeletal muscle). To validate its performance in a large pH range including the physiologically relevant span, the sensor was characterized in solutions with pH values of 5.2 and 7.8, respectively. To emulate the in vivo environment where the sensor would be surrounded by physiological fluid, simulated body fluid (SBF) was used as its composition approximates the inorganic content of human blood plasma. Tris ( $((\text{CH}_2\text{OH})_3\text{CNH}_2)$ ) and hydrochloric acid (HCl) were used to shift the pH of simulated body fluid (SBF) to designed values. Fig. 31 shows the calibration curve of a sensor in both basic and acidic solutions, indicating that the sensitivity of the sensor is invariant in the presence of changing pH in the external environment.

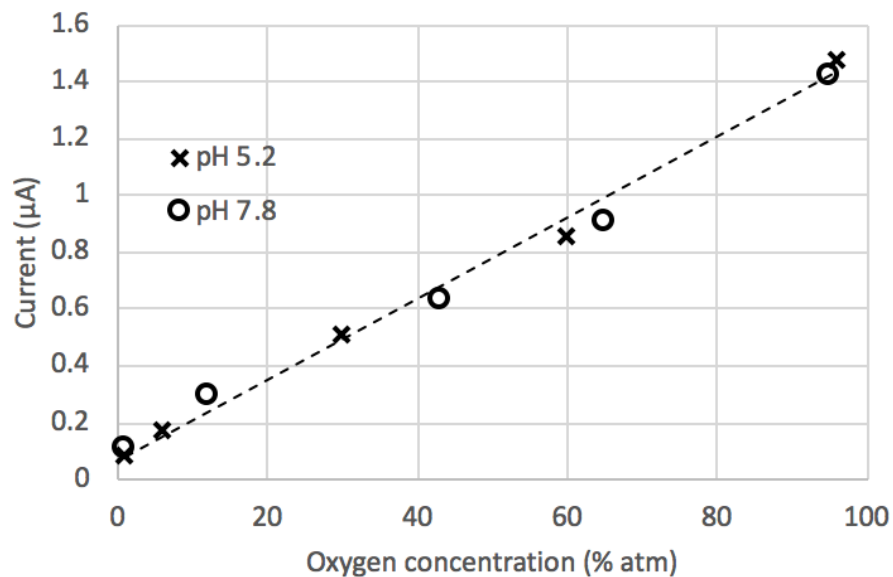


Figure 31. The sensitivity results of the sensor tested in solutions with pH values of 5.2 and 7.8, respectively.

### 3.3.2 *In vivo* test results

Fig. 32 shows the *in vivo* and *ex vivo* LSV results using the oxygen sensor connected to the customized potentiostat. As discussed, the inherent analog noise and transient noise delivered by vibrations of the sensor or turbulence in the environment can be easily filtered by the moving average filter. Therefore, both I-V curves demonstrate clear plateau for extracting the corresponded limiting reduction current.

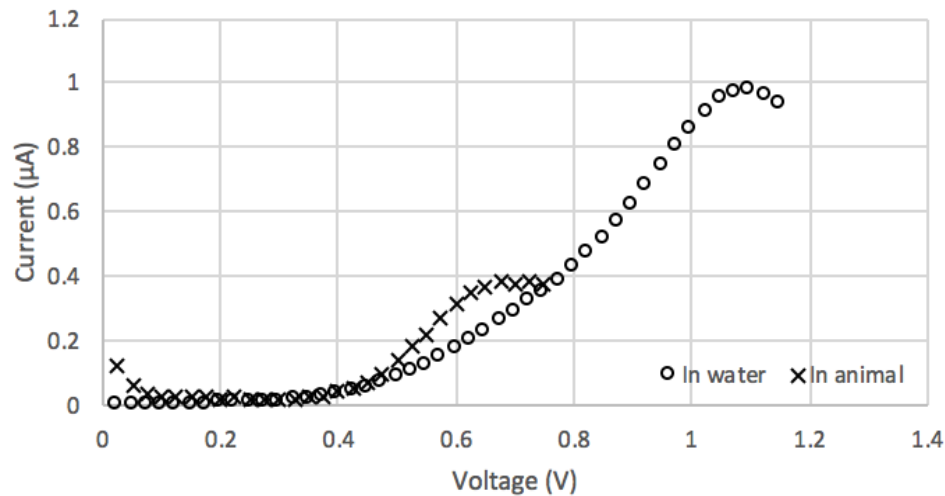


Figure 32. End to end testing of the oxygen sensing system *in vivo* and *ex vivo*.

Periodic measurements *in vivo* were performed using LSV, which lasts for about 50 s, followed by a rest period of about 10 s, repeated 4 times continuously for the duration of the experiment. After *in vivo* measurements, sensors were retrieved from the muscle and measurement in air-saturated water was obtained and confirmed to be around 160 Torr. Fig. 33 shows an example of data recorded for the animal models. In mouse model, the oxygen tension changes from 38 Torr to 27 Torr under general anesthesia, higher on the first point of measurement, and stabilizes on the following 3 measurements (27 – 29 Torr), while in fish model, continuous decrease from 22 Torr to 4 Torr is observed.

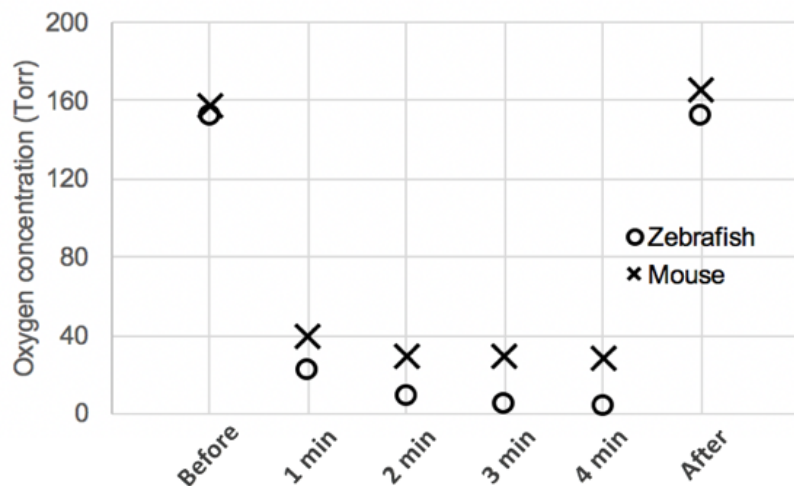


Figure 33. *In vivo* test results for mouse and zebrafish models, respectively.

Fig. 34 shows a comparison of the *in vivo* results of the oxygen levels in mouse and fish. The continuous tissue oxygen measurement in mouse gluteus muscle shown in Fig. 33 may be first falsely raised by 1) the introduction of any air bubbles trapped in the insertion site or 2) accumulation of arterial blood on the incision wound, and later equilibrated with muscle oxygen during testing. Therefore, muscle oxygen tension values for mouse model shown in Fig. 34 are determined by the second minute point after sensor insertion, where the signal tends to stabilize. In the zebrafish model, a small incision pocket was made within 2 mm under the skin to cut through the trunk muscle, which is about the same size as the functional area of the sensor. Unlike in the mouse model, the incision pocket closes up nicely after sensor insertion, leaving no room for accumulation of air bubble or blood during test. However, acute bleeding was observed during testing, which significantly disrupted the blood flow carrying oxygen to the muscle site, leading to a continuous decrease of oxygen tension. Therefore, muscle oxygen tension values for fish model shown in Fig. 13 are determined by the first sensor readout after insertion. The

preliminary studies in zebrafish ( $n = 15$ ) and mice ( $n = 15$ ) show average oxygen levels of 24 Torr and 36 Torr, respectively, which is within the physiological oxygen tension range. The standard deviation of oxygen tension in zebrafish and mice models are 13 and 10, respectively. The variation in each animal model might be caused by the heterogeneous distribution of oxygen tension in tissue and the incision-induced disruptions in the local equilibrium such as platelets aggregation and compromised tissue perfusion.

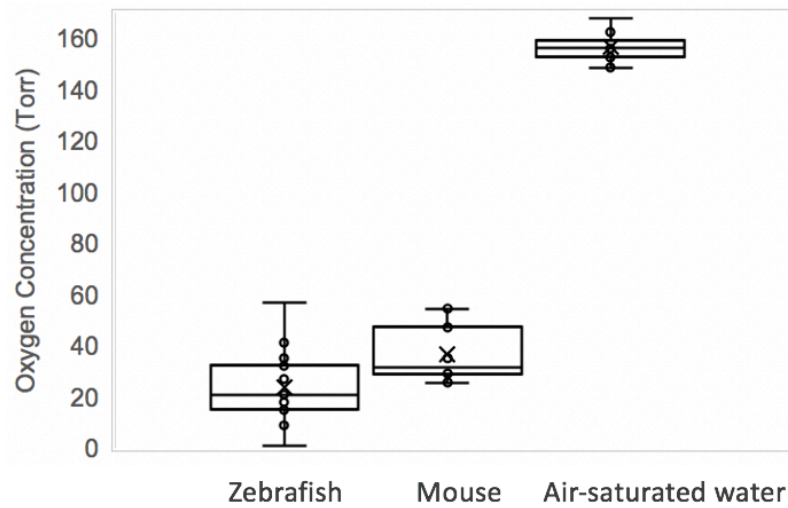


Figure 34. *In vivo* result of oxygen level in mouse and fish models. The average oxygen levels of mouse glueous muscle and fish trunk muscle are 36 Torr and 24 Torr, respectively ( $n=15$  each).

### 3.3.3 Critical problems causing device drift/failure

As discussed earlier, exposed contacts need to be encapsulated with Dymax 3041 to provide strain relief and to prevent liquid ingress. Additional medical-grade encapsulant (Dymax 1072-M) can be applied to cover Dymax 3041 to further protect the solder junction and ensure biocompatibility of the sensor. Incomplete encapsulation often causes

liquid ingress and deteriorates the functionality of the sensor. Oxidation of the solder junction is also observed when 1) the insulation layer of the enameled wire is broken or 2) excess amount of solder is applied during soldering. A pictorial history of the sensor pad over a one-week duration is shown in Fig. 35. Initially, no obvious change is observed, but the sensor performance is unstable. As the degradation of the solder junction continues, current output of the sensor starts to increase, green copper oxides begin to be observed, consistent with oxidation of the copper pad and copper wire. Finally, the sensor broke due to continuous liquid ingress and corrosion of the solder junction.



Figure 35. A pictorial history of the sensor pad over a one-week duration.

### 3.5 Summary

This chapter further examined the miniaturized oxygen sensing system composed of a Clark-type sensor and a customized potentiostat platform. Sensors with smaller planar dimension were fabricated using MEMS technology and their performances were examined. Specifically, the sensors demonstrated good linearity, consistent sensitivity in solutions with different pH and oxygen transport properties. The feasibility of the

prototype oxygen system for measuring oxygen level in muscle tissue is justified via a series of benchtop experiments, and mouse[78] and zebrafish models are explored to validate the sensor's ability to measure dynamic oxygen tensions *in vivo*.

## **CHAPTER 4 BIODEGRADABLE BATTERY WITH IMMOBLIZED ELECTROLYTE**

### **4.1 Background and motivation**

MEMS devices have been extensively used for sensing and modulation of a medical or environmental event to provide a means to improve patient health [79] or sustain environmental protection. Many biocompatible MEMS devices, either passive or active, have achieved commercial success [9]. Some typical examples include stents for treating narrowed arteries [80], [81], actuators for pacing monitoring cardiovascular events [82], [83], sensors for monitoring pollutants present in the atmosphere and in water [43], [84]–[86], and electrodes for neuromodulation [23], [24], [81], [87], [88]. In some cases, however, the medical or environmental need is transient; and as a result, permanent devices can persist long after they are needed. Such persistence can result in undesired problems; for example, in biomedical applications chronic implants can be susceptible to persistent inflammation and may require revision surgeries for device extraction after their functional lifetime. Recently emerging transient implantable medical devices (TIMDs) have garnered increasing interest due to their potential to eliminate the risks associated with permanent implants [31], [89] when treating or monitoring acute conditions. Specifically, TIMDs can breakdown into non-toxic components after a targeted lifespan, which excludes the need for revision surgery to remove the device and reduces the risk of chronic inflammatory response frequently observed with permanent implanted devices. This feature of TIMDs makes them more desirable in the monitoring and treatment of diseases and injuries that are transient in nature, such as bone fracture,



traumatic brain injury, wound healing and drug delivery systems. An example is the wireless radio frequency (RF) pressure sensor demonstrated by Luo et al. [90]. The sensor comprises zinc/iron bilayers as the sensor conductor material, and biodegradable polymers poly-L-lactide (PLLA) and polycaprolactone (PCL) as dielectric and structural materials. The functional lifetime of the sensors was approximately four days, and can be tailored by the choice of polymer encapsulation and ratio of the zinc/iron galvanic couple. Passive telemetry by analog inductive coupling is implemented in the operating frequency range of 10-100 MHz. Output power of the sensor is between 10-250 mW and the signal strength along the coil axis decreases as the third power of distance.

Compared to chronic devices, demonstrated TIMDs are still limited in functionality and application domain. There are many challenges that limit the development of biodegradable devices with more advanced functions and higher performance [13], [17]. One prominent challenge is accommodating onboard powering to overcome the constraint of passive designs or wireless powering, and to support the design of self-powered TIMDs, which can potentially demonstrate higher performance over longer time intervals and exhibit greater functionality. Therefore, the realization of a similarly biodegradable energy source is an essential component in developing biodegradable implants to facile handling transient injuries and diseases.

The work in energy sources featuring biodegradability and biocompatibility remains relatively unexplored. Researchers are still coming to grips with different types of transient batteries that offer output powers useful for the target class of devices [31], [36], [91]–[94]. Other practical challenges associated with the battery design include output

stability, device compactness, and life time (including shelf life and operation life span) of the battery. Yin et al. [31] demonstrated a series of biodegradable batteries featuring magnesium (Mg) as the anode, iron (Fe), molybdenum (Mo), or tungsten (W) as the cathode, and phosphate-buffered saline (PBS) as the electrolyte. This approach packaged all the battery components including the electrolyte within a cell and provided a constant electrochemical environment for stable operation of the battery. However, this structure incorporated liquid electrolyte at the expense of amenability to assembly and battery compactness. Electrolyte needs to be manually injected into the battery prior to implantation to eliminate corrosion of the electrodes for longer shelf life. In addition, this structure did not feature an insulating layer between anode and cathode, which might lead to short circuit of the electrodes within the liquid electrolyte. Jimbo and Miki [92] reported an ingestible battery that is activated upon exposure to the gastric fluid, which eliminated the need to design for a bulky electrolyte and automatically simplified battery component integration and prolonged shelf life. While this approach achieved compactness by harnessing the surrounding body fluid, the electrochemical cell design did not allow for encapsulation of the electrolyte to obtain stable battery performance in the presence of varying external aqueous conditions. The discharge profile of the battery was very unstable and the output current was susceptible to transient spikes.

This study presents the design, fabrication and testing of a biodegradable battery that satisfies the powering requirements for the target class of electronics and features easy integration, automatic activation, prolonged shelf life and improved stability. In our attempt to address the challenge of accommodating the bulk volume of the battery

electrolyte, we integrated the anode/cathode pair with a solid electrolyte system that supports compact packaging. Specifically, this design comprises a Mg/Fe galvanic pair as the electrodes, and an immobilized electrolyte system which simultaneously utilizes body fluid as an element of the electrolyte. This approach harnessed the physiological solution by allowing a minimum amount of body fluid to penetrate and activate the battery, while maintaining a constant electrolytic environment within the cell for the stable powering of transient TIMDs.

## **4.2 Materials and Design**

### **4.2.1 Battery Design and Working Principle**

The envisioned structure of the biodegradable battery is summarized in Fig. 36. The battery consists of two key functional components: (1) a Mg/Fe galvanic couple and (2) a NaCl/PCL electrochemical cell. Mg is incorporated as a sacrificial anode that galvanically protects an Fe cathode and powers the external device. NaCl particles are dispersed in PCL to form a solid system to serve as immobilized electrolyte, which defines the size of the battery. The top side of the NaCl/PCL cell is encapsulated by a laminated layer of PCL that dually serves as the packaging for the battery and a semipermeable membrane for infiltration of the electrolyte. A thick PLA film on the bottom side of the electrochemical cell, together with a PLA spacer, is used to emboss the electrode pair and confine the NaCl/PCL composite within the cell.

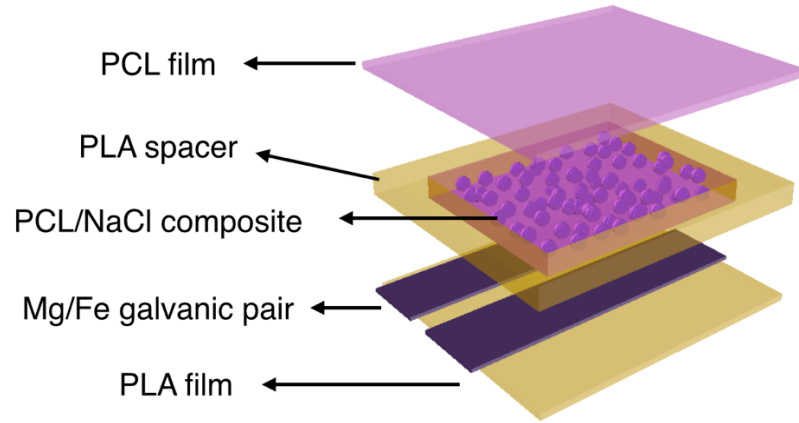


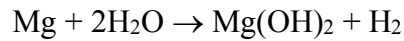
Figure 36. Schematic diagram of immobilized electrolyte biodegradable battery.

The constituent materials of the battery are all biocompatible, and spontaneously break down into non-toxic components after the functional life span of the battery[95]–[100]. Polycaprolactone is selected as the primary component of the solid electrolyte system due to its attractive chemical, mechanical, and physiological properties. Polycaprolactone has a very low glass-transition temperature ( $T_g$ ) of about  $-60\text{ }^{\circ}\text{C}$  and a melting temperature around  $60\text{ }^{\circ}\text{C}$ . Therefore, polycaprolactone is in the rubbery state at body temperature where it is soft and flexible and exhibits high permeability to low molecular weight species. In addition, polycaprolactone could be easily integrated with microfabrication techniques due to its low melting point and good solubility in a wide range of organic solvents including tetrahydrofuran, chloroform, acetone and ethyl acetate. Further, both polycaprolactone and polylactic acid have been demonstrated in long-term drug delivery systems and structural implants with confirmed biocompatibility in vivo. In turn, polylactic acid is selected as material for the supporting spacer structure because it has good tensile strength and is remarkably compatible with polycaprolactone. Sodium

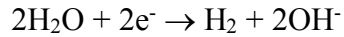
chloride is the ideal material for the electrolyte system since  $\text{Na}^+$  and  $\text{Cl}^-$  are the main ionic constituents of the body fluid. Mg/Fe galvanic couple is chosen as the anode/cathode pair because it has been previously investigated and proven to be a great candidate for the construction of biodegradable batteries. The anodic reaction of the electrochemical cell is given by:



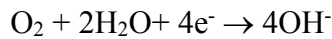
and the oxidation of Mg releases electrons into the external part of the circuit. The following side reaction also takes place on the anode and forms hydrogen gas and magnesium hydroxide ( $\text{Mg}(\text{OH})_2$ ) simultaneously:



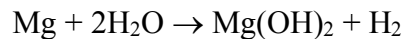
The cathodic reaction is dominated by hydrogen evolution:



while oxygen reduction reaction is limited by the amount of oxygen diffused onto the surface of the cathode. The following oxygen reduction is therefore considered as a side reaction:



Consequently, the overall governing reaction of the battery is given by:



The activation of the battery requires the presence of water-based electrolyte to both act as a reactant on the cathode and serve as an ionic pathway for the completion of the battery circuit. We have shown in our previous work [30] that PCL film enables almost instantaneous penetration of physiological solution to activate the battery, and supports hydrogen diffusion. In the present design, the separate use of PCL in the encapsulating film and immobilized electrolyte permits greater flexibility in designing for electrochemical performance and compact packaging, as shown in Fig. 37. Much like a dry cell, liquid from the surrounding body permeates the immobilized electrolyte and activates the battery. The encapsulating PCL film would hinder the efflux of NaCl from the battery to confine the electrolyte within the electrochemical cell during battery discharge. Hydrogen gas formed during the battery discharge is released by diffusion across the thin PCL film. For longer functional time span of the battery, the PCL layer should selectively support water and hydrogen transport, but retard NaCl transport. Note that although the water necessary to form the aqueous environment within the cell is coming from the external environment, due to the excess of solid NaCl in the cell, the aqueous environment in the cell is held at the solid solubility limit of NaCl in water at the temperature of operation, independent (to first order) of the ionic composition of the external environment.

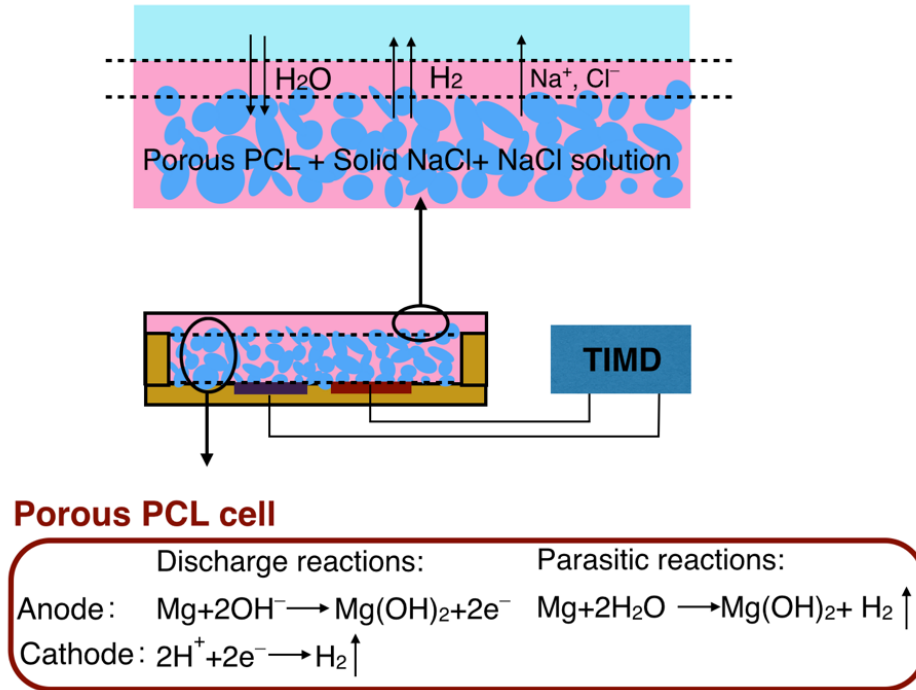


Figure 37. The principle of operation of the biodegradable battery. Liquid absorbed into the cell activates the battery by converting solid NaCl into a super saturated NaCl solution.  $\text{Na}^+$  and  $\text{Cl}^-$ , as well as hydrogen gas, leach out from the PCL film. The governing chemistry in the electrolytic cell is the cathodic protection of Fe through the oxidation of Mg anode and, parasitic corrosion of the Mg.

The schematic diagram of the circuit model representing the DC equivalence of the battery is shown in Fig. 38. The voltage  $V$  denotes the potential difference of the two half cells of the battery which varies with the parasitic reactions on the electrodes. A leakage path enabled by the parasitic corrosion reaction on the anode is denoted by the serial connection of  $R_1$  and  $R_3$ . When a closed loop circuit is formed at the terminals, the discharge current drawn from the battery flows through  $R_1$  and  $R_2$  and powers the external device. In the discharge loop,  $R_1$  denotes the ohmic resistance of the battery

which describes the polarization resistance and electrolyte resistance in the cell.  $R_2$  denotes the electrolyte resistance and connection resistance of the battery. The cumulative effect of side reactions need to be considered when understanding the parameters in the circuit model and evaluating the performance of battery.

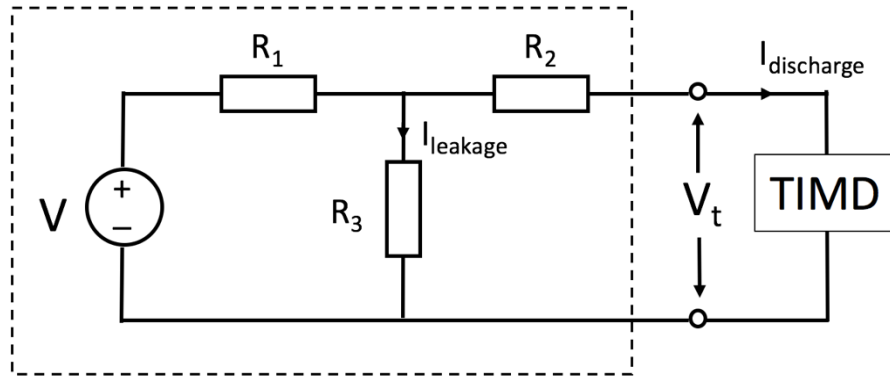


Figure 38. The schematic diagram of the circuit model.

### 4.3 Fabrication and assembly

The fabrication process of the immobilized electrolyte biodegradable battery is schematically shown in Fig. 39. The PCL/NaCl composite was prepared by solvent-casting. Commercial 80 kDa PCL pellets were solubilized in acetone at a concentration of 100 mg/mL. 150 g sodium chloride (NaCl) with a particle size of 300-400  $\mu\text{m}$  was dispersed in 100 mL PCL solution and casted. The composites were dried under ambient conditions for 24 hours and vacuum-dried to remove residual solvent for an additional 12 hours.



To define the solid electrolyte shape, a polylactic acid (PLA) spacer was fabricated using 3-D printing technology (Makerbot Replicator 2X). PLA was selected due to its high processing temperature (approximately 180 °C), which is inert to the following high temperature process of PCL. The solid electrolyte was molded into the PLA spacer with a lamination press at 65 °C, which is above the PCL melting point (approximately 61°C). The PCL/NaCl composite (93.75 wt% NaCl) then softened and adopted the shape defined by the spacer. Next, the Mg and Fe electrode pair was embossed onto one surface of the battery and encapsulated with an PLA film. Finally, a thin PCL film is laminated onto the opposite surface of the PCL/NaCl composite at 65 °C to seal the battery.

#### **4.4 Characterization and testing**

The permeability of NaCl in PCL films was characterized to support design of the battery packaging. Samples used to evaluate the barrier properties of the PCL structure were fabricated with same geometries as those used in the battery, except that no electrodes were incorporated. Samples were immersed in a large volume of deionized (DI) water (250 mL) to (1) establish zero concentration conditions of NaCl external to the battery and (2) minimize concentration changes in the external environment. At periodic time points, the samples were removed from the liquid, air-dried at slightly increased temperature (e.g. 35 °C) for 12 hr, and weighed to determine the rate of NaCl transport across the polymers. As discussed, the PCL layer should selectively support water and hydrogen transport, but retard NaCl transport. As high mass transfer resistance of NaCl is required to retain the electrolyte within the battery, PCL films with varying

thicknesses were compared to determine the optimum parameters that satisfy these mass transfer and battery discharge design constraints.

To further understand the role of water and its influence on the discharging behavior, batteries were tested under constant load discharge in a DI water environment. The batteries were dipped into water to evaluate the activation behavior. Additionally, after the battery stabilized after a certain period of time, it was removed from water to evaluate the deterioration in performance originated from loss of water. After the potential fell below the cutoff point, the battery was immersed in water for the second time to observe the subsequent performance of the battery.

The electrochemical performance of the battery was tested under galvanostatic conditions in a two-electrode-cell configuration at various discharge rates up to 0.1 mA/cm<sup>2</sup> using a potentiostat (WaveDriver 10, Pine Instruments). The batteries were discharged in 100 mL of SBF at 37 °C to emulate the physiological environment. The internal resistance ( $R_i$ ) and the open circuit voltage ( $V_{oc}$ ) of the battery can be investigated using the following equation:

$$V_t = V_{oc} - R_i \cdot I \quad (8)$$

where  $V_{oc}$ ,  $I$ ,  $R_i$  and  $V_t$  refer to the open circuit potential (V), discharge current (A), internal resistance ( $\Omega$ ), and output voltage (V) at the terminals of the cell, respectively. From the discharge data, we can plot a graph of terminal potential difference,  $V_t$ , against current,  $I$ , and find the internal resistance and the open circuit potential of the cell.

In addition, the batteries were tested in a series of liquids (i.e., either DI water, 0.1 M NaCl, and SBF) to investigate how the external ionic environment affects the ionic transport across the PCL encapsulation and stability of the immobilized electrolyte within the battery. The battery was first activated in DI water and discharged at a constant current of  $25 \mu\text{A}/\text{cm}^2$ . After 1 hour of stable discharge, the battery was removed from the DI water and immediately immersed into the NaCl solution. After another hour of stable discharge, the battery was immersed into SBF solution. Finally, the solution was again changed to DI water after another hour of stable discharge. The solution volumes were 200 mL and tests were performed under room temperature.

## **4.5 Results and Discussion**

### **4.5.1 Characterization of battery components**

Fig. 39 shows optical images of the PCL/NaCl composite and the configuration of the battery. The simple structure of the battery facilitates miniaturization. It is designed to have a volume approximately defined by the solid electrolyte system. The geometry of the presented batteries is depicted in Fig. 37. The battery has a solid electrolyte volume of  $12 \text{ mm} \times 10 \text{ mm} \times 2 \text{ mm}$ , which contains 0.48g NaCl/PCL composite (93.75 wt% NaCl), and the total size of the fabricated battery is  $16 \text{ mm} \times 16 \text{ mm} \times 2 \text{ mm}$ . Mg foil with  $0.45 \text{ cm}^2$  active area and thickness of  $45 \mu\text{m}$  was utilized in the battery, and the anode cathode spacing was 1 mm.

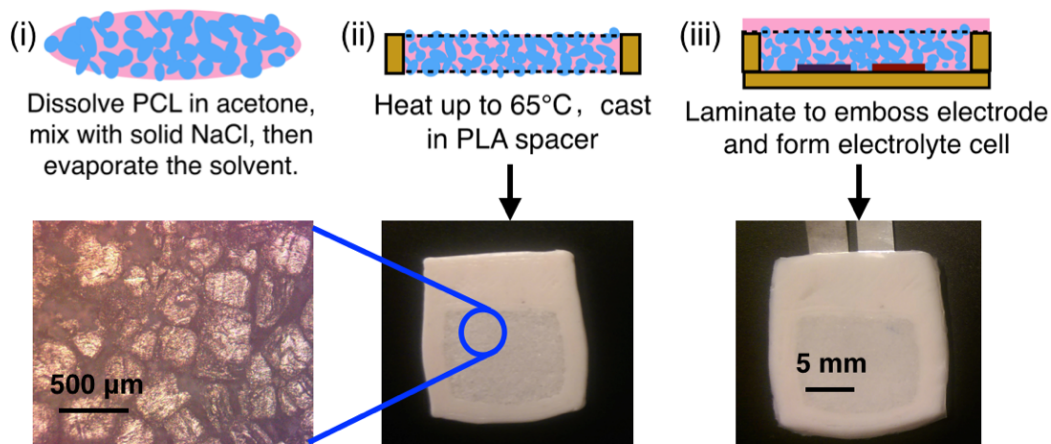


Figure 39. Fabrication process of the battery.

In order to find a suitable coating area and thickness of the PCL film for hindering NaCl efflux from the NaCl/PCL composite without appreciably increasing the mass transfer resistances of hydrogen and water, NaCl permeability tests were conducted to evaluate its diffusion properties in PCL. As shown in Fig. 40, the leaching of NaCl from the battery is hindered by the polymeric binder in the NaCl/PCL composite, as well as the PCL membrane encapsulating the composite. The leach rate of NaCl across 20  $\mu\text{m}$  and 50  $\mu\text{m}$  membranes were approximately 22  $\text{mg}/\text{cm}^2/\text{h}$  and 9  $\text{mg}/\text{cm}^2/\text{h}$ , respectively. These findings showed that the lifetime of the battery is limited by depletion of the active material (Mg), as well as loss of the solid electrolyte. For a battery to last more than 24 hr, a membrane between 30  $\mu\text{m}$  and 50  $\mu\text{m}$  thick has been experimental determined to be the optimum coating thickness for maximizing the stability and performance of the batteries. In addition, the battery depicted in Fig. 38 contains 0.45 g NaCl, which could

support stable discharge for about 40 hours, and 4 mg Mg, indicating that the battery lifetime in this configuration is limited by depletion of the anode.

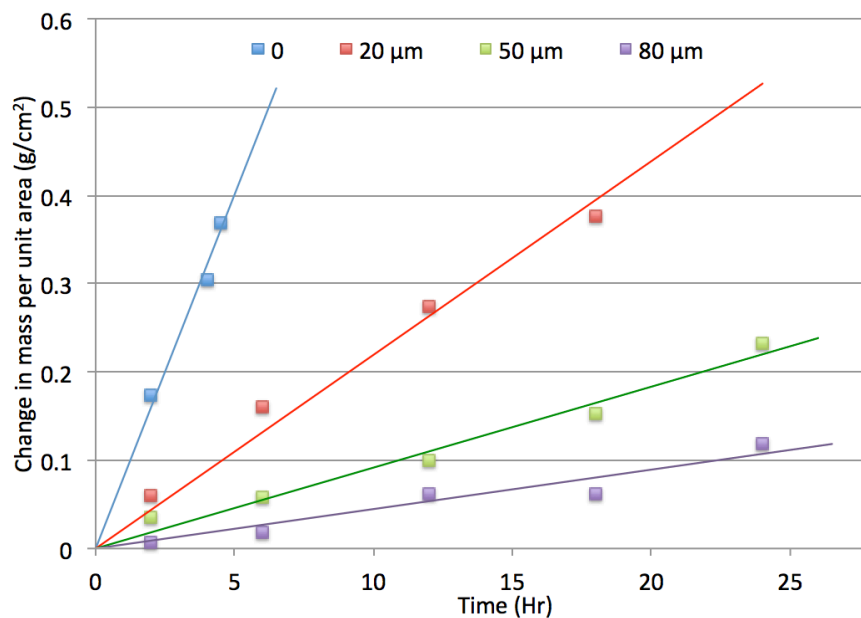


Figure 40. NaCl leach rate of the NaCl/PCL composite structure with top PCL membrane thickness of 0  $\mu\text{m}$ , 20  $\mu\text{m}$ , 50  $\mu\text{m}$ , 80  $\mu\text{m}$ , respectively.

Fig. 41 demonstrates the discharge behavior upon activation in DI water of four batteries with the same thickness of PCL membranes (30  $\mu\text{m}$ ). The output voltage of the battery statistically stabilized in 6 minutes, which demonstrated that the PCL structure allows sufficient water transport for activation of the battery. Increasing the PCL thickness to 50  $\mu\text{m}$  was experimentally proven to not appreciably prolong the activation time of the battery.

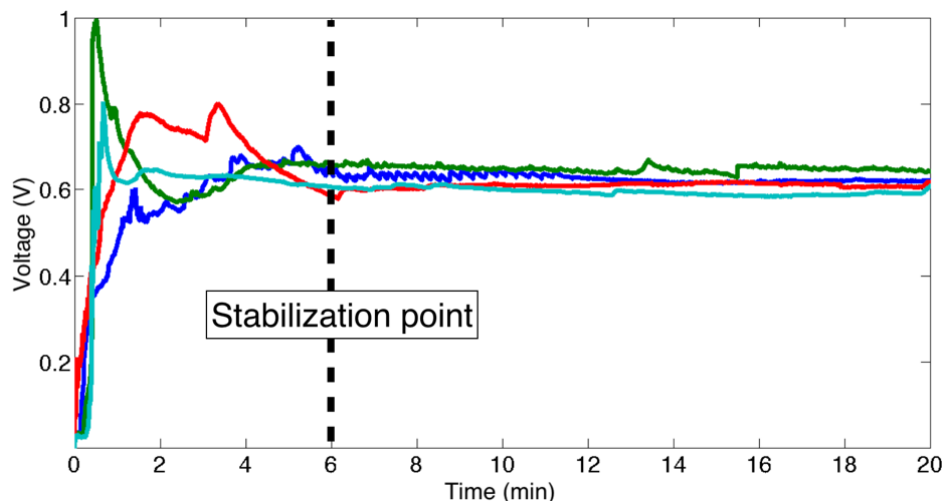


Figure 41. Discharge behavior upon activation of four batteries with the same configuration and discharge parameters.

After the battery was stabilized in DI water and discharged for 24 hours, it was removed from the water and continued with discharging. Fig. 42 shows that the liquid retained in the cell supported continued discharge for up to 6 hours in air. When the discharge potential fell below a cutoff potential of 0.1 V, immersion of the battery in water enabled the battery to resume to the steady state discharge potential after 10 minutes, verifying that the voltage decline or termination of the battery was caused by the consumption of water inside the battery. The deterioration in battery performance was due to the loss of water, as water is consumed in the governing reactions of the battery, as well as undergoes evaporation. These findings suggested that the PCL structure offers functional advantages for retaining the electrolyte even in air. Further, the PCL film was mechanically robust to accommodate for releasing of hydrogen during the discharge of

the battery for prolonged periods. It was also speculated that capillary force contributes to the fast absorbance of water, especially in the second immersion, and internal pressure might have contributed to the release of hydrogen from the PCL membrane.

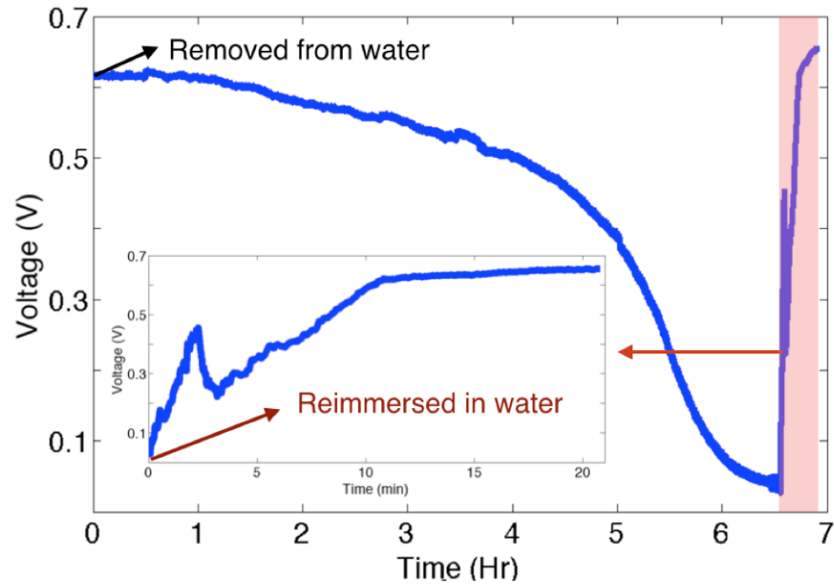


Figure 42. Discharge behavior of a battery removed from DI water after being discharged for 24 hours. The battery terminates in 6 hours due to liquid loss, and resumes its performance shortly after reimmersion in water for a second time.

#### 4.5.2 Electrochemical testing of biodegradable batteries

To emulate the *in vivo* environment where the battery would be surrounded by physiological fluid, electrochemical testing was conducted in SBF, as its composition approximates the inorganic content of human blood plasma. The discharge behavior with a PCL membrane thickness of 50  $\mu\text{m}$  is shown in Fig. 43. The operating voltages are approximately 0.95 V, 0.75 V and 0.45 V for discharge rates of 12.5  $\mu\text{A}/\text{cm}^2$ , 25  $\mu\text{A}/\text{cm}^2$

and  $0.1 \text{ mA/cm}^2$ , respectively. In each case, the terminal voltage is stable for at least 24 hours during the constant-current discharge. The current is linearly related to the voltage in relation to Ohm's law, which indicates that in applications involving a purely resistive load, the output current would still be fairly constant.

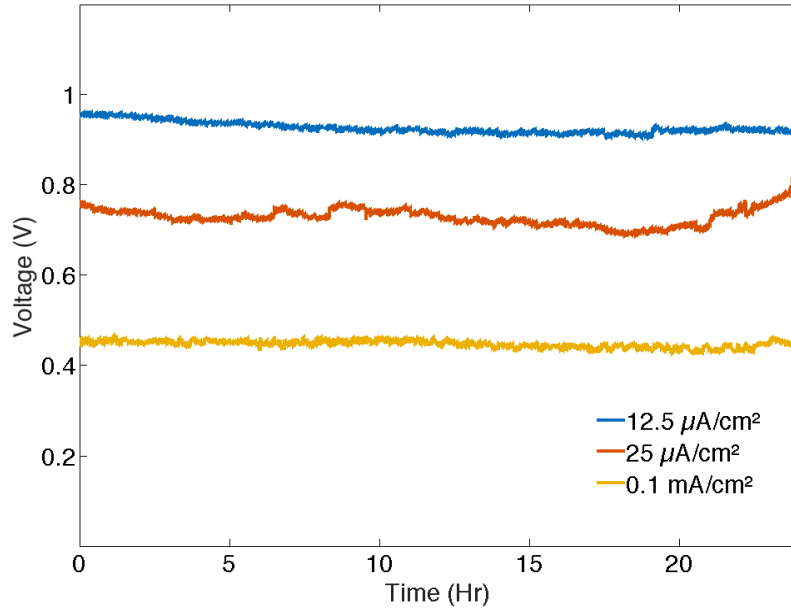


Figure 43. Discharging behavior under constant current. The operating voltages are approximately 0.95 V, 0.75 V and 0.45 V for discharge rates of  $12.5 \mu\text{A/cm}^2$ ,  $25 \mu\text{A/cm}^2$  and  $0.1 \text{ mA/cm}^2$ , respectively.

Fig. 44 illustrates how the battery behaves at different discharge currents. As discussed, the open circuit potential and internal resistance are related to terminal voltage and discharge current as described by equation (1). In this case,  $V_t$  changes nonlinearly with  $I$ , which leads to a varying  $V_{oc}$  and  $R_i$  at different discharge currents. At each current point, transient  $V_{oc}$  and  $R_i$  can be determined using an assisting tangent line, of which the



absolute value of the gradient is equal to  $R_i$ , and the intercept on the y-axis is equal to  $V_{oc}$ . Note that at increased discharge currents, there is a decline in both  $V_{oc}$  and  $R_i$ , as indicated by the dotted line. It is speculated that the higher  $V_{oc}$  and  $R_i$  observed at lower discharge current is attributed to the corrosion mechanism of magnesium. It has been previously demonstrated in other literatures[30], [95], [101] that magnesium features a passivation layer of  $Mg(OH)_2$  at the surface, and the discharge chemistry relies on the continuous formation and breakdown of the passivation layer. The formation of poorly soluble  $Mg(OH)_2$  film hinders the corrosion of magnesium, which may lead to both high leakage and discharge path resistances at low discharge rate. When a current is drawn from the battery, the  $Mg(OH)_2$  layer is mechanically disrupted to expose the underlying magnesium. As the current increases, the rate of film breakdown overcomes the rate of  $Mg(OH)_2$  reformation, which subsequently leads to a decrease in internal resistance.

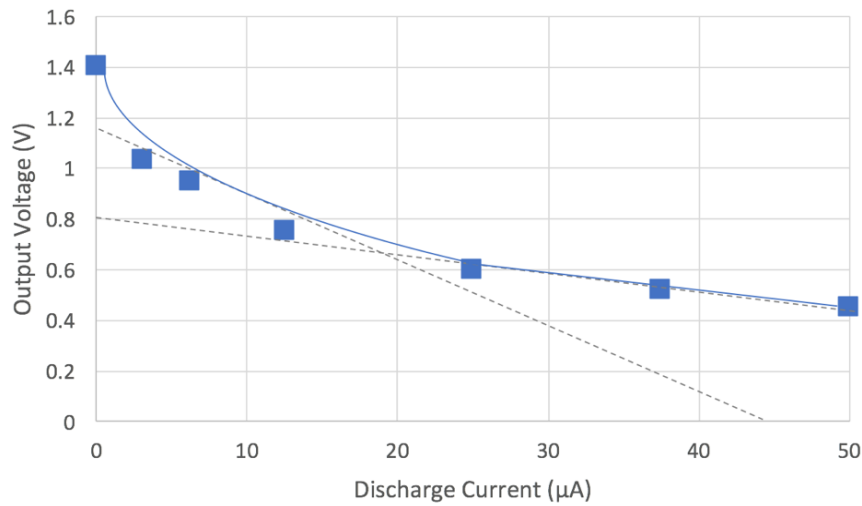


Figure 44. Battery terminal voltage at different discharge currents.  $V_t$  changes nonlinearly with  $I$  at smaller currents.

Physiological fluid, such as human blood plasma, comprises mainly of water (up to 95% v/v) and inorganic salts (e.g., NaCl). To demonstrate that the immobilized electrolyte approach renders the biodegradable battery immune to the external liquid environment, Fig. 45 shows the discharge of a battery sequentially in DI water, 0.1 M NaCl, and SBF. Further, the liquid solutions selected increasingly approximate the composition of human blood plasma. Hence, the stable discharge profile achieved from this experiment suggested that the performance of the presented battery is not susceptible to the surrounding physiological environment.

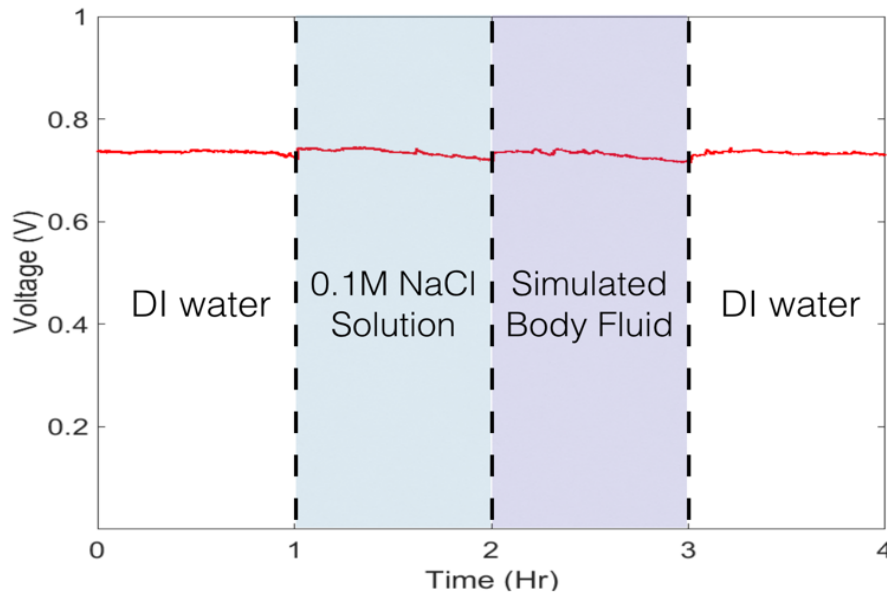


Figure 45. Discharging behavior under a constant current of  $25 \mu\text{A}/\text{cm}^2$ . The liquid volume outside of the battery was changed every one hour.

## 4.6 Summary

This chapter detailed an approach to achieving a biodegradable battery with immobilized electrolyte for transient implantable medical devices. Specifically, the battery features a Mg/Fe galvanic pair as the electrodes, and encapsulates a solid system comprising NaCl dispersed in a polymeric (PCL) volume. Since the ionic concentration within the encapsulation is high, the cell performance is reasonably independent of external environment as long as the internal moisture content and NaCl concentration remain above a threshold. This approach harnesses bodily fluid as an element of the electrolyte, thereby features auto activation of the battery and reduces processing complexity of sealing liquid within a cell. In addition, since the cell is ‘dry’ prior to implantation, this design eliminates concerns with shelf life and unwanted corrosion prior to desired use of the battery. Moreover, the battery encapsulation provides a barrier for retaining the electrolyte and potentials of preventing influx of large organic molecules, and the cell structure naturally prevents the short circuit of the electrodes. In addition, since the electrolyte is highly concentrated salt, the activity of the electrolyte space can be maintained at the saturation concentration of NaCl, thus providing the desired constant environment to support stable battery performance.

## **CHAPTER 5 BIODEGRADABLE OXYGEN SENSORS BASED ON GALVANIC CORROSION**

### **5.1 Background and motivation**

The present chapter explores the development of biodegradable oxygen sensors for implantable applications. Specifically, the findings from the previous chapters on biodegradable batteries and non-degradable oxygen sensors together informed the development of the work discussed in this chapter. The present objective is to demonstrate a biodegradable device that can break down into non-toxic components after a targeted lifespan, reducing the risk of chronic inflammatory response frequently observed with permanent devices. The underlying goal is to improve the approach to advance the postoperative monitoring of oxygen tension and provide an additional means to monitor a number of diseases and injuries that are transient in nature. Additionally, such sensors may have application in transient monitoring of the environment, such as environmental spills and algal tides. Ultimately, the development of the underlying fabrication technology for biodegradable active transducers will also allow others to exploit the technology for a variety of applications.

### **5.2 Materials and Design**

#### **5.2.1 Materials**

As discussed in chapter 1, PLA has been commonly used in biomedical applications ranging from tissue engineering devices to body implants. PLA is an aliphatic polyester

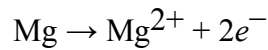
existing in three stereochemical forms (e.g. semi-crystalline poly(L-lactide) PLLA, poly (D-lactide) (PDLA) and amorphous poly(DL- lactide) (PDLLA)), which can chemically degrade in water/biofluids due to the hydrolytically unstable ester linkages in the backbone chain. The dissolution rate of PLA can be controlled by adjusting the molecular weight and chemical composition during the synthesis processes. In addition, PLA can be processed by solvent casting, spin casting and hot melting, which can be integrated with microfabrication techniques. Metals that exhibit corrosion behavior and degrade in water/biofluids are also used as biodegradable materials for implantable applications. Magnesium (Mg) is the most well-known and widely-used biocompatible and biodegradable metal. For example, Mg, and Mg alloys have been demonstrated in biodegradable stent applications due to their combination of high mechanical strength, fracture toughness, and non-toxicity. Besides Mg, alternative dissolvable metals, including iron (Fe), tungsten (W) and molybdenum (Mo), have been explored in broad applications of biodegradable electronics, such as transistors, sensors, and energy devices. When exposed to biofluids, these materials undergo corrosion and produce soluble ions, hydroxides, and/or oxides.

### 5.2.2 Sensor Design and Working Principle

The biodegradable oxygen sensor discussed here is based on the principle of competitive redox reactions; the presence of oxygen will promote one reaction over the other, leading to a difference of observable potential in the corroding redox couple. Consider two dissimilar metals in an electrolyte environment, supported by a biodegradable polymer

package such as PLA. Mg, due to its anodic electrochemical properties, is selected as the anode portion of the couple. Biodegradable metals Mo, Fe and W are compared for the cathode portion of the sensor, as demonstrated in the following section. Consider, for example, an Mg-Mo galvanic pair as shown in Fig. 46. The galvanic pair is embedded in a PLA substrate with the top surface exposed to the environment under test. The external physiological solution in the environment, which may contain oxygen, is harnessed as the electrolyte. The sensor is self-polarizing and derives electrical energy from spontaneous galvanic protection of Mo through the anodic oxidation of Mg.

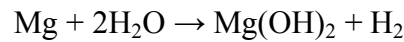
The oxidation of Mg takes place on the anode surface as follows:



and magnesium hydroxide ( $\text{Mg}(\text{OH})_2$ ) is formed from the following reaction:



The following side reaction also takes place on the anode and forms hydrogen gas and  $\text{Mg}(\text{OH})_2$  simultaneously:



The cathodic reaction of the electrochemical cell is given by:



At the cathode site, oxygen reduction produces a higher potential compared to that for hydrogen reduction, but has a current limited by the availability of oxygen; while hydrogen evolution enables improved current density, but with reduced output voltage.

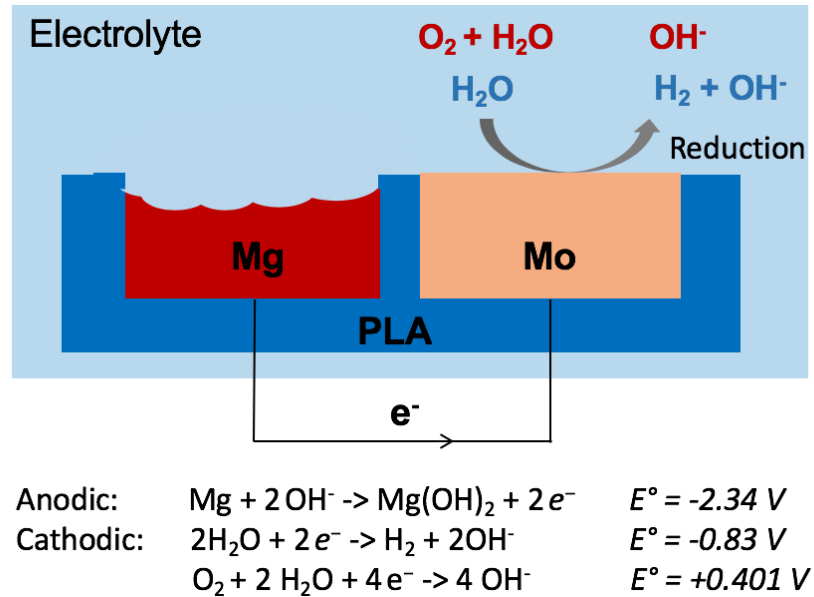


Figure 46. Schematic diagram of the biodegradable sensor.

We have discussed in the previous chapter that that magnesium features a passivation layer of  $Mg(OH)_2$  at the surface, and the discharge chemistry of the Mg-Fe galvanic pair relies on the continuous formation and breakdown of the passivation layer. The Mg anode of this Mg-Mo sensor also features the same chemical property: the formation of a poorly soluble  $Mg(OH)_2$  film that hinders the corrosion of magnesium, which may lead to high discharge path resistances at low discharge rate. When current is drawn from the electrochemical couple, the  $Mg(OH)_2$  layer is mechanically disrupted to expose the underlying Mg. As the current decreases, the rate of  $Mg(OH)_2$  reformation overcomes the

rate of film breakdown, which subsequently leads to an increase in internal resistance. Therefore, a relatively high discharge current density is needed to maintain a relatively consistent internal resistance. This need for a high current density discharge stands in contrast to the supply of oxygen limiting the total current achievable from the competing oxygen reduction reaction.

To ensure stable operation of the sensor as well as the ability to detect oxygen, the device is therefore operated in two modes: battery mode and sensor mode. As shown in Fig. 47, in battery mode, a relatively high current density (e.g. 1 mA/cm<sup>2</sup>) is drawn from the device to induce an excessive breakdown of the surface Mg(OH)<sub>2</sub> film and ensure a relatively constant anode surface area. In sensor mode, the current density drawn from the device is substantially reduced (e.g. 0.02 mA/cm<sup>2</sup>), since the oxygen reduction reaction plays an important role at low current densities. Cell voltage in sensor mode is measured to evaluate the oxygen concentration. Oxygen concentration in the vicinity of the sensor cathode is equilibrated with the oxygen content in the environment during a two-minute open-circuit status between the battery mode and sensor mode, allowing diffusion to re-supply from the environment the oxygen that was consumed during battery mode.



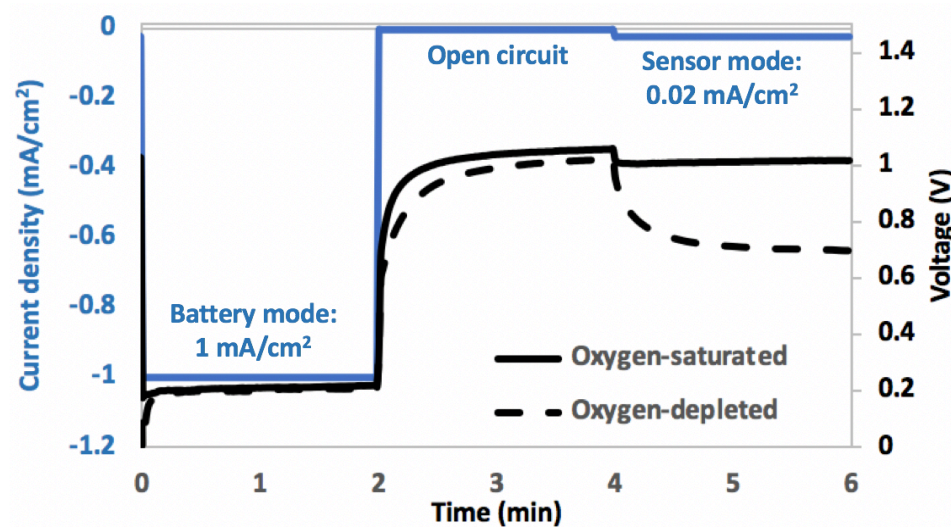


Figure 47. The sensor is discharged at varying current densities. The blue line is the discharge current density of the sensor. The dashed black line is the output voltage in an oxygen-depleted sample electrolyte, while the solid black line is the output voltage in an oxygen-saturated sample electrolyte.

### 5.2.3 Measurement test circuit of the sensor

Fig. 48 shows the measurement test circuit for the sensor. The dashed box represents a simple DC equivalent circuit of the sensor. The resistance  $r$  denotes the internal resistance of the sensor, which is composed of the polarization resistance, electrolyte resistance and connection resistance of the cell. The sensor is interfaced with an external test circuit for drawing a controlled current from the sensor. The output voltage of the sensor varies with the discharge current and reactions on the electrodes; the function of the test circuit is to impose a current waveform such as notionally illustrated in Figure 47 onto the sensor, to allow extraction of the oxygen concentration in the sensor electrolyte.

The test circuit contains two DACs and two op-amps with negative feedback for controlling the discharge current with sufficient precision. The op-amp with a negative feedback resistor also functions as a transimpedance amplifier that converts the discharge current into a voltage, which can be expressed by:

$$V_3 = V_1 + I \cdot R$$

where  $V_3$  represents the output voltage of the transimpedance amplifier, and  $V_1$ ,  $I$ ,  $R$  denote the regulated voltage, output current of the sensor, and feedback resistance of the transimpedance amplifier, respectively. The output of this op-amp will also sink current to balance the current discharged from the sensor.

The circuit provides a regulated voltage between the two terminals of the sensors and the current flowing through the sensor is converted to voltage signals by the transimpedance amplifier and read out by the ADC. The voltage between the sensor terminals is controlled and maintained by the DAC and op-amps, and can be modulated by a microcontroller to reach the desired discharging current. The output voltage of the sensor is read by the microcontroller after the current stabilizes at the designed value, and further filtered to analyze the oxygen concentration in the environment. In addition, when a closed loop circuit is formed at the sensor terminals, the discharge current drawn from the sensor in battery mode can be potentially used to power external devices.

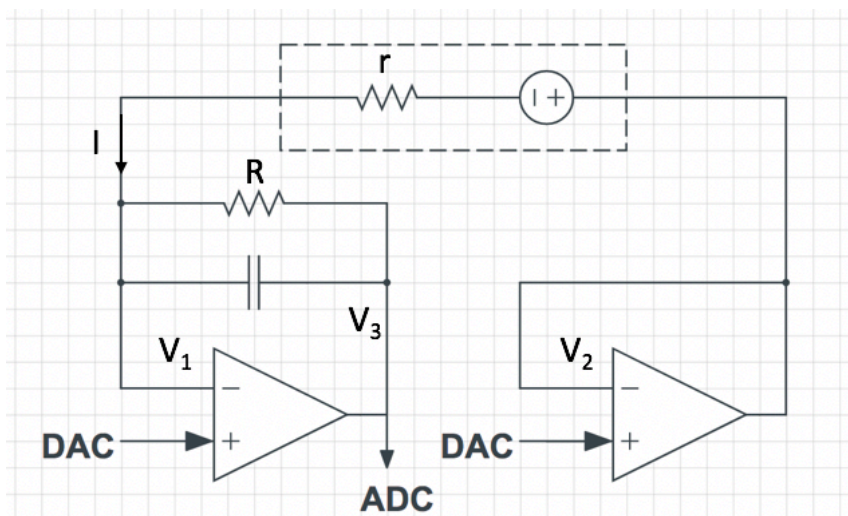


Figure 48. the test circuit of the sensor. The DC equivalence of the sensor is inside the dashed box. The external test circuit draws a controlled current from the sensor.

### 5.3 Characterization and testing

#### 5.3.1 Electrochemical analysis of the sensor

To evaluate the possible reactions on the cathode, potentials between Mg and Mo electrodes and potentials of individual electrodes were investigated using galvanodynamic measurements at a scan rate of  $0.01 \text{ mA/cm}^2 \cdot \text{s}$ . Figure 49 shows the cell potential and individual electrode potentials vs. reference electrode (Ag/AgCl) as a function of discharge current density. The cell voltage change is mainly attributed to the characteristics of current dependence of the cathodic reaction. Specifically, the Mo electrode potential exhibits a significant decrease at a current density up to  $0.45 \text{ mA/cm}^2$  and then switches to a slower decrease, which dominates the decrease in potential difference between Mg and Mo electrodes. The cathode reactions give a potential between  $-0.2 \text{ V}$  and  $-1 \text{ V}$  vs. Ag/ AgCl reference electrode at a low discharge current

density up to  $0.4 \text{ mA/cm}^2$ . The potential is less than the oxygen reduction potential ( $0.179 \text{ V vs. Ag/AgCl}$ ) and higher than the hydrogen evolution potential ( $-1.05 \text{ V vs. Ag/AgCl}$ ), suggesting that both types of reactions could take place. The cathodic reaction shifts completely to hydrogen evolution ( $-(1.2-1.3) \text{ V vs. Ag/AgCl}$ ) at a higher current density with a significant increase of the amount of visible hydrogen bubbles at the cathode. The significant decrease in voltage at low current density therefore mainly results from a change of the cathodic reaction from oxygen reduction to hydrogen evolution.

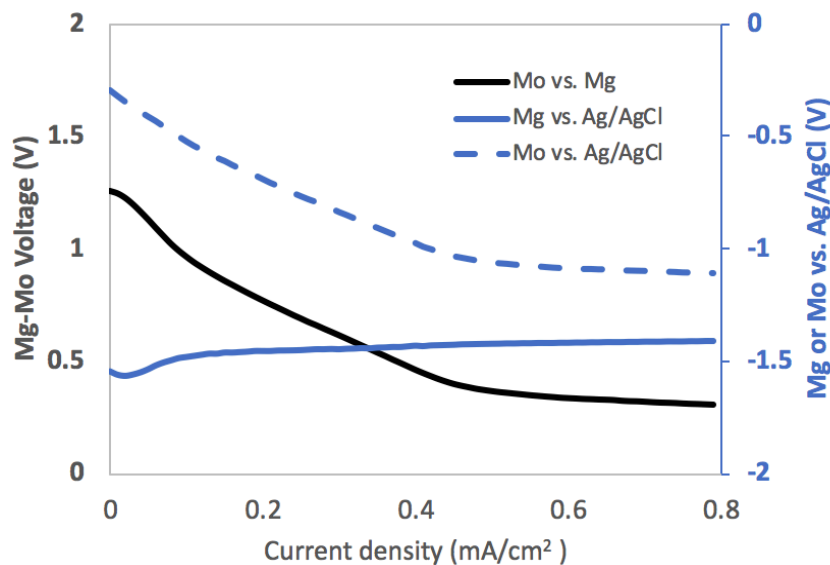


Figure 49. Galvanodynamic measurements of the Mg-Mo pair and the individual electrodes at a scan rate of  $0.01 \text{ mA/cm}^2 \cdot \text{s}$ .

### 5.3.2 Sensor testing method

Fig. 50 shows an example using the test method described in section 5.2.3. The sensor operates in battery mode for 5 minutes, followed by 2 minutes of open circuit to allow oxygen concentration on cathode surface to equilibrate with external environment. The

cell voltage is then measured at a low discharge current density to evaluate the oxygen concentration in the environment.

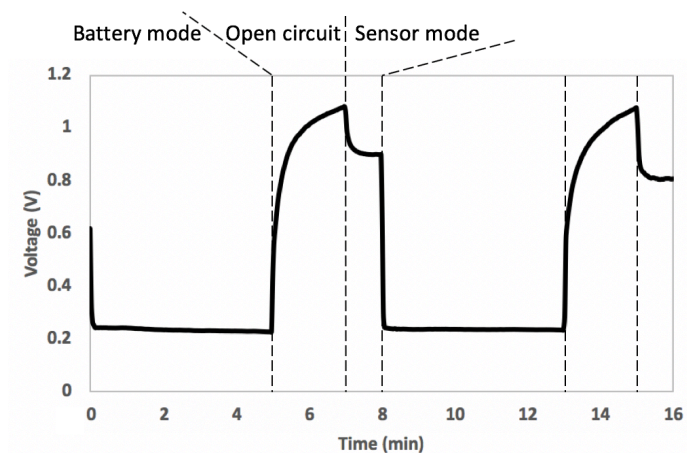
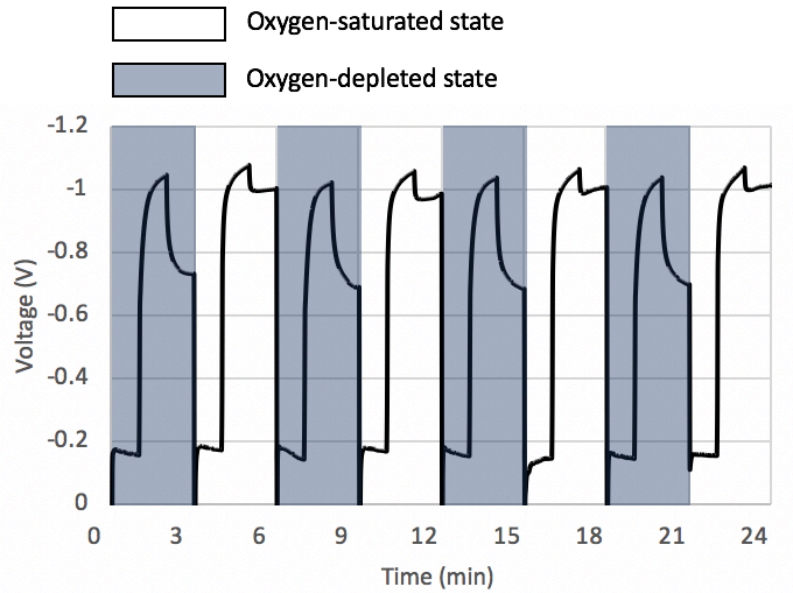


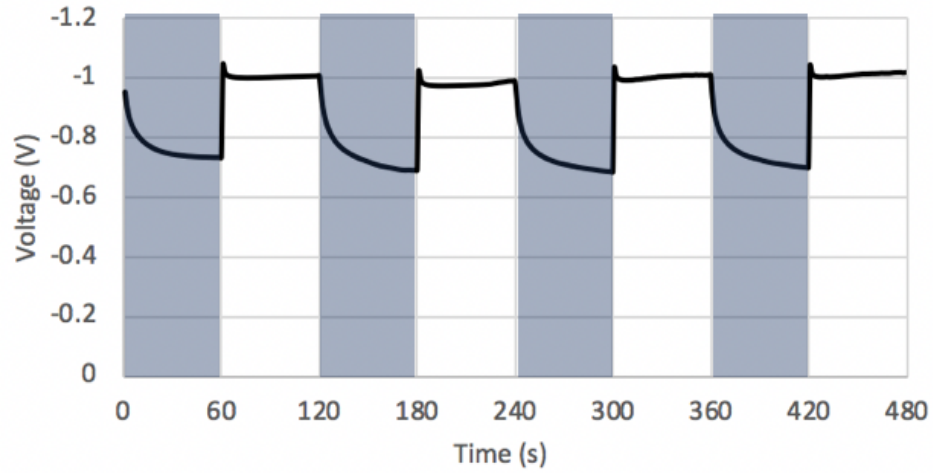
Figure 50. An example of a PCL-supported Mg-Mo electrochemical couple supported on PLA being subjected to the test method described in section 5.2.3. The output voltage of the electrochemical couple is measured as a function of time. During battery mode, a current of 1 mA/cm<sup>2</sup> is being drawn from the couple. During open circuit mode, no current is drawn from the couple. During sensor mode, a current of 0.02 mA/cm<sup>2</sup> is drawn from the couple. In sensor mode, the output voltage is representative of the electrolyte oxygen concentration. The process is then repeated to understand the time history of oxygen concentration in the environment.

Benchtop testing of the sensor was performed in a 0.1 M NaCl solution in both oxygen-saturated and oxygen-depleted states. Fig. 51 and Fig. 52 demonstrate the testing result of a Mg-Mo sensor using two test methods. Specifically, in Fig. 51, the discharge current is alternated between battery mode and sensor mode during each measurement, as shown in Fig. 51(a); while in Fig. 52, the discharge current density is set to a constant value of 0.02 mA/cm<sup>2</sup>. Fig. 51(b) extracts the output voltage in sensor mode from Fig. 51(a), which is

used to evaluate the oxygen concentration. In Fig. 52, the first measurement in oxygen-saturated state shows approximately a 50% drift (marked by the green circle), and the output voltage takes a longer time to stabilize in later measurements of the oxygen-depleted state. Neither of these effects are observed in Fig. 51(b). It is speculated that the initial drift is caused by insufficient polarization of the sensor before the first measurement, and the increasing stabilization time is due to the changing electrode properties (i.e. less available reactions sites, etc.) during the measurement, potentially due to accumulating  $\text{Mg}(\text{OH})_2$  buildup on the anode. Therefore, alternating between battery mode and sensor mode is preferred compared to a constant discharge measurement.



(a)



(b)

Figure 51. Testing result of the sensor in both oxygen-saturated and oxygen-depleted state. (a) The discharge current is alternated between battery mode and sensor mode during each measurement; (b) output voltage in sensor mode extracted from (a). Stable operation is observed.

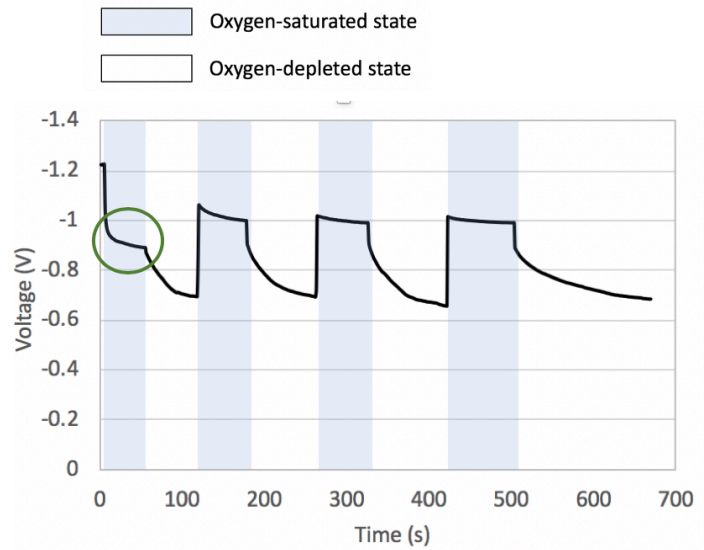
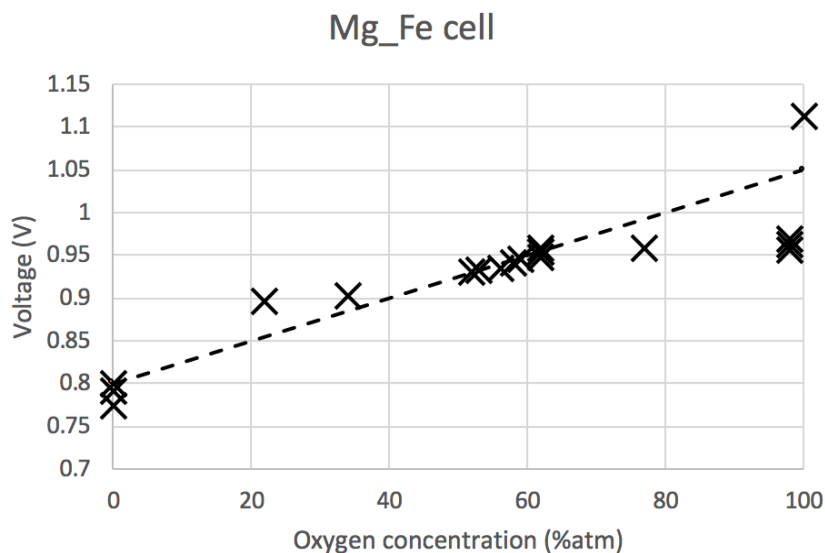


Figure 52. Output voltage of the sensor at constant discharge current (i.e., sensor mode only) in both oxygen-saturated and oxygen-depleted states. Sensor drift is observed.

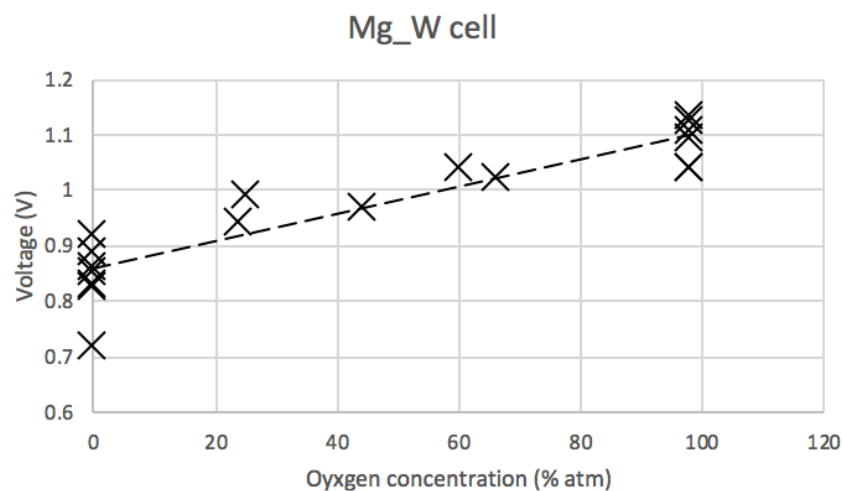
### 5.3.3 Comparison of Mg-Fe, Mg-W and Mg-Mo galvanic pairs

Sensors with Mg anodes and different cathode materials (i.e. Fe, W and Mo) are tested and compared using a 0.1 M NaCl solution, where the oxygen concentration was tuned by the addition of sodium sulfite ( $\text{Na}_2\text{SO}_3$ ) and calibrated to a commercial  $\text{O}_2$  probe (Microx TX3, PreSens). The output voltage of the biodegradable sensors is cross-referenced to the commercial probe to evaluate their performance. Fig. 53 shows that the sensitivities of Mg-Fe, Mg-W and Mg-Mo sensors in the physiologically relevant concentrations (i.e. 0-60 atm% oxygen) are approximately 2.5 mV/atm.%, 2.2 mV/atm.% and 5 mV/atm.%, respectively. While the sensors all demonstrated linearity across a range of physiologically relevant concentrations, the Mg-Mo cell shows the highest sensitivity over the physiologically relevant range, and good linearity, with a correlation coefficient exceeding 0.97.

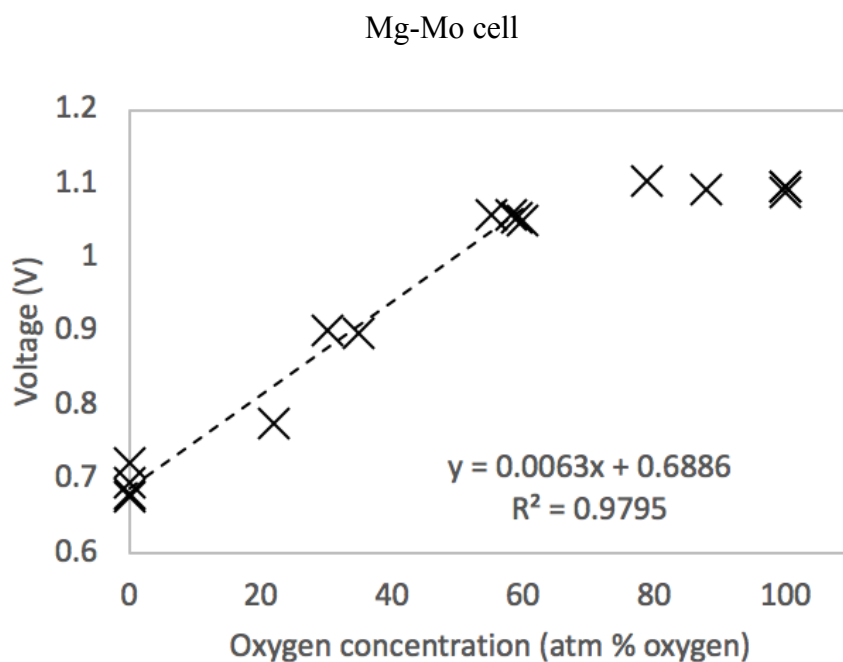


(a)





(b)

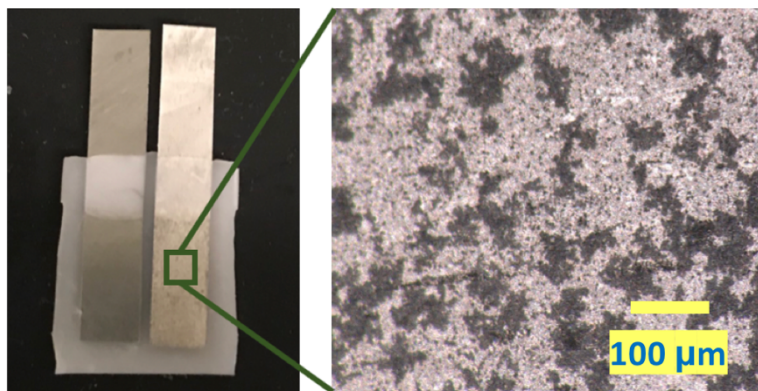


(c)

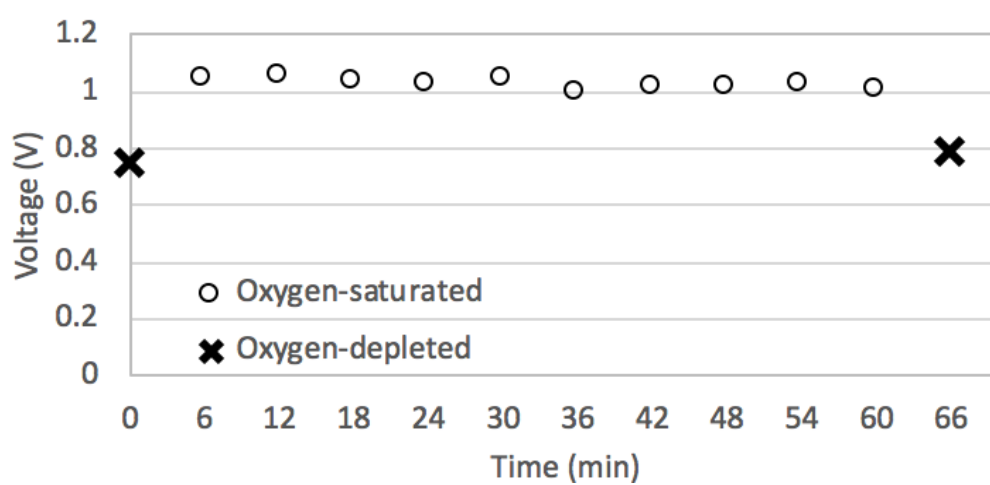
Figure 53. Response characterization of (a) Mg-Fe, (b) Mg-W and (c) Mg-Mo sensors at a discharge current density of 0.02 mA/cm<sup>2</sup>. At each measurement point, sensor interrogation protocol followed the waveforms of Fig. 50 (battery mode, open circuit mode, sensor mode).

#### 5.3.4 Characterization of a Mg-Mo oxygen Sensor

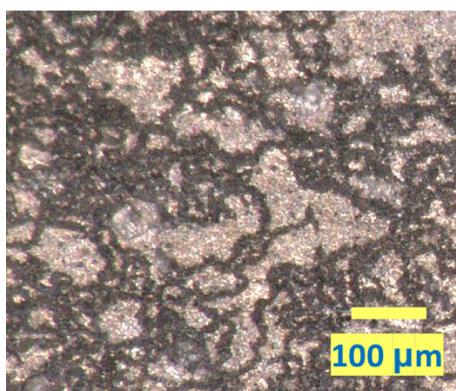
The Mg-Mo galvanic couple is chosen as the anode/cathode pair due to its high sensitivity over the physiologically relevant oxygen range as demonstrated in the previous section. The Mg and Mo electrode pair is molded into a 200  $\mu\text{m}$ -thick PLA substrate with a lamination press. Fig. 54 (a) shows an optical image of the sensor. The simple structure of the sensor facilitates miniaturization. The total size of this sensor is 15 mm  $\times$  18 mm  $\times$  0.2 mm. Mg foil with 0.45cm<sup>2</sup> active area and thickness of 45  $\mu\text{m}$  is placed in the sensor, and the anode cathode spacing is 1 mm. The size of the sensor can be further minimized by reducing the active area of the electrodes. The optical image of the Mg surface shows the cotton-like oxide deposits arising from repeated formation and breakdown of the passivating layer after an hour of operation. Fig. 54(b) shows that the output voltage fluctuation in an hour is approximately 10 %, possibly due to the area changes of exposed Mg. When the sensor is only discharged at a low current density of 0.02 mA/cm<sup>2</sup> for an hour, a higher density of hydroxides can be observed on the surface of the sensor (as shown in Fig. 54(c)), which further suggests that a high discharge current density is important for maintaining a relatively constant anode surface area.



(a)



(b)

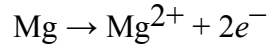


(c)

Figure 54. (a) Optical image of the sensor and cotton-like deposits observed on anode after an hour of testing; (b) The stability results of biodegradable oxygen sensor by measuring output voltage at a full-oxygen state 10 times sequentially. Sensor sensitivity is validated by measuring in oxygen depleted state before and after the stability test. (c) Optical image of sensor surface after discharge for an hour at a low current density of 0.02 mA/cm<sup>2</sup>.

## 5.4 Device modeling

As describe in section 5.2, the sensor involves three reactions. The oxidation of Mg takes place on the anode surface:



The cathodic reaction of the electrochemical cell is given by:



Electron transfer reactions are commonly described by the Butler-Volmer equation. Since there is a limited amount of oxygen dissolved in the electrolyte, the oxygen reduction reaction is controlled by the mass transfer of oxygen from the bulk electrolyte to the electrode surface. The dependence of electrical current on the electrode potential can be described by a generalized form of the Butler-Volmer equation, which is applicable to the mass transfer-influenced conditions:

$$j = j_0 \left\{ \frac{c_o(0, t)}{c_o^*} \exp \left[ \frac{\alpha_a z F \eta}{RT} \right] - \frac{c_r(0, t)}{c_r^*} \exp \left[ -\frac{\alpha_c z F \eta}{RT} \right] \right\}$$

Where  $j$  is the electrode current density,  $j_0$  is the exchange current density,  $T$  is absolute temperature,  $z$  is number of electrons involved in the electrode reaction,  $F$  is the Faraday constant,  $R$  is the universal gas constant,  $a_c$  is the cathodic charge transfer coefficient,  $a_a$  is the anodic charge transfer coefficient,  $\eta$  is the activation overpotential,  $c_o$  and  $c_r$  refer to the concentration of the species to be oxidized and to be reduced, respectively, and  $c(0,t)$  is the time-dependent concentration at the electrode surface. The activation overpotential is defined by:

$$\eta = E - E_{eq}$$

where  $E$  is the electrode potential and  $E_{eq}$  is the equilibrium potential derived from Nernst equation:

$$E_{eq} = E^0 - \frac{RT}{zF} \ln \frac{a_{Red}}{a_{Ox}}$$

Where  $E^0$  is the standard half-cell potential and  $a$  is the chemical activity for the relevant species.

In the cathodic hydrogen evolution reaction and Mg oxidation reaction on the anode, the electrode reaction is controlled by electrical charge transfer at the electrode. Excluding the mass transfer effect, the relationship between the electrical current and potential can be described by:

$$j = j_0 \cdot \left\{ \exp \left[ \frac{\alpha_a z F \eta}{RT} \right] - \exp \left[ -\frac{\alpha_c z F \eta}{RT} \right] \right\}$$

The rate of oxygen concentration change in a volume is given by flow and diffusion into and out of that volume along with any generation or consumption of oxygen inside the control volume:

$$\frac{\partial c}{\partial t} + \nabla \cdot \mathbf{j} = R,$$

where  $c$  is the oxygen concentration which will be subject to mass transfer, and  $R$  is a net volumetric source for  $c$ . For example,  $R > 0$  means that a chemical reaction is creating more of the species, and  $R < 0$  means that a chemical reaction is consuming the species;  $\mathbf{j}$  is the total flux. We assume there is only one source of flux in this situation which arises due to diffusion. The flux of oxygen is proportional to the local concentration gradient:

$$\mathbf{j}_{\text{diff}} = -D\nabla c$$

The coupled electrochemical and diffusion processes of the sensor are modeled using COMSOL Multiphysics Transport of Diluted Species (tds) module and Secondary Current Distribution (siec) module. A 2D model (as shown in Fig. 55) was built to reduce the computational complexity assuming the current, voltage and oxygen distribution are uniform in the  $z$  direction (along the electrodes). A series of simulations were carried out by fixing the current density to be 0.04 mA/cm<sup>2</sup> and varying the initial oxygen concentration (0.001 mol/m<sup>3</sup>, 0.07 mol/m<sup>3</sup>, 0.14 mol/m<sup>3</sup>, 0.21 mol/m<sup>3</sup>, 0.28 mol/m<sup>3</sup>). The

electrolyte pH is set to be 7. The concentration of  $\text{Mg}^{2+}$  is set to be a relatively small value ( $10^{-8} \text{ mol/m}^3$ ) to account for the diluted dissolved  $\text{Mg}^{2+}$  in the external liquid. When oxygen concentration drops below  $10^{-30} \text{ mol/m}^3$ , we fix it to  $10^{-30} \text{ mol/m}^3$  to avoid the numerical error of evaluating the real logarithm of a negative number. The hydrogen evolution exchange current density on Mo surface is approximately  $10^{-3} \text{ A/m}^2$ [102]. The exchange current density of Mg oxidation and oxygen reduction are set to be  $1 \text{ A/m}^2$  and  $2.68 \times 10^{-4} \text{ A/m}^2$ , respectively, and the oxygen diffusion coefficient in the electrolyte is set to be  $3 \times 10^{-9} \text{ m}^2/\text{s}$  to better fit the experimental result. These fitted values are in similar ranges with values found in literature[103][104][76].

The dependence of oxygen concentration as a function of cell voltage at  $T = 200 \text{ s}$  is plotted in Fig. 56. The increase in oxygen concentration increases the output voltage of the cell. An oxygen sensor was tested at a sensor-mode discharge current density of  $0.04 \text{ mA/cm}^2$  and output voltages at  $T = 60 \text{ s}$  were recorded and compared with the simulated results, as shown in Fig 56.

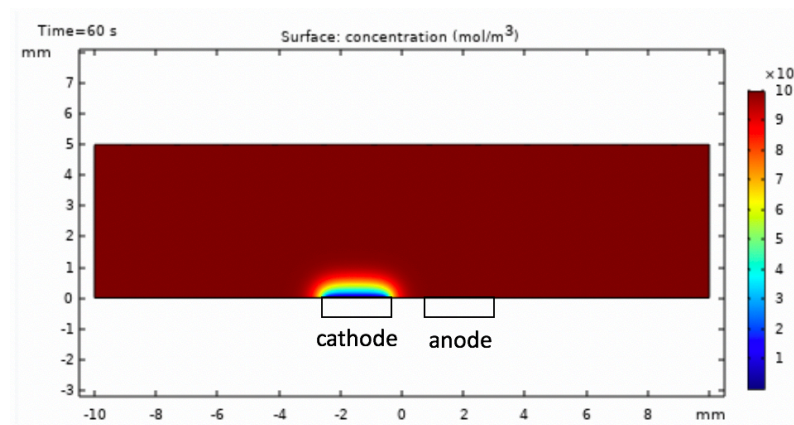


Figure 55. A 2D map of the oxygen distribution in the electrolyte after applying a current to the electrodes using COMSOL Multiphysics.

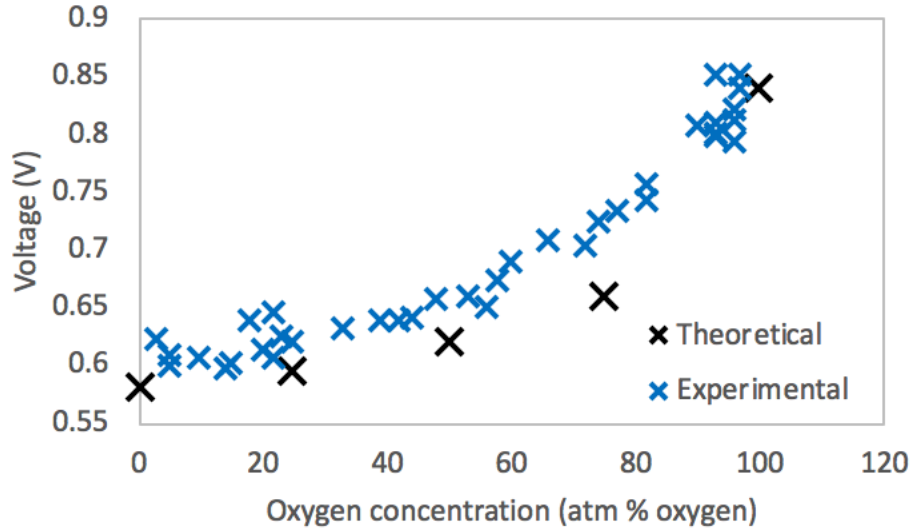


Figure 56. Simulated and experimental results of the dependence of oxygen concentration as a function of cell voltage. The experimental cell was an Mg-Mo couple discharged in sensor mode at a current density of  $0.04 \text{ mA/cm}^2$ . At each measurement point, sensor interrogation protocol followed the waveforms of Fig. 50 (battery mode, open circuit mode, sensor mode).

Although exact correspondence between the simulated and experimental values were not obtained, the model captures the functional form of the observed behavior well. This gives us confidence that the proposed method of operation of the biodegradable oxygen sensor is plausible, and allows for a more full exploration of the design space of this class of sensors in future work.

## 5.5 Summary

Biodegradable oxygen sensors are designed and fabricated, and their performance is examined in this chapter. Three cathode materials (Mg-Mo, Mg-Fe, Mg-W) are fabricated on a biodegradable substrate and their performance is compared. In order to



maintain stable operation, the device works in alternating battery mode and sensor mode. High current density in battery mode induces breakdown of the  $\text{Mg}(\text{OH})_2$  film on the anode surface, which can ensure a relatively constant anode surface area. The output voltage of the cell in sensor mode is then measured to evaluate the oxygen concentration. The Mg-Mo galvanic pair embossed onto a PLA substrate was found to have the highest sensitivity to oxygen concentration over the physiologically relevant range of interest. This design features easy fabrication of a biodegradable oxygen sensor, thus providing a simplified strategy for transient monitoring of the environment and biological process, such as environmental spills, algal tides and wound healing.

## CHAPTER 6 CONCLUSIONS AND FUTURE WORK

### 6.1 Summary of Conducted Research

In accordance to the objective of this thesis, a microfabricated Clark-type oxygen sensor was fabricated and characterized (Chapter 2). The sensor demonstrated a good oxygen response and linearity over a range of physiologically relevant oxygen concentrations. This device was integrated with a customized potentiostat circuit and a microcontroller with data process and wireless transmission capability, enabling monitoring oxygen tension in biomedical-related applications over semi-chronic time periods.

To demonstrate the feasibility of the prototype oxygen sensing system for *in vivo* applications, sensors with smaller planar footprint were fabricated to adapt to small animal models (Chapter 3). Oxygen levels in mouse gluteus muscle and zebrafish trunk muscle were further investigated to validate the sensor's ability to test oxygen level *in vivo*.

To further develop a biodegradable oxygen sensor along with a transient energy source to support the design of completely biodegradable oxygen sensing systems, a biodegradable Mg-Fe battery (Chapter 4) and a transient galvanic oxygen sensor (Chapter 5) were designed, fabricated and characterized. The battery achieved a constant discharge profile in the presence of varying external aqueous conditions, enabling compact, stable-performing cells with a designable functional life span. The transient sensor can potentially measure physiological oxygen tension in a transient, harmless manner in the body, while simultaneously acting as a potential energy source for additional devices.

## 6.2 Suggestions for Future Research

### 6.2.1 Clark-type Oxygen Sensor and *In Vivo* Study

Chapter 2 and 3 demonstrated a Clark-type oxygen sensor and its application *in vivo*. Linear sweep voltammetry was used to overcome the potential fluctuations of the gold reference electrode and eliminate the quantitative errors in data collection due to simple inaccuracies in the reference potential. The remaining difficulties in tissue can be overcome by using higher scan rates for LSV measurement to limit the oxygen depleted region in the membrane and the thin saline layer behind it. Therefore, the sensor may be calibrated *in vitro* before use and the calibration will be valid for conditions *in vivo*. However, for long-term implantable applications, biofouling is an important limiting factor in terms of measurement accuracy and deployment longevity. Further improvement involves surface modifications, surface coatings, and their interactions with the tissue. Establishing standardized procedures for testing toxicity and tissue integration of these surfaces and coatings will guide the future strategies in developing biofouling-resistant oxygen sensors.

Previously reported tissue  $\text{PO}_2$  values have shown substantial variation. In the subcutaneous tissue of rabbits, the  $\text{PO}_2$  was 20–25 mmHg [105] and in human subcutaneous tissue 40 mmHg. In the skin flaps of pigs, the average tissue  $\text{PO}_2$  varied between 21 and 53 mmHg and  $\text{PCO}_2$  between 41 and 53 mmHg [106]. Even if the same model are used among the different laboratories, median  $\text{PO}_2$  values vary widely, thus requiring several comparative studies [8]. Our study contributed data points to the oxygen

levels in zebrafish trunk muscle and mouse gluteus muscle. However, inherent problems might exist in using these animal models, such as:

(1) Insertion of the sensor disturbs the equilibrium in the local environment, including the microcirculation, leading to compromised tissue perfusion and decreased oxygenation.

(2) Damage to the tissue causes platelets to aggregate within minutes or even seconds, and release a variety of substances to prevent exsanguination, which also widens the area that perfusion is disturbed. Since oxygen sensor is in close contact with tissue surface, the coagulation would block the penetration of oxygen into the cell from the tissue.

(3) Since the animal is brought into sedation right before sensor insertion, it might take a few minutes for its life condition to stabilize. For instance, both decreasing respiratory frequency and lowering body temperature could cause tissue oxygen tension to decrease.

Problems might be caused by these phenomena inherent in inserting electrodes into anesthetized animal models, no matter how well the electrodes are engineered. Histogram statistical analysis might be needed to analyze such results. Further improvements include using larger animal models and eliminating the need of anesthetization or using the sensors in non-invasive applications where the sensors are placed on organ or tissue surfaces. Specifically, the overall size of the sensor would be negligible compared to the size of tissue, removing the need for sedation and reducing the side effect of tissue damage induced by invasive measurement.

### 6.2.2 Lifetime of the biodegradable devices

Chapter 4 and chapter 5 discussed the design, fabrication and characterization of a biodegradable battery and a biodegradable oxygen sensor. As the transient nature of the biodegradable would suggest, the devices can physically degrade after they are implanted in the body. However, the viability of the transient devices during degradation is still unclear. The devices should maintain their functionality during some portion of its degradation lifespan for use in various applications in vivo.

Ideally, the device should disappear immediately after the device finishes its job and is no longer functionally required. However, in reality, such a case is likely impossible because the degradation of materials will likely have to undergo some unstable stage before disappearing. Further, for short functional lifetime applications, it is possible that a correspondingly short degradation lifetime would result in local toxicity due to the environment surrounding the sensor changing rapidly. Therefore, the desired performance for a degradable device would be long functional lifetime, with a degradation lifetime as short as possible while remaining biocompatible.

In chapter 4, we have shown that the functional lifetime of the biodegradable battery is mainly limited by the NaCl efflux, if a sufficient amount of Mg is incorporated in the battery. In our design, the battery has a solid electrolyte volume of  $12\text{ mm} \times 10\text{ mm} \times 2\text{ mm}$ , which contains 0.48g NaCl/PCL composite (93.75 wt% NaCl). The leaching of NaCl from the battery is hindered by the polymeric binder in the NaCl/PCL composite and PCL membrane. Increased ratios of PCL in the NaCl/PCL composite and an increased thickness of the passivation film would result in longer functional lifetime, at

the cost of increasing the mass transfer resistances of water and prolonging the activation time for the battery. Fortunately, in some applications, an equilibration time for the battery to absorb water and stabilize is acceptable. Therefore, longer functional lifetimes and a reasonable activation time of this battery can be obtained by engineering the ration of PCL in the NaCl/PCL composite and the thickness of PCL passivation layer. Other parameters such as molecular weight of PCL can also be used to engineer the transport of NaCl and water.

The lifetime of the biodegradable sensor described in Chapter 5 is typically limited by depletion of the Mg anode. It is therefore necessary to control and extend the discharge lifetime of the Mg-Mo galvanic pair. The functional lifetime of the sensor may potentially be improved by incorporating a more compact cross section (i.e., narrow and thin) so that the length of the Mg anode would be at least 1-2 orders of magnitude larger than its cross-sectional dimensions. In this manner, only a small cross-section of Mg at one end of the anode would be exposed to the electrolyte, discharge of the device would proceed along the length of the anode.

After improving the functional lifetime of the devices, it is important to tailor the degradable lifetime of the devices while maintaining biocompatibility. This balance between those factors can be predefined *in vitro* before the implantation process. Some parameters such as thickness, molecular weight of PCL and PLA and volume of the metals can be used to engineer the functional lifetime as well as degradation lifetime. In addition, surface-erodible biodegradable polymers such as polyorthoester, polyanhydride,

polyglycerol sebacate, etc. can be used instead of PCL or PLA to precisely control and engineer the device's functional lifetime and degradation behavior.

### 6.2.3 Biodegradable Oxygen Sensor

The transient oxygen sensors may have application in transient monitoring of the environment. For instance, the biodegradable oxygen sensor can be used to help improve the characterization of soil respiration. Typically, oxygen sensors can be buried at various depths to monitor oxygen depletion over time, which is then used to predict soil respiration rates. The amount of soil respiration is controlled by several factors. Various factors such as temperature, moisture, pressure and level of oxygen in the soil are intertwined and can and produce extremely disparate rates of respiration.

The oxygen sensors respond to absolute oxygen concentration but are generally calibrated to yield relative gas concentration. For testing in the body where moisture, temperature and pH are relatively consistent, the sensor output can be compared to calibration prior to the test and yield a relatively accurate result. However, in environmental applications where pressure and temperature fluctuate, the sensor output fluctuates even under consistent oxygen levels. If these effects are not accounted for, it produces an apparent change in the calculated relative oxygen concentration.

There are two ways which can potentially solve this problem. First, the sensors can be better engineered so that it is only sensitive to oxygen concentration in the environment. Either the encapsulation layer of the sensor selectively allows oxygen signals to get into

the sensor, or the sensor was engineered such that all other environmental factors are kept consistent. For instance, the sensors can be equipped with an internal thermistor and a small resistance heater located on the back side of the sensor. The heaters are designed to warm the sensor to a temperature slightly above ambient in order to keep the temperature consistent for all tests. The temperature response of the sensors can therefore be minimized. Alternatively, a differential measurement, in which the signal from one sensor that is impervious to oxygen is subtracted from the signal from a second sensor that is oxygen-sensitive and one sensor is not, with all other sensor features identical, could remove the common mode errors of the environment such as temperature. Expanding this concept, instead of pre-test calibration, the oxygen sensors can be calibrated to a real-time two-point calibration system. For example, three sensors buried to different depths could be used to test the oxygen concentration in the soil. The oxygen level close to the deepest and uppermost sensors are set to be 0 and 160 torr, respectively, and the middle depth sensor is buried to the depth of interest. Other parameters such as pH and temperature are consistent for all three sensors, allowing relative oxygen concentration in the soil to be calculated by comparing the sensor output of three sensors.



## APPENDIX 1

Control program main.c

```
#include "RF_Toggle_LED_Demo.h"
```

```
#include "cc430f6137.h"
```

```
#include "hal_uart.h"
```

```
#include "hal_lcd.h"
```

```
#define PACKET_LEN      (0x04)      // PACKET_LEN <= 61
```

```
#define RSSI_IDX        (PACKET_LEN+1) // Index of appended RSSI
```

```
#define CRC_LQI_IDX     (PACKET_LEN+2) // Index of appended LQI, checksum
```

```
#define CRC_OK          (BIT7)      // CRC_OK bit
```

```
#define PATABLE_VAL     (0xC4)      // 0XC4-- 10 dBm;
```

```
        // 0X50-- 0 dBm;
```

```
        // 0X2D-- -6 dBm;
```

```
        // 0X26-- -12dBm;
```

```
        // 0x05-- -30dBm;
```

```
        // 0xc0-- max
```

```
#define LED_DIR         PJDIR
```

```
#define LED_OUT         PJOUT
```

```
#define LED_SEL         PJSEL
```

```
#define LED_BIT         0
```

```
#define LED_ON()        LED_OUT|=(1<<LED_BIT)
```

```
#define LED_OFF()       LED_OUT&=~(1<<LED_BIT)
```

```
#define LED_BIT1        0x01
```

```
#define LED1_ON()       LED_OUT|=(1<<LED_BIT1)
```

```
#define LED1_OFF()      LED_OUT&=~(1<<LED_BIT1)
```

```
#define LED_BIT2        0x02
```

```
#define LED2_ON()       LED_OUT|=(1<<LED_BIT2)
```

```
#define LED2_OFF()      LED_OUT&=~(1<<LED_BIT2)
```

```
#define LED_BIT3        0x03
```

```
#define LED3_ON()       LED_OUT|=(1<<LED_BIT3)
```

```
#define LED3_OFF()      LED_OUT&=~(1<<LED_BIT3)
```

```
#define BUTTON_BIT0     0
```

```
#define BUTTON_BIT1     0x01
```

```
#define BUTTON_BIT2     0x02
```

```
#define BUTTON_BIT3     0x03
```

```
#define BUTTON_DIR      P2DIR
```

```
#define BUTTON_OUT      P2OUT
```

```

#define BUTTON_REN    P2REN
#define BUTTON_IN     P2IN

// #define CPU_F      ((double)1000000)
// #define delayms(x)  _delay_cycles((long)(CPU_F*(double)x/1000.0))
// #define delayss(x)  _delay_cycles((long)(CPU_F*(double)x))

void delayms(unsigned int n)
{
    unsigned int i, j;
    for(i=0; i<n; i++)
    {
        for(j=0; j<1023; j++) _NOP();
    }
}

void delayss(unsigned int n){
    unsigned int i;
    for(i=0; i<n; i++) delayms(1023);
}

void showN(unsigned int x){
    HalLcdPrint7SegDigit((unsigned char)('0' + x / 10), 4);
    HalLcdPrint7SegDigit((unsigned char)('0' + x % 10), 5);
}

extern RF_SETTINGS rfSettings;

unsigned char packetReceived;
unsigned char packetTransmit;

unsigned char RxBuffer[64];
unsigned char RxBufferLength = 0;
unsigned char TxBuffer[5] = {PACKET_LEN, 0x00, 0x00, 0x00, 0x00};

static unsigned char string[2] = "wt";

unsigned char transmitting = 0;
unsigned char receiving = 0;

unsigned char status = 0;
unsigned char ins = 0;
unsigned int time = 0;

```

```

void main( void )
{
    WDTCTL = WDTPW + WDTNORM;

    SetVCore(2);

    ResetRadioCore();
    InitRadio();
    InitButtonLeds();
    HalUartInit();
    HalLcdInit();

    _EINT();
    ReceiveOn();
    receiving = 1;

    unsigned char flag;

    while (1)
    {
        __bis_SR_register( LPM3_bits + GIE );
        __no_operation();
        switch(__even_in_range(status,6))
        {
            case 2:
                ReceiveOff();
                receiving = 0;
                for(flag = 0x00; flag < 0x20; flag++)
                {
                    Transmit( (unsigned char*)TxBuffer,sizeof TxBuffer);
                    transmitting = 1;
                    __bis_SR_register( LPM3_bits + GIE );
                }
                if(!transmitting)
                {
                    ReceiveOn();
                    receiving = 1;
                }
                break;
            case 4:
                HalUartTxString(string, sizeof string);
                ReceiveOn();
                receiving = 1;

```

```

        break;
    case 6:
        ReceiveOn();
        receiving = 1;
        break;
    }

}

}

}

void InitButtonLeds(void)
{

    P2OUT = 0xFF;
    P2DIR = 0xFF;
    P2REN = 0xFF;
    P2IE = 0xFF;

    // Set up LEDs
    LED_OUT = 0;
    LED_DIR = 0xFF;
}

void InitRadio(void)
{
    // Set the High-Power Mode Request Enable bit so LPM3 can be entered
    // with active radio enabled
    PMMCTL0_H = 0xA5;
    PMMCTL0_L |= PMMHPMRE_L;
    PMMCTL0_H = 0x00;

    WriteRfSettings(&rfSettings);

    WriteSinglePATable(PATABLE_VAL);
}

void Transmit(unsigned char *buffer, unsigned char length)
{
    LED_OUT^=(1<<LED_BIT);
    RF1AIES |= BIT9;
    RF1AIFG &= ~BIT9;           // Clear pending interrupts
    RF1AIE |= BIT9;             // Enable TX end-of-packet interrupt

    WriteBurstReg(RF_TXFIFOWR, buffer, length);
}

```

```

    Strobe( RF_STX );          // Strobe STX
}

void ReceiveOn(void)
{
// LED_ON();
RF1AIES |= BIT9;              // Falling edge of RFIFG9
RF1AIFG &= ~BIT9;             // Clear a pending interrupt
RF1AIE |= BIT9;               // Enable the interrupt

// Radio is in IDLE following a TX, so strobe SRX to enter Receive Mode
Strobe( RF_SRX );
}

void ReceiveOff(void)
{
// LED_OFF();
RF1AIE &= ~BIT9;              // Disable RX interrupts
RF1AIFG &= ~BIT9;             // Clear pending IFG

// It is possible that ReceiveOff is called while radio is receiving a packet.
// Therefore, it is necessary to flush the RX FIFO after issuing IDLE strobe
// such that the RXFIFO is empty prior to receiving a packet.
Strobe( RF_SIDLE );
Strobe( RF_SFRX );
}

#pragma vector=CC1101_VECTOR
__interrupt void CC1101_ISR(void)
{
    switch(__even_in_range(RF1AIV,32))    // Prioritizing Radio Core Interrupt
    {
        case 0: break;                  // No RF core interrupt pending
        case 2: break;                  // RFIFG0
        case 4: break;                  // RFIFG1
        case 6: break;                  // RFIFG2
        case 8: break;                  // RFIFG3
        case 10: break;                  // RFIFG4
        case 12: break;                  // RFIFG5
        case 14: break;                  // RFIFG6
        case 16: break;                  // RFIFG7
        case 18: break;                  // RFIFG8
        case 20: break;                  // RFIFG9
    }
}

```

```

if(receiving)          // RX end of packet
{
    RF1AIE &= ~BIT9;          // Disable RX interrupts
    // Read the length byte from the FIFO
    RxBufferLength = ReadSingleReg( RXBYTES );
    ReadBurstReg(RF_RXFIFORD, RxBuffer, RxBufferLength);

    // Stop here to see contents of RxBuffer
    __no_operation();

    // Check the CRC results
    if(RxBuffer[CRC_LQI_IDX] & CRC_OK)
    {
        switch(__even_in_range(status,6))
        {
            case 0:
            case 2:
            case 6:
                HalLcdPrint7SegDigit((unsigned char*)RxBuffer[PACKET_LEN-3],0);
                HalLcdPrint7SegDigit((unsigned char*)RxBuffer[PACKET_LEN-2],1);

                if(RxBuffer[PACKET_LEN-3] == 'o' && RxBuffer[PACKET_LEN-2]
== 'k')
                    status = 4;
                else status = 6;
                break;
            case 4:
                LED_OUT ^= (1<<LED_BIT2);
                string[0] = RxBuffer[PACKET_LEN-1];
                string[1] = RxBuffer[PACKET_LEN];
                break;
        }
    }
}

else if(transmitting)    // TX end of packet
{
    RF1AIE &= ~BIT9;          // Disable TX end-of-packet interrupt
    LED_OFF();              // Turn off LED after Transmit
    transmitting = 0;
}

```

```

        else while(1);           // trap
        break;
    case 22: break;               // RFIFG10
    case 24: break;               // RFIFG11
    case 26: break;               // RFIFG12
    case 28: break;               // RFIFG13
    case 30: break;               // RFIFG14
    case 32: break;               // RFIFG15
}
__bic_SR_register_on_exit(LPM3_bits);
}

```

```

#pragma vector=PORT2_VECTOR
__interrupt void PORT2_ISR(void)
{
    switch(__even_in_range(P2IV, 16))
    {
        case 0: break;
        case 2:
            status = 2;
            __bic_SR_register_on_exit(LPM3_bits);
            break;           // P1.0 IFG
        case 4:
            if(ins != 6) break;
            if(time == 24){
                TxBuffer[3] = 0;
                TxBuffer[4] = 23;
            } else TxBuffer[4]--;
            time++;
            showN(time);
            break;           // P1.1 IFG
        case 6:
            if(ins != 6) break;
            if(time == 25){
                TxBuffer[3] = 1;
                TxBuffer[4] = 0;
            } else TxBuffer[4]++;
            time--;
            showN(time);
            break;           // P1.2 IFG
        case 8:
            switch(__even_in_range(ins,6))
            {

```

```

    case 0:
    case 6:
        ins = 2;
        TxBuffer[1] = 's';
        TxBuffer[2] = 't';
        HalLcdPrint7SegDigit((unsigned char*)'S',4);
        HalLcdPrint7SegDigit((unsigned char*)'T',5);
        break;
    case 2:
        ins = 4;
        TxBuffer[1] = 'e';
        TxBuffer[2] = 'd';
        HalLcdPrint7SegDigit((unsigned char*)'E',4);
        HalLcdPrint7SegDigit((unsigned char*)'D',5);
        break;
    case 4:
        ins = 6;
        time = 24;
        TxBuffer[1] = 'd';
        TxBuffer[2] = 's';
        TxBuffer[3] = 0x01;
        TxBuffer[4] = 0x00;
        HalLcdPrint7SegDigit((unsigned char*)'2',4);
        HalLcdPrint7SegDigit((unsigned char*)'4',5);
        break;
    }
    break;// P1.3 IFG
    case 10: break;           // P1.4 IFG
    case 12: break;           // P1.5 IFG
    case 14: break;           // P1.6 IFG
    case 16: break;
}
P2IFG = 0x00;
}
#pragma vector=USCI_A0_VECTOR
__interrupt void USCI_A0_ISR(void)
{
    switch(__even_in_range(UCA0IV,4))
    {
        case 0:break;         // Vector 0 - no interrupt
        case 2:                // Vector 2 - RXIFG
            while (!(UCA0IFG&UCTXIFG));    // USCI_A0 TX buffer ready?
            UCA0TXBUF = UCA0RXBUF;         // TX -> RXed character
            break;
    }
}

```



```

    case 4:break;                // Vector 4 - TXIFG
    default: break;
    }
}

```

Sensor program main.c  
//On 5137

```
#include "RF_Toggle_LED_Demo.h"
```

```

#define PACKET_LEN    (0x04)    // PACKET_LEN <= 61
#define RSSI_IDX      (PACKET_LEN+1) // Index of appended RSSI
#define CRC_LQI_IDX   (PACKET_LEN+2) // Index of appended LQI, checksum
#define CRC_OK        (BIT7)     // CRC_OK bit

```

```

#define PATABLE_VAL    (0x50)    // 0XC4-- 10 dBm;
                                // 0X50-- 0 dBm;
                                // 0X2D-- -6 dBm;
                                // 0X26-- -12dBm;
                                // 0x05-- -30dBm;
                                // 0xc0-- max

```

```

#define BIT14          BITE
#define DACCS0         P2OUT &= ~BIT7
#define DACCS1         P2OUT |= BIT7
#define DIN0           P2OUT &= ~BIT4
#define DIN1           P2OUT |= BIT4
#define SCLK0          P2OUT &= ~BIT6
#define SCLK1          P2OUT |= BIT6

```

```

#define CPU_F ((double)1000000)
#define delay_us(x) __delay_cycles((long)(CPU_F*(double)x/1000000.0))
#define delay_ms(x) delay_us(1000*x)
void delayms(unsigned int n)
{
    unsigned int i, j;
    for(i=0;i<n;i++)
    {
        for(j=0;j<200;j++) _NOP();
    }
}

```

```

void delayss(unsigned int n){
    unsigned int i;

```

```

        for(i=0;i<n;i++) delayms(1000);
    }

    unsigned char wor=0;

    extern RF_SETTINGS rfSettings;

    unsigned char packetReceived;
    unsigned char packetTransmit;

    unsigned char RxBuffer[64];
    unsigned char RxBufferLength = 0;
    unsigned char TxBuffer[5] = {PACKET_LEN, 'R', 'D', 0x00, 0x00};

    unsigned char transmitting = 0;
    unsigned char receiving = 0;
    unsigned char start = 0;
    unsigned char sleep = 0;
    unsigned char day = 0x01;
    unsigned char hour = 0x00;

    unsigned long current = 0;
    unsigned long current1 = 0;
    unsigned int voltage = 0x0000;
    unsigned int voltageST = 0x8100;
    volatile unsigned int results[4];

    void main( void )

    {
        // Stop watchdog timer to prevent time out reset
        WDTCTL = WDTPW + WDTHOLD;

        SetVCore(2);
        ResetRadioCore();
        InitRadio();

        unsigned char flag;
        for(flag=0x00;flag<0x1A;flag++){
            Transmit( (unsigned char*)TxBuffer,sizeof TxBuffer);
            transmitting = 1;
            __bis_SR_register(LPM3_bits + GIE);
        }
    }

```

```

WriteSingleReg(WOREVT1, 0x87); //0x87
WriteSingleReg(WOREVT0, 0x6B); //0x6B
// WORCTRL.EVENT1 = 7 => T_EVENT1 = ~1.5 msec
WriteSingleReg(MCSM2, 0x00); //0x00
// WORCTRL.WOR_RES = 0 (EVENT0 = 34667, RX_TIME = 6)
// => RX timeout = 34667 * 0.0563 = ~1.96 msec
WriteSingleReg(WORCTRL, (7 << 4) | 0); //1110000
WriteSingleReg(IOCFG1, 0x29); // GDO1 = RF_RDY 29 1F

DACPort_Init();
InitADC();

wor = 1;
while (1){
    Strobe(RF_SWOR);
    RF1AIE |= BIT14;
    __bis_SR_register(LPM3_bits + GIE);
    __no_operation();

    if(sleep){
        wor = 0;
        RF1AIE &= ~(BIT1+BIT14);

        UCSCTL3 |= SELREF__REFOCLK;
        UCSCTL4 = SELA__REFOCLK + SELM__DCOCLKDIV +
        SELS__DCOCLKDIV;
        UCSCTL6 |= XT2OFF + XT1OFF;

        do{
            UCSCTL7 &= ~(XT2OFFG + XT1LFOFFG + XT1HFOFFG + DCOFFG);
            // Clear XT2,XT1,DCO fault flags
            SFRIFG1 &= ~OFIFG; // Clear fault flags
        }while (SFRIFG1&OFIFG);

        RTCCTL01 |= RTCAIE + RTCHOLD + RTCMODE;

        RTCYEAR = 0x0000; // Year = 0x2010
        RTCMON = 0x01; // 1
        RTCDAY = 0x01; // 1
        RTCDOW = day; //day; // 0
        RTCHOUR = hour; //hour; // 0
        RTCMIN = 0x00; // 0
        RTCSEC = 0x00; // 0
    }
}

```

```

// RTCADOWDAY = 0x2;           // RTC Day of week alarm = 0x2
RTCADAY = 0x01;                // RTC Day Alarm = 0x20
RTCADOW = 0x02|0x80;
RTCAHOUR = 0x00;               // RTC Hour Alarm
RTCAMIN = 0x00;               // RTC Minute Alarm

unsigned int temp = (2 - RTCDOW) * 24 - RTCHOUR;
TxBuffer[1] = '0' + temp / 10;
TxBuffer[2] = '0' + temp % 10;

delayss(3);

unsigned char i;
for(i=0;i<5;i++){
    Transmit( (unsigned char*)TxBuffer,sizeof TxBuffer);
    transmitting = 1;
    __bis_SR_register(LPM3_bits + GIE);
}

RF1AIE = 0x00;
P2IE = 0x00;

RTCCTL01 &= ~(RTCHOLD);       // Start RTC calendar mode

__bis_SR_register(LPM3_bits + GIE); // Enter LPM3 mode with interrupts
__no_operation();
}
else if(start)
{
    wor = 0;
    RF1AIE &= ~(BIT1+BIT14);

    delayss(3);

    voltage = voltageST;
    P5DIR |= 0x01;
    P5OUT |= 0x01;
    DAC_Ser(voltage);

    unsigned char i;
    for(i=0;i<10;i++)
    {
        Transmit( (unsigned char*)TxBuffer,sizeof TxBuffer);
        transmitting = 1;
    }
}

```

```

        __bis_SR_register(LPM3_bits + GIE);
        __no_operation();
    }
    for(i=0;i<0x0fff;i++)
    {
        //set voltage and read current
        current = 0;

        DAC_Ser(voltage);
        voltage = voltage + 0x0400;//0x006E;

        P2SEL |= BIT5 + BIT0 + BIT1 + BIT2 + BIT3;
        ADC12CTL0 = ADC12ON+ADC12MSC+ADC12SHT0_2;    // Turn
on ADC12, set sampling time
        ADC12CTL1 = ADC12SHP +ADC12CONSEQ_1;
        ADC12MCTL0 = ADC12SREF_2 + ADC12INCH_0;    // Use
sampling timer
        ADC12MCTL1 = ADC12SREF_2 + ADC12INCH_1;
        ADC12MCTL2 = ADC12SREF_2 + ADC12INCH_2;
        ADC12MCTL3 = ADC12SREF_2 + ADC12INCH_3+ADC12EOS;
        ADC12IE = 0x08;

        ADC12CTL0 |= ADC12ENC + ADC12SC;

        __bis_SR_register(LPM4_bits + GIE);    // LPM0, ADC12_ISR will force
exit

        current = current;
        TxBuffer[3] = (current>>8) & 0xff;
        TxBuffer[4] = current & 0xff;

        //    unsigned int j;
        //    for(j=0;j<3;j++){
            RF1AIE &= ~(BIT1+BIT14);
            Transmit( (unsigned char*)TxBuffer,sizeof TxBuffer);
            transmitting = 1;
            __bis_SR_register(LPM3_bits + GIE);
            __no_operation();
        //    }

        RF1AIE |= BIT14;
        ReceiveOn();
        receiving = 1;

```

```

        __bis_SR_register(LPM3_bits + GIE);
        __no_operation();
        RF1AIE &= ~BIT14;
        ReceiveOff();
        receiving = 0;
    }
    DAC_Ser(voltageST);
    delayss(1);

//    wor = 1;
    PMMCTL0 = PMMPW | PMMSWBOR;

}
}

}

```

```

void InitRadio(void)

```

```

{
    // Set the High-Power Mode Request Enable bit so LPM3 can be entered
    // with active radio enabled
    PMMCTL0_H = 0xA5;
    PMMCTL0_L |= PMMHPMRE_L;
    PMMCTL0_H = 0x00;

    WriteRfSettings(&rfSettings);

    WriteSinglePATable(PATABLE_VAL);
}

```

```

void InitADC(void)

```

```

{
    P2SEL |= BIT5 + BIT0 + BIT1 + BIT2 + BIT3;
    ADC12CTL0 = ADC12ON+ADC12MSC+ADC12SHT0_2;    // Turn on
ADC12, set sampling time
    ADC12CTL1 = ADC12SHP +ADC12CONSEQ_1;
    ADC12MCTL0 = ADC12SREF_2 + ADC12INCH_0;      // Use
sampling timer
    ADC12MCTL1 = ADC12SREF_2 + ADC12INCH_1;
    ADC12MCTL2 = ADC12SREF_2 + ADC12INCH_2;
    ADC12MCTL3 = ADC12SREF_2 + ADC12INCH_3+ADC12EOS;
}

```

```

//      ADC12MCTL0 = ADC12SREF_2;          // Vr+ = VeREF+ (ext) and Vr-
=AVss
      //ADC12IE = 0x10;
}

void DACPort_Init(void)
{
    P2DIR |= BIT4 + BIT6 + BIT7;
    P2OUT  = 0xFF;
}

void Transmit(unsigned char *buffer, unsigned char length)
{
    RF1AIES |= BIT9;
    RF1AIFG &= ~BIT9;          // Clear pending interrupts
    RF1AIE |= BIT9;           // Enable TX end-of-packet interrupt

    WriteBurstReg(RF_TXFIFOWR, buffer, length);

    Strobe( RF_STX );          // Strobe STX
}

void ReceiveOn(void)
{
    RF1AIES |= BIT9;           // Falling edge of RFIFG9
    RF1AIFG &= ~BIT9;         // Clear a pending interrupt
    RF1AIE |= BIT9;           // Enable the interrupt

    // Radio is in IDLE following a TX, so strobe SRX to enter Receive Mode
    Strobe( RF_SRX );
}

void ReceiveOff(void)
{
    RF1AIE &= ~BIT9;          // Disable RX interrupts
    RF1AIFG &= ~BIT9;         // Clear pending IFG

    // It is possible that ReceiveOff is called while radio is receiving a packet.
    // Therefore, it is necessary to flush the RX FIFO after issuing IDLE strobe
    // such that the RXFIFO is empty prior to receiving a packet.
    Strobe( RF_SIDLE );
    Strobe( RF_SFRX );
}

```

```

void DAC_Ser(unsigned int data)
{
    unsigned char i;
    unsigned int control;
    unsigned int DACDATA2;
    control = 0x1000;

    DACCS0;
    SCLK0;

    for (i=0;i<8;i++)
    {
        DACDATA2=control&0x8000;
        if(DACDATA2>>15)
            DIN1;
        else
            DIN0;
        SCLK1;
        control<<=1;
        SCLK0;
    }
    for (i=0;i<16;i++)
    {
        DACDATA2=data&0x8000;
        if(DACDATA2>>15)
            DIN1;
        else
            DIN0;
        SCLK1;
        data<<=1;
        SCLK0;
    }
    delay_us(10);
    DACCS1;
    SCLK0;
}

#pragma vector=CC1101_VECTOR
__interrupt void CC1101_ISR(void)
{
    switch(__even_in_range(RF1AIV,32))    // Prioritizing Radio Core Interrupt
    {
        case 0: break;                // No RF core interrupt pending
        case 2: break;                // RFIFG0
    }
}

```



```

case 4:                                // GDO1 = LNA_PD signal
if(wor){
    RF1AIE &= ~(BIT1+BIT9);

    Strobe(RF_SWOR);
}

if(receiving){
    RF1AIE &= ~(BIT1+BIT9);
    __bic_SR_register_on_exit(LPM3_bits);
}
break;
case 6: break;                        // RFIFG2
case 8: break;                        // RFIFG3
case 10: break;                       // RFIFG4
case 12: break;                      // RFIFG5
case 14: break;                      // RFIFG6
case 16: break;                      // RFIFG7
case 18: break;                      // RFIFG8
case 20:                             // RFIFG9
    if(wor || receiving)              // RX end of packet
    {
//-----
//    LED_OUT |= (1<<LED_BIT);
//-----
        RF1AIE &= ~(BIT1+BIT9);

        // Read the length byte from the FIFO
        RxBufferLength = ReadSingleReg( RXBYTES );
        ReadBurstReg(RF_RXFIFORD, RxBuffer, RxBufferLength);

        if(RxBuffer[CRC_LQI_IDX] & CRC_OK)    // Check checksum bit
        {
            if(RxBuffer[PACKET_LEN-3] == 's' && RxBuffer[PACKET_LEN-2] == 't') {

                start = 1;
                sleep = 0;
                TxBuffer[1] = 'o';
                TxBuffer[2] = 'k';

            }
            else if(RxBuffer[PACKET_LEN-3] == 'd' && RxBuffer[PACKET_LEN-2] == 's')
        {
            day = RxBuffer[PACKET_LEN-1];                // 0

```

```

        hour = RxBuffer[PACKET_LEN];           // 0
        sleep = 1;
        start = 0;
    }
    else if(RxBuffer[PACKET_LEN-3] == 'e' && RxBuffer[PACKET_LEN-2] == 'd')
    {
        DAC_Ser(voltageST);
        delayss(1);
        PMMCTL0 = PMMPW | PMMSWBOR;
    }
}
}
else if(transmitting)    // TX end of packet
{
    RF1AIE &= ~BIT9;      // Disable TX end-of-packet interrupt
    transmitting = 0;
}
else while(1);           // trap
__bic_SR_register_on_exit(LPM3_bits);
break;
case 22: break;          // RFIFG10
case 24: break;          // RFIFG11
case 26: break;          // RFIFG12
case 28: break;          // RFIFG13
case 30:                 // WOR_EVENT0
    if(wor){
//    RF1AIFG &= ~(BIT9 + BIT1);
    RF1AIES |= BIT9;      // Falling edge of RFIFG9
    RF1AIFG &= ~BIT9;     // Clear a pending interrupt
//    RF1AIE |= BIT9;      // Enable the interrupt
    RF1AIE |= BIT9 + BIT1;
//-----

//-----

        Strobe( RF_SRX );}
        if(receiving) __bic_SR_register_on_exit(LPM3_bits);
        break;
    case 32: break;       // RFIFG15
    }
// __bic_SR_register_on_exit(LPM3_bits);
}

#pragma vector = ADC12_VECTOR

```

```

__interrupt void ADC12_ISR(void)
{
    switch(__even_in_range(ADC12IV,34))
    {
        case 0: break;           // Vector 0: No interrupt
        case 2: break;           // Vector 2: ADC overflow
        case 4: break;           // Vector 4: ADC timing overflow
        case 6:
            current = ADC12MEM0;
            __bic_SR_register_on_exit(LPM4_bits);
            break;               // Vector 6: ADC12IFG0

        case 8: break;           // Vector 8: ADC12IFG1
        case 10: break;          // Vector 10: ADC12IFG2
        case 12:
            current1 = current + ADC12MEM0;
            current1 = current + ADC12MEM1;
            current1 = current + ADC12MEM2;
            current1 = current + ADC12MEM3;

            current1 = current / 4; // Move results, IFG is cleared
            __bic_SR_register_on_exit(LPM4_bits);
            break; // Exit active CPU, SET BREAKPOINT HERE

        case 14: break;          // Vector 14: ADC12IFG4
        case 16: break;          // Vector 16: ADC12IFG5
        case 18: break;          // Vector 18: ADC12IFG6
        case 20: break;          // Vector 20: ADC12IFG7
        case 22: break;          // Vector 22: ADC12IFG8
        case 24: break;          // Vector 24: ADC12IFG9
        case 26: break;          // Vector 26: ADC12IFG10
        case 28: break;          // Vector 28: ADC12IFG11
        case 30: break;          // Vector 30: ADC12IFG12
        case 32: break;          // Vector 32: ADC12IFG13
        case 34: break;          // Vector 34: ADC12IFG14
        default: break;
    }
}

#pragma vector=RTC_VECTOR
__interrupt void RTC_ISR(void)
{
    switch(__even_in_range(RTCIV,16))
    {
        case RTC_NONE: break;
    }
}

```

```

case RTC_RTCDYIFG: break;
case RTC_RTCTEVIFG: break;
case RTC_RTCAIFG:           // RTCAIFG
    PMMCTL0 = PMMPW | PMMSWBOR;
    break;
case RTC_RT0PSIFG: break;
case RTC_RT1PSIFG: break;
case 12: break;           // Reserved
case 14: break;           // Reserved
case 16: break;           // Reserved
default: break;
}
}

```

## APPENDIX 2

```
#include "cc430x513x.h"
#include "hal_pmm.h"
#include "hal_uart.h"
#include <msp430.h>

/*****
 * Function Definition
 */

void InitButtonLeds(void);
void delayms(unsigned int n);
void InitADC(void);
void AdcShutDown(void);

#define BIT14      BITE
#define DACCS0      P2OUT &= ~BIT7
#define DACCS1      P2OUT |= BIT7
#define DIN0        P2OUT &= ~BIT4
#define DIN1        P2OUT |= BIT4
#define SCLK0       P2OUT &= ~BIT6
#define SCLK1       P2OUT |= BIT6

#define CPU_F ((double)1000000)
#define delay_us(x) __delay_cycles((long)(CPU_F*(double)x/1000000.0))
#define delay_ms(x) delay_us(1000*x)
void delayms(unsigned int n)
{
    unsigned int i, j;
    for(i=0;i<n;i++)
    {
        for(j=0;j<200;j++) _NOP();
    }
}

void delayss(unsigned int n){
    unsigned int i;
    for(i=0;i<n;i++) delayms(1000);
}

unsigned char start = 0;
```

```

unsigned long current = 0;
unsigned int voltage = 0x0000;
unsigned int voltageST = 0x5E00;//0x6700;
unsigned int voltageIncrease = 0x0200; //0x01E0;
unsigned char x = 0x00;

void main( void ){
    WDTCTL = WDTPW + WDTXOLD;
    SetVCore(2);

    DACPort_Init();
    InitADC();
    HalUartInit();
    __EINT();
    start = 0;
    unsigned char result[4] = "wtwt";
    __bis_SR_register(LPM4_bits + GIE);

    while (1){
        __bis_SR_register(LPM0_bits + GIE);
        __no_operation();

        if(start){
            result[0] = 'd';
            result[1] = 't';
            // voltage = voltageST;
            P5DIR |= 0x01;
            P5OUT |= 0x01;
            DAC_Ser(voltage);

            unsigned char i;
            for(voltage = voltageST; voltage < 0xffff - voltageIncrease; voltage =
voltage + voltageIncrease){
                current = 0;

                DAC_Ser(voltage);
                // voltage = voltage + 0x01E0;//0x006E;

                P2SEL |= BIT5 + BIT0 + BIT1 + BIT2;
                ADC12CTL0 = ADC12ON+ADC12MSC+ADC12SHT0_2;
            // Turn on ADC12, set sampling time
                ADC12CTL1 = ADC12SHP + ADC12CONSEQ_1;
                ADC12MCTL0 = ADC12SREF_2 + ADC12INCH_0;
            // Use sampling timer

```

```

        ADC12MCTL1 = ADC12SREF_2 + ADC12INCH_1;
        ADC12MCTL2 = ADC12SREF_2 + ADC12INCH_2 +
ADC12EOS;

        ADC12IE = 0x04;

        ADC12CTL0 |= ADC12ENC + ADC12SC;

        __bis_SR_register(LPM4_bits + GIE);    // LPM0, ADC12_ISR
will force exit

        current = current / 3;
        result[2] = (unsigned char*)((current>>8) & 0xff);
        result[3] = (unsigned char*)(current & 0xff);
        HalUartTxString(result, sizeof result);
        delayss(1);
    }
    DAC_Ser(voltageST);
    delayss(1);
    P5OUT |= 0x00;
    DAC_Ser(0x0000);
    PMMCTL0 = PMMPW | PMMSWBOR;
}
}

}

void InitADC(void)
{
    P2SEL |= BIT5 + BIT0 + BIT1 + BIT2;
    ADC12CTL0 = ADC12ON+ADC12MSC+ADC12SHT0_2;    // Turn on
ADC12, set sampling time
    ADC12CTL1 = ADC12SHP + ADC12CONSEQ_1;
    ADC12MCTL0 = ADC12SREF_2 + ADC12INCH_0;    // Use
sampling timer
    ADC12MCTL1 = ADC12SREF_2 + ADC12INCH_1;
    ADC12MCTL2 = ADC12SREF_2 + ADC12INCH_2 + ADC12EOS;

    //    ADC12MCTL0 = ADC12SREF_2;    // Vr+ = VeREF+ (ext) and Vr-
=AVss
    //ADC12IE = 0x10;
}

```

```

void DACPort_Init(void)
{
    P2DIR |= BIT4 + BIT6 + BIT7;
    P2OUT = 0xFF;
}

void DAC_Ser(unsigned int data)
{
    unsigned char i;
    unsigned int control;
    unsigned int DACDATA2;
    control = 0x1000;

    DACCS0;
    SCLK0;

    for (i=0;i<8;i++)
    {
        DACDATA2=control&0x8000;
        if(DACDATA2>>15)
            DIN1;
        else
            DIN0;
        SCLK1;
        control<<=1;
        SCLK0;
    }
    for (i=0;i<16;i++)
    {
        DACDATA2=data&0x8000;
        if(DACDATA2>>15)
            DIN1;
        else
            DIN0;
        SCLK1;
        data<<=1;
        SCLK0;
    }
    delay_us(10);
    DACCS1;
    SCLK0;
}

#pragma vector = ADC12_VECTOR

```



```

__interrupt void ADC12_ISR(void)
{
    switch(__even_in_range(ADC12IV,34))
    {
        case 0: break;                // Vector 0: No interrupt
        case 2: break;                // Vector 2: ADC overflow
        case 4: break;                // Vector 4: ADC timing overflow
        case 6:
            current = ADC12MEM0;
            __bic_SR_register_on_exit(LPM4_bits);
            break;                    // Vector 6: ADC12IFG0

        case 8: break;                // Vector 8: ADC12IFG1
        case 10:
            current = current + ADC12MEM0;
            current = current + ADC12MEM1;
            current = current + ADC12MEM2;
            __bic_SR_register_on_exit(LPM4_bits);
            break;                    // Vector 10: ADC12IFG2
        case 12: break; // Exit active CPU, SET BREAKPOINT HERE
        case 14: break;                // Vector 14: ADC12IFG4
        case 16: break;                // Vector 16: ADC12IFG5
        case 18: break;                // Vector 18: ADC12IFG6
        case 20: break;                // Vector 20: ADC12IFG7
        case 22: break;                // Vector 22: ADC12IFG8
        case 24: break;                // Vector 24: ADC12IFG9
        case 26: break;                // Vector 26: ADC12IFG10
        case 28: break;                // Vector 28: ADC12IFG11
        case 30: break;                // Vector 30: ADC12IFG12
        case 32: break;                // Vector 32: ADC12IFG13
        case 34: break;                // Vector 34: ADC12IFG14
        default: break;
    }
}

#pragma vector=USCI_A0_VECTOR
__interrupt void USCI_A0_ISR(void)
{
    switch(__even_in_range(UCA0IV,4))
    {
        case 0: break;                // Vector 0 - no interrupt
        case 2:                        // Vector 2 - RXIFG
            x = UCA0RXBUF;
            if(x == 's'){

```

```

        start = 1;
    }
    else if(x == 'e'){
        DAC_Ser(voltageST);
//        delayss(1);
        PMMCTL0 = PMMPW | PMMSWBOR;
    }
    __bic_SR_register_on_exit(LPM4_bits);
//    HalLcdPrint7SegDigit(x,3);
//    while (!(UCA0IFG&UCTXIFG));        // USCI_A0 TX buffer ready?
//    UCA0TXBUF = UCA0RXBUF;            // TX -> RXed character
    break;
case 4:break;                        // Vector 4 - TXIFG
default: break;
}
}

```

## BIBLIOGRAPHY

- [1] J. O. C. Dunn, M. G. Mythen, and M. P. Grocott, "Physiology of oxygen transport," *BJA Educ.*, 2016.
- [2] R. N. Pittman, "Oxygen Transport in the Microcirculation and Its Regulation," *Microcirculation*. 2013.
- [3] P. Venditti, L. Di Stefano, and S. Di Meo, "Mitochondrial metabolism of reactive oxygen species," *Mitochondrion*. 2013.
- [4] A. J. Kowaltowski, N. C. de Souza-Pinto, R. F. Castilho, and A. E. Vercesi, "Mitochondria and reactive oxygen species," *Free Radical Biology and Medicine*. 2009.
- [5] P. J. Sheffield, "Measuring tissue oxygen tension: A review," *Undersea and Hyperbaric Medicine*. 1998.
- [6] J. Park, T. Bansal, M. Pinelis, and M. M. Maharbiz, "A microsystem for sensing and patterning oxidative microgradients during cell culture," *Lab Chip*, 2006.
- [7] I. G. Kirkinetzos and C. T. Moraes, "Reactive oxygen species and mitochondrial diseases," *Semin. Cell Dev. Biol.*, 2001.
- [8] A. Carreau, B. El Hafny-Rahbi, A. Matejuk, C. Grillon, and C. Kieda, "Why is the partial oxygen pressure of human tissues a crucial parameter? Small molecules and hypoxia," *J. Cell. Mol. Med.*, 2011.
- [9] B. S. Klosterhoff *et al.*, "Implantable Sensors for Regenerative Medicine," *J. Biomech. Eng.*, vol. 139, no. 2, p. 021009, 2017.
- [10] C. T. Brighton and A. G. Krebs, "Oxygen tension of healing fractures in the rabbit," *J. Bone Joint Surg. Am.*, 1972.
- [11] R. Ramamoorthy, P. K. Dutta, and S. A. Akbar, "Oxygen sensors: Materials, methods, designs and applications," *J. Mater. Sci.*, vol. 38, no. 21, pp. 4271–4282, 2003.
- [12] N. Akmal and J. Lauer, "Electrochemical Oxygen Sensors: Principles and Applications," *Polym. Sensors*, vol. 690, pp. 149–160, 1998.
- [13] R. Bashir, "BioMEMS: State-of-the-art in detection, opportunities and prospects," *Adv. Drug Deliv. Rev.*, vol. 56, no. 11, pp. 1565–1586, 2004.
- [14] K. Gilleo, D. Ph, and E. Llc, "Mems in Medicine," pp. 1–10.
- [15] C. Pang, C. Lee, and K. Y. Suh, "Recent advances in flexible sensors for wearable and implantable devices," *J. Appl. Polym. Sci.*, vol. 130, no. 3, pp. 1429–1441, 2013.
- [16] H. Du and R. Bogue, "MEMS sensors: past, present and future," *Sens. Rev.*, vol. 27, pp. 7–13, 2007.
- [17] A. C. R. Grayson *et al.*, "A BioMEMS review: MEMS technology for physiologically integrated devices," *Proc. IEEE*, vol. 92, no. 1, pp. 6–21, 2004.
- [18] R. A. M. Receveur, F. W. Lindemans, and N. F. De Rooij, "Microsystem technologies for implantable applications," *J. Micromechanics Microengineering*, vol. 17, no. 5, pp. R50–R80, 2007.

- [19] F. G. Zeng, S. Rebscher, W. Harrison, X. Sun, and H. Feng, "Cochlear implants: system design, integration, and evaluation.," *IEEE Rev. Biomed. Eng.*, vol. 1, no. dc, pp. 115–142, 2008.
- [20] and N. A. P. Steichen, Stephanie D., Mary Caldorera-Moore, "A review of current nanoparticle and targeting moieties for the delivery of cancer therapeutics," *Off. J. Eur. Fed. Pharm. Sci.*, vol. 48(3), pp. 416–427, 2013.
- [21] R. R. Jivani, G. J. Lakhtaria, D. D. Patadiya, L. D. Patel, N. P. Jivani, and B. P. Jhala, "Biomedical microelectromechanical systems (BioMEMS): Revolution in drug delivery and analytical techniques," *Saudi Pharm. J.*, vol. 24, no. 1, pp. 1–20, 2014.
- [22] D. J. H. Tng, R. Hu, P. Song, I. Roy, and K. T. Yong, "Approaches and challenges of engineering implantable microelectromechanical systems (MEMS) drug delivery systems for in vitro and in vivo applications," *Micromachines*, vol. 3, no. 4, pp. 615–631, 2012.
- [23] J. Viventi *et al.*, "Flexible, foldable, actively multiplexed, high-density electrode array for mapping brain activity in vivo.," *Nat. Neurosci.*, vol. 14, no. 12, pp. 1599–605, 2011.
- [24] P. J. Rousche, D. S. Pellinen, D. P. Pivin, J. C. Williams, R. J. Vetter, and D. R. Kipke, "Flexible polyimide-based intracortical electrode arrays with bioactive capability," *IEEE Trans. Biomed. Eng.*, vol. 48, no. 3, pp. 361–370, 2001.
- [25] P. J. Chen, S. Saati, R. Varma, M. S. Humayun, and Y. C. Tai, "Wireless intraocular pressure sensing using microfabricated minimally invasive flexible-coiled LC sensor implant," *J. Microelectromechanical Syst.*, vol. 19, no. 4, pp. 721–734, 2010.
- [26] X. Yu, W. Shou, B. K. Mahajan, X. Huang, and H. Pan, "Materials, Processes, and Facile Manufacturing for Bioresorbable Electronics: A Review," *Advanced Materials*. 2018.
- [27] R. W. Korsmeyer, R. Gurny, E. Doelker, P. Buri, and N. A. Peppas, "Mechanisms of solute release from porous hydrophilic polymers," *Int. J. Pharm.*, 1983.
- [28] M. Vert, S. M. Li, G. Spenlehauer, and P. Guerin, "Bioresorbability and biocompatibility of aliphatic polyesters," *J. Mater. Sci. Mater. Med.*, 1992.
- [29] H. K. Makadia and S. J. Siegel, "Poly Lactic-co-Glycolic Acid (PLGA) as biodegradable controlled drug delivery carrier," *Polymers (Basel)*, 2011.
- [30] M. Tsang, A. Armutlulu, A. W. Martinez, S. A. B. Allen, and M. G. Allen, "Biodegradable magnesium/iron batteries with polycaprolactone encapsulation: A microfabricated power source for transient implantable devices," *Microsystems Nanoeng.*, vol. 1, no. August, p. 15024, 2015.
- [31] L. Yin *et al.*, "Materials, designs, and operational characteristics for fully biodegradable primary batteries," *Adv. Mater.*, vol. 26, no. 23, pp. 3879–3884, 2014.
- [32] L. Yin *et al.*, "Dissolvable metals for transient electronics," *Adv. Funct. Mater.*, 2014.
- [33] M. Luo, A. W. Martinez, C. Song, F. Herrault, and M. G. Allen, "A microfabricated wireless RF pressure sensor made completely of biodegradable

- materials,” *J. Microelectromechanical Syst.*, vol. 23, no. 1, pp. 4–13, 2014.
- [34] M. Luo, C. J. Song, F. Herrault, and M. G. Allen, “A microfabricated RF wireless pressure sensor made completely of biodegradable materials,” *Proc. 14th Solid State Sensors, Actuators, Microsystems Work.*, pp. 38–41, 2012.
  - [35] C. M. Boutry, H. Chandralalim, P. Streit, M. Schinhammer, A. C. Hänzi, and C. Hierold, “Characterization of miniaturized RLC resonators made of biodegradable materials for wireless implant applications,” *Sensors Actuators, A Phys.*, vol. 189, pp. 344–355, 2013.
  - [36] A. Heller, “Potentially implantable miniature batteries,” *Anal. Bioanal. Chem.*, vol. 385, no. 3, pp. 469–473, 2006.
  - [37] D. She, M. Tsang, J. K. Kim, and M. G. Allen, “Immobilized[1] She, D., Tsang, M., Kim, J. K., and Allen, M. G., 2015, ‘Immobilized electrolyte biodegradable batteries for implantable MEMS,’ 2015 Transducers - 2015 18th International Conference on Solid-State Sensors, Actuators and Microsystems, TRANSD,” in *2015 Transducers - 2015 18th International Conference on Solid-State Sensors, Actuators and Microsystems, TRANSDUCERS 2015*, 2015, pp. 494–497.
  - [38] M. Tsang, A. Armutlulu, A. W. Martinez, S. A. B. Allen, and M. G. Allen, “Biodegradable magnesium/iron batteries with polycaprolactone encapsulation: A microfabricated power source for transient implantable devices,” *Microsystems Nanoeng.*, 2015.
  - [39] X. Huang *et al.*, “Biodegradable materials for multilayer transient printed circuit boards,” *Adv. Mater.*, 2014.
  - [40] H. Suzuki, A. Hiratsuka, S. Sasaki, and I. Karube, “Problems associated with the thin-film Ag/AgCl reference electrode and a novel structure with improved durability,” *Sensors Actuators B Chem.*, vol. 46, no. 2, pp. 104–113, 1998.
  - [41] H. Suzuki, T. Hirakawa, S. Sasaki, and I. Karube, “An integrated module for sensing  $pO_2$ ,  $pCO_2$ , and pH,” vol. 405, pp. 57–65, 2000.
  - [42] H. Suzuki, T. Hirakawa, I. Watanabe, and Y. Kikuchi, “Determination of blood  $pO_2$  using a micromachined Clark-type oxygen electrode,” *Anal. Chim. Acta*, vol. 431, pp. 249–259, 2001.
  - [43] H. Suzuki, “Microfabrication of chemical sensors and biosensors for environmental monitoring,” vol. 12, no. 1–2, pp. 55–61, 2000.
  - [44] H. Suzuki, H. Ozawa, S. Sasaki, and I. Karube, “Novel thin-film Ag/AgCl anode structure for microfabricated Clark-type oxygen electrodes,” *Sensors Actuators, B Chem.*, vol. 53, no. 3, pp. 140–146, 1998.
  - [45] H. Suzuki, H. Arakawa, and I. Karube, “Fabrication of a sensing module using micromachined biosensors,” *Biosens. Bioelectron.*, vol. 16, no. 9–12, pp. 725–733, 2001.
  - [46] C. C. Wu, H. N. Luk, Y. T. T. Lin, and C. Y. Yuan, “A Clark-type oxygen chip for in situ estimation of the respiratory activity of adhering cells,” *Talanta*, vol. 81, no. 1–2, pp. 228–234, 2010.
  - [47] M. Wittkamp, G.-C. Chemnitz, K. Cammann, M. Rospert, and W. Mokwa, “Silicon thin film sensor for measurement of dissolved oxygen,” *Sensors Actuators B Chem.*, vol. 43, no. 1–3, pp. 40–44, 1997.

- [48] J. Park, Y. K. Pak, and J. J. Pak, "A microfabricated reservoir-type oxygen sensor for measuring the real-time cellular oxygen consumption rate at various conditions," *Sensors Actuators, B Chem.*, vol. 147, no. 1, pp. 263–269, 2010.
- [49] C. C. Wu, T. Yasukawa, H. Shiku, and T. Matsue, "Fabrication of miniature Clark oxygen sensor integrated with microstructure," *Sensors Actuators, B Chem.*, vol. 110, no. 2, pp. 342–349, 2005.
- [50] G. Koley, J. Liu, M. W. Nomani, M. Yim, X. Wen, and T. Y. Hsia, "Miniaturized implantable pressure and oxygen sensors based on polydimethylsiloxane thin films," *Mater. Sci. Eng. C*, vol. 29, no. 3, pp. 685–690, 2009.
- [51] S. Lee, B. L. Ibey, G. L. Coté, and M. V. Pishko, "Measurement of pH and dissolved oxygen within cell culture media using a hydrogel microarray sensor," *Sensors Actuators, B Chem.*, vol. 128, no. 2, pp. 388–398, 2008.
- [52] M. W. Toepke and D. J. Beebe, "PDMS absorption of small molecules and consequences in microfluidic applications," *Lab Chip*, vol. 6, no. 12, p. 1484, 2006.
- [53] N. K. Hiroaki Suzuki, Akio Sugama, "Micromachined Clark oxygen electrode," *Sensors Actuators B Chem.*, vol. 10, no. 2, pp. 91–98, 1993.
- [54] Z. Yang, S. Sasaki, I. Karube, and H. Suzuki, "Fabrication of oxygen electrode arrays and their incorporation into sensors for measuring biochemical oxygen demand," *Anal. Chim. Acta*, vol. 357, no. 1–2, pp. 41–49, 1997.
- [55] H. Suzuki, "Fabrication of an Oxygen Electrode Using Semiconductor Technology," *Anal. Chem.*, vol. 11, no. 26, pp. 1078–1080, 1993.
- [56] A. Niazi and C. J. Anthony, "Development of Oxygen Sensor by Integrating the Low Cost Printed Circuit Board Technology and Solid Electrolyte Membrane," *Proc. Int. Conf. Biomed. Eng. Syst.*, no. 137, pp. 1–7, 2014.
- [57] N. Yamazoe and N. Miura, "Solid-state electrochemical oxygen sensors for operation at room temperature," *Trends Anal. Chem.*, vol. 9, no. 5, pp. 170–175, 1990.
- [58] J. Kim and A. A. Gewirth, "Mechanism of oxygen electroreduction on gold surfaces in basic media," *J. Phys. Chem. B*, 2006.
- [59] D. J. Strike, A. Hengstenberg, M. Quinto, C. Kurzawa, M. Koudelka-Hep, and W. Schuhmann, "Localized visualization of chemical cross-talk in microsensor arrays by using scanning electrochemical microscopy," *Mikrochim. Acta*, 1999.
- [60] J. N. Lee, C. Park, and G. M. Whitesides, "Solvent Compatibility of Poly(dimethylsiloxane)-Based Microfluidic Devices," *Anal. Chem.*, 2003.
- [61] D. She and M. G. Allen, "A micromachined freestanding electrochemical sensor for measuring dissolved oxygen," *J. Microelectromechanical Syst.*, 2019.
- [62] N. N. Rabalais, R. J. Díaz, L. A. Levin, R. E. Turner, D. Gilbert, and J. Zhang, "Dynamics and distribution of natural and human-caused hypoxia," *Biogeosciences*, 2010.
- [63] G. A. Linneweber *et al.*, "Neuronal control of metabolism through nutrient-dependent modulation of tracheal branching," *Cell*, 2014.
- [64] T. K. Hunt, B. Zederfeldt, and T. K. Goldstick, "Oxygen and healing," *Am. J. Surg.*, 1969.
- [65] H. W. Hopf and M. D. Rollins, "Wounds: An overview of the role of oxygen,"

*Antioxidants and Redox Signaling*. 2007.

- [66] K. Jonsson, J. A. Jensen, W. H. Goodson, J. M. West, and T. K. Hunt, "Assessment of perfusion in postoperative patients using tissue oxygen measurements," *Br. J. Surg.*, 1987.
- [67] L. C. CLARK, R. WOLF, D. GRANGER, and Z. TAYLOR, "Continuous recording of blood oxygen tensions by polarography.," *J. Appl. Physiol.*, 1953.
- [68] I. A. Silver, "Some observations on the cerebral cortex with an ultramicro, membrane-covered, oxygen electrode," *Med. Electron. Biol. Eng.*, 1965.
- [69] W. G. Sheridan, R. H. Lowndes, and H. L. Young, "Tissue oxygen tension as a predictor of colonic anastomotic healing," *Dis. Colon Rectum*, 1987.
- [70] J. N. Demas, B. A. DeGraff, and P. B. Coleman, "Oxygen sensors based on luminescence quenching," *Analytical Chemistry*. 1999.
- [71] O. S. Wolfbeis, "Luminescent sensing and imaging of oxygen: Fierce competition to the Clark electrode," *BioEssays*, 2015.
- [72] S. M. Grist, L. Chrostowski, and K. C. Cheung, "Optical oxygen sensors for applications in microfluidic cell culture," *Sensors (Switzerland)*. 2010.
- [73] J. López-Gejo, D. Haigh, and G. Orellana, "Relationship between the microscopic and macroscopic world in optical oxygen sensing: A luminescence lifetime microscopy study," *Langmuir*, 2010.
- [74] S. K. Lee and I. Okura, "Optical sensor for oxygen using a porphyrin-doped sol-gel glass," *Analyst*, 1997.
- [75] S. J. Davis, M. G. Allen, W. J. Kessler, K. R. McManus, M. F. Miller, and P. A. Mulhall, "Diode laser-based sensors for chemical oxygen iodine lasers," in *Gas and Chemical Lasers*, 1996.
- [76] C. Androjna, J. E. Gatica, J. M. Belovich, and K. A. Derwin, "Oxygen diffusion through natural extracellular matrices: Implications for estimating 'critical thickness' values in tendon tissue engineering," *Tissue Eng. - Part A*, 2008.
- [77] P. Marek, J. J. Velasco-Veléz, T. Doll, and G. Sadowski, "Compensation for the influence of temperature and humidity on oxygen diffusion in a reactive polymer matrix," *J. Sensors Sens. Syst.*, 2014.
- [78] C. Z.Z., S. D., W. D.C., A. M., and F. M.J., "Development of a minimally invasive muscle oxygen nanosensor for evaluation of mitochondrial myopathy," *Mol. Genet. Metab.*, 2018.
- [79] M. G. Allen, "Microfabricated implantable wireless microsystems: Permanent and biodegradable implementations," *Proc. IEEE Int. Conf. Micro Electro Mech. Syst.*, pp. 1–4, 2014.
- [80] E. Y. Chow, A. L. Chlebowsky, S. Chakraborty, W. J. Chappell, and P. P. Irazoqui, "Fully wireless implantable cardiovascular pressure monitor integrated with a medical stent," *IEEE Trans. Biomed. Eng.*, vol. 57, no. 6, pp. 1487–1496, 2010.
- [81] D. J. Chew *et al.*, "A Microchannel Neuroprosthesis for Bladder Control After Spinal Cord Injury in Rat," *Sci. Transl. Med.*, vol. 5, no. 210, pp. 210ra155-210ra155, 2013.
- [82] J. P. Dimarco and M. Mower, "Implantable Cardioverter–Defibrillators," pp. 1836–1847, 2003.

- [83] A. Magalski *et al.*, “Continuous ambulatory right heart pressure measurements with an implantable hemodynamic monitor: A multicenter, 12-month follow-up study of patients with chronic heart failure,” *J. Card. Fail.*, vol. 8, no. 2, pp. 63–70, 2002.
- [84] T. Jackson, K. Mansfield, M. Saafi, T. Colman, and P. Romine, “Measuring soil temperature and moisture using wireless MEMS sensors,” *Measurement*, vol. 41, no. 4, pp. 381–390, 2008.
- [85] S. Baruah and J. Dutta, “Nanotechnology applications in pollution sensing and degradation in agriculture,” *Environ. Chem. Lett.*, vol. 7, no. 3, pp. 191–204, 2009.
- [86] P. D. Patel, “(Bio)sensors for measurement of analytes implicated in food safety: A review,” *TrAC - Trends Anal. Chem.*, vol. 21, no. 2, pp. 96–115, 2002.
- [87] D. R. Kipke, R. J. Vetter, J. C. Williams, and J. F. Hetke, “Silicon-substrate intracortical microelectrode arrays for long-term recording of neuronal spike activity in cerebral cortex,” *IEEE Trans. Neural Syst. Rehabil. Eng.*, vol. 11, no. 2, pp. 151–155, 2003.
- [88] E. M. Schmidt, M. J. Bak, F. T. Hambrecht, C. V Kufta, D. K. O’Rourke, and P. Vallabhanath, “Feasibility of a visual prosthesis for the blind based on intracortical microstimulation of the visual cortex,” *Brain*, vol. 119, no. 5, pp. 507–22, 1996.
- [89] C. J. Bettinger and Z. Bao, “Biomaterials-based organic electronic devices,” *Polym. Int.*, vol. 59, no. 5, pp. 563–567, 2010.
- [90] M. Luo, A. W. Martinez, C. Song, F. Herrault, and M. G. Allen, “A microfabricated wireless RF pressure sensor made completely of biodegradable materials,” *J. Microelectromechanical Syst.*, 2014.
- [91] D. She, M. Tsang, J. K. Kim, and M. G. Allen, “Immobilized electrolyte biodegradable batteries for implantable MEMS,” in *2015 Transducers - 2015 18th International Conference on Solid-State Sensors, Actuators and Microsystems, TRANSDUCERS 2015*, 2015.
- [92] H. Jimbo and N. Miki, “Gastric-fluid-utilizing micro battery for micro medical devices,” *Sensors Actuators, B Chem.*, vol. 134, no. 1, pp. 219–224, 2008.
- [93] Y. J. Kim, W. Wu, S.-E. Chun, J. F. Whitacre, and C. J. Bettinger, “Biologically derived melanin electrodes in aqueous sodium-ion energy storage devices,” *Proc. Natl. Acad. Sci. U. S. A.*, vol. 110, no. 52, pp. 20912–7, 2013.
- [94] Y. J. Kim, S.-E. Chun, J. Whitacre, and C. J. Bettinger, “Self-deployable current sources fabricated from edible materials,” *J. Mater. Chem. B*, vol. 1, no. 31, p. 3781, 2013.
- [95] F. Witte *et al.*, *Degradable biomaterials based on magnesium corrosion*, vol. 12, no. 5–6. 2008.
- [96] R. Langer, “Drug delivery and targeting,” *Nature*, vol. 392, no. 6679, pp. 5–10, 1998.
- [97] A. Södergård and M. Stolt, “Properties of lactic acid based polymers and their correlation with composition,” *Prog. Polym. Sci.*, vol. 27, no. 6, pp. 1123–1163, 2002.
- [98] D. Garlotta, “A Literature Review of Poly(Lactic Acid),” *J. Polym. Environ.*, vol. 9, no. 2, pp. 63–84, 2001.



- [99] S. Zhu *et al.*, “Biocompatibility of pure iron: In vitro assessment of degradation kinetics and cytotoxicity on endothelial cells,” *Mater. Sci. Eng. C*, vol. 29, no. 5, pp. 1589–1592, 2009.
- [100] H. Sun, L. Mei, C. Song, X. Cui, and P. Wang, “The in vivo degradation, absorption and excretion of PCL-based implant,” *Biomaterials*, vol. 27, no. 9, pp. 1735–1740, 2006.
- [101] D. Xue, Y. Yun, Z. Tan, Z. Dong, and M. J. Schulz, “In Vivo and In Vitro Degradation Behavior of Magnesium Alloys as Biomaterials,” *J. Mater. Sci. Technol.*, vol. 28, no. 3, pp. 261–267, 2012.
- [102] J. K. Nørskov *et al.*, “Trends in the exchange current for hydrogen evolution,” *J. Electrochem. Soc.*, 2005.
- [103] C. Song and J. Zhang, “Electrocatalytic oxygen reduction reaction,” in *PEM Fuel Cell Electrocatalysts and Catalyst Layers: Fundamentals and Applications*, 2008.
- [104] R. Udhayan and D. P. Bhatt, “On the corrosion behaviour of magnesium and its alloys using electrochemical techniques,” *J. Power Sources*, 1996.
- [105] N. Chang, W. H. Goodson, F. Gottrup, and T. K. Hunt, “Direct measurement of wound and tissue oxygen tension in postoperative patients,” *Ann. Surg.*, 1983.
- [106] M. B. Myers, G. Cherry, and S. Milton, “Tissue gas levels as an index of the adequacy of circulation: the relation between ischemia and the development of collateral circulation (delay phenomenon).,” *Surgery*, 1972.